TÉCNICO LISBOA

Development of a Flying Testbed for Airborne Wind Energy Harvesting

André Filipe da Cunha Pereira

Thesis to obtain the Master of Science Degree in

Aerospace Engineering

Supervisor: Prof. João Manuel Melo de Sousa

Examination Committee

Chairperson: Prof. Afzal Suleman
Supervisor: Prof. João Manuel Melo de Sousa
Member of the Committee: Prof. André Calado Marta

October 2022

Enjoy a victory,
Acknowledge a defeat,
You have delivered!
Trick or treat?

Declaração

Declaro que o presente documento é um trabalho original da minha autoria e que cumpre todos os requisitos do Código de Conduta e Boas Práticas da Universidade de Lisboa.

Declaration

I declare that this document is an original work of my own authorship and that it fulfills all the requirements of the Code of Conduct and Good Practices of the Universidade de Lisboa.

Acknowledgments

First of all, I would like to thank Instituto Superior Técnico as an institution which provided me the opportunity to become an Aerospace Engineer, as well as to all the professors who somehow contributed positively to my academical success.

Also, a sincerer thank you to Fundação para a Ciência e a Tecnologia who supported this work, through IDMEC, under LAETA, in the framework of project UIDB/50022/2020.

Then, a major thanks to my supervisor and professor João Melo de Sousa for all the support and effort put into along this last year. For all the patience in reading my long emails and in providing the answers to all my questions, for all the advice, directions and explanations, and basically for all the help reaching my goals with this thesis, thank you very much!

Finally, a big thanks to all the important people who surrounded me in this process. I thank my parents Sandra and Rui for always being present and for being the day-to-day support of my life. I thank my Avó Rita for all the possibilities offered me. I thank my Tia Paula for reading and correcting the stuff I sent to her. I thank my cousins for always putting a smile on my face. Lastly, I thank all the friends who helped me enjoy life during these months, clearing out my mind in the tough moments and making me understand priorities when I felt lost. From all of them, a very special thank you to Tomás, Mivas, Parlamento, Iara, Pixota, Rita M., Tiago M., Rita S., Henrique, Sofia, Diogo, CC, Carlota, Maria Sousa e Bella.

Resumo

Energia Eólica Aerogerada (AWE) abrange um novo e promissor modo de exploração de energia eólica, cuja tecnologia não se encontra ainda sedimentada. Dada a diversidade das soluções ao nível operacional e de arquitetura, selecionar um sistema AWE para uma possível implementação, num determinado local, constitui um cenário difícil e incerto.

Este trabalho incorpora uma extensa revisão sobre a tecnologia existente, a qual permitiu identificar treze fatores-chave para exploração de AWE. Categorizam-se em Fatores Técnicos de Projeto, Operacionais, de Manufatura, de Logística e de Aceitação Social. Utilizando-os numa análise multicritério, inferiu-se que um sistema de asa rígida com geração elétrica no solo e descolagem linear horizontal é o mais adequado tanto numa localização rural como marítima. O desempenho aerodinâmico foi identificado como o fator mais relevante para AWE.

Depois, considerando uma futura implementação, realizou-se um estudo sobre o potencial eólico de alta altitude em Portugal. Concluiu-se que uma exploração AWE é mais vantajosa em locais rurais, projetando-se uma velocidade de vento máxima de $18\,\mathrm{m/s}$ a $250\,\mathrm{m}$ de altitude.

Por fim, de forma a consolidar bases para futuros estudos em AWE, desenvolveu-se um protótipo experimental, recorrendo a testes em túnel de vento e em voo para o caracterizar aerodinamicamente e em termos de geração elétrica. O protótipo resultante consiste numa aeronave rádio-controlada (eficiência aerodinâmica máxima de 8.3) com dois geradores elétricos a bordo conectados em série. A uma velocidade de $18.6\,\mathrm{m/s}$, obtiveram-se $1.3\,\mathrm{W}$ de potência de saída. O protótipo evidencia algumas limitações, mas com potencial para otimização futura.

Palavras-chave: Energia Eólica Aerogerada, Fatores-chave de Projeto, Análise Multicritério via FANP, Recurso Eólico de Alta Altitude, Testagem em Túnel de Vento, Geração Elétrica a Bordo.

Abstract

Airborne Wind Energy (AWE) encompasses a new and promising way of exploring wind energy, which to date has not been fully established. Considering the diversity of technology at the operational and architectural level, selecting a particular system for a possible AWE implementation, targeting a certain location, is a difficult and uncertain scenario.

The present thesis embodies an extensive review on the existent technology, which allowed to identify thirteen key factors of AWE exploration, further categorized in Technical Design Factors, Operational Factors, Manufacturability, Logistics and Social Acceptability Factors. Applying them in a multi-criteria decision analysis, one inferred rigid wing pumping-cycle systems with horizontal take-off as the most suitable solutions for an AWE exploration in rural and off-shore sites. Also, aerodynamic performance resulted as the most relevant decision factor.

Then, relevant for a future AWE implementation, one studied the high-altitude wind resource potential in Portugal, concluding that an on-shore exploration of this resource would be more advantageous. A maximum sustained wind speed of $18\,\mathrm{m/s}$ at a height of $250\,\mathrm{m}$ was projected.

Finally, aiming to consolidate foundations for further studies on this subject, a flying experimental testbed was developed, resorting to wind tunnel and flight testing to characterize it aerodynamically and in terms of electricity generation. The resulting prototype consists of a radio-controlled aircraft (maximum aerodynamic efficiency of 8.3) and two on-board electric generators connected in series. At an airspeed of $18.6\,\mathrm{m/s}$, a $1.3\,\mathrm{W}$ output power was obtained. The prototype shows some limitations, however with clear potential for future optimization.

Keywords: Airborne Wind Energy, Key Design Factors, Fuzzy Analytic Network Process, High-altitude Wind Resource, Wind Tunnel Testing, Electric On-board Generation.

Contents

List of Tables

List of Figures

Abbreviations

ABL	Atmospheric Boundary Layer
ACU	Airborne Control Unit
AIS	Aeronautical Information Service
ANP	Analytic Network Process
ANAC	National Civil Aviation Authority
AP	Aerodynamic Performance
AWE	Airborne Wind Energy
BLS	Bridle Line System
CCI-LC	European Space Agency's Climate Change Initiative Land Cover
CG	Center of Gravity
CPP	Continuity of Power Production
CT	Conventional Tail
CTR	Controlability
DC	Direct Current
DU	Durability
DW	Downwind
EI	Ecological Impact
FANP	Fuzzy Analytic Network Process
FC	Flight Condition
ICAO	International Civil Aviation Organization
KCI	Knowledge-based Consistency Index
L	Logistics
LE	Leading Edge
LEI	Leading Edge Inflatable
LIDAR	Light Detection and Ranging

LHT	Linear Horizontal Take-off
LVT-HO	Linear Vertical Take-off with the aircraft in Horizontal Orientation
LVT-VO	Linear Vertical Take-off with the aircraft in Vertical Orientation
M	Manufacturability
MA	Mass-to-Area Ratio
MCDA	Multi-Criteria Decision Analysis
NI	Noise Impact
OB	On-board
OF	Operational Factors
OG	On-ground
QS	”Quasi-steady”
SAF	Social Acceptability Factors
SF	Safety
SL	Surface Layer
SLE	Supported Leading Edge
SQP	Sequential Quadratic Programming
SU	Survivability
TBT	Twin-boom Tail
TDF	Technical Design Factors
TLF	Take-off/Landing Feasibility
UW	Upwind
UTM	Universal Transverse Mercator
VI	Visual Impact
VLB	Variable Lower Boundary
VUB	Variable Upper Boundary
WT	Wind Turbines

Nomenclature

Greek symbols

α	Angle of attack, degrees.
α_0	Zero-lift angle of attack, degrees.
α_{c}	Corrected angle of attack, degrees.
α_{u}	Measured/Uncorrected angle of attack, degrees.
δ	Downwash effect correction factor.
η_θ	Cosine efficiency.
η_{aero}	Aerodynamic efficiency of the wind turbines.
η_{elec}	Motor/Generator electrical efficiency.
Γ	Environmental lapse rate, $\mathrm{K/km}$.
γ	Wing speed ratio.
γ^*	Optimal wing speed ratio.
Γ_{ad}	Adiabatic lapse rate, $\mathrm{K/km}$.
γ_{ri}	Reel-in speed factor.
γ_{ro}	Reel-out speed factor.
λ_{ts}	Ratio of tunnel section width to tunnel section height.
λ_{wg}	Wing taper ratio.
μ_M	Membership function.
μ_{air}	Air dynamic viscosity, $\mathrm{Pa.s}$.
Ψ	Stability correction function.
ρ_{air}	Air density.
Θ	Carrousel's kites angular position.
θ	Elevation angle.
v^*	Friction velocity, $\mathrm{m/s}$.

Roman symbols

$\mathcal{AR}$ Wing aspect ratio.

$\tilde{A}$ Fuzzy comparison matrix.

$\tilde{a}$ Triangular fuzzy set.

a Induction factor.

A_s Swept area, m^2.

a_{2D} Rate of variation of lift with the angle of attack for a two-dimensional profile.

A_{HT} Projected horizontal tail area, m^2.

A_{rot} Turbine rotor area, m^2.

A_{ts} Wind tunnel open section area, m^2.

A_{VT} Projected vertical tail area, m^2.

A_{wg} Wing area, m^2.

b Wing span, m.

$\overline{c}$ Wing mean chord, m.

C_L/C_D Aerodynamic efficiency or Glide ratio.

$C_\perp$ Tether cross section's perpendicular drag coefficient.

C_D Flying wing drag coefficient.

C_L Flying wing lift coefficient.

C_p Power coefficient.

C_R Total aerodynamic coefficient.

$C_{D,power}$ Extra drag coefficient for *Drag-mode* systems.

$C_{D,rot}$ Turbine drag coefficient.

$C_{D,t}$ Tether's drag coefficient.

$C_{D,u}$ Measured/Uncorrected drag coefficient.

C_{D0} Profile drag coefficient.

$C_{D_{FS}}$ Flying system drag coefficient.

C_{Di} Induced drag coefficient.

C_{F_y} Lateral force coefficient.

C_{Mx} Roll moment coefficient.

C_{My} Pitch moment coefficient.

C_{Mz} Yaw moment coefficient.

CI Consistency index.

D Flying drag force, N.

D_{rot} Turbine rotor diameter, m.

e Oswald efficiency.

e_{tip} Eccentricity of the wing tip.

F_a Total aerodynamic force, N.

$F_x^{\mathrm{no\_model}}$ Drag force measured at the scale with no model mounted, N.

f_{max} Maximum profile camber, m.

F_{trac} Tether traction force, N.

F_x Drag force measured at the scale, N.

F_y Lateral force measured at the scale, N.

F_z Lift force measured at the scale, N.

g Gravitational acceleration, $\mathrm{m/s^2}$.

h Altitude, m.

h_{ref} Reference height, m.

h_{SL} Surface layer thickness, m.

h_{ts} Wind tunnel open section height, m.

I_{in} Input current, A.

I_{out} Output current, A.

k Von-Kárman constant.

K_n Static margin.

L Flying wing lift force, N.

l^z Lower bound of fuzzy judgment.

L^{Ob} Obukhov Length, m.

l_t Straight tether length.

$l_{CA_{wg}-CA_tl}$ Distance between the wing's and tail's aerodynamic centers, m.

l_{ts} Wind tunel open section width, m.

m Flying system mass, kg.

m^z Fuzzy judgment's most probable value.

M_x Roll moment, $\mathrm{N.m}$.

M_y Pitch moment, $\mathrm{N.m}$.

M_z Yaw moment, $\mathrm{N.m}$.

m_{mod} Modified aircraft mass, kg.

m_{orig} Original aircraft mass, kg.

n Number of rows/columns of a square matrix.

$n_{clusters}$ Number of clusters.

n_M Motor rotational speed, RPM.

N_{rot} Number of on-board turbines.

n_{rot} Turbine rotational speed, RPM.

$\Delta P_{w,\Delta h}|^{\mathrm{altitude}}$ Gain in $P_{w,\Delta h}|_{h_0}^{h_1}$, by increasing altitude, $\%$.

$\Delta P_{w,\Delta h}|^{\mathrm{stability}}$ Gain in $P_{w,\Delta h}|_{h_0}^{h_1}$, by going from unstable to stable atmospheric conditions, $\%$

p_0 Static pressure at the surface in standard atmosphere, Pa.

P_W Wind power, W.

P_{cycle} Cycle's overall mechanical power, W.

p_{din} Dynamic pressure, Pa.

P_{elec}^{in} Electrical input power, W.

P_{elec}^{out} Electrical output power, W.

P_{loss} Lost power, W.

P_{max} Maximum power any given wing can extract from the wind, W.

P_{mech} Mechanical power, W.

P_{ref} Preference percentage.

p_{stat} Static pressure, Pa.

$P_{w,\Delta h}|_{h_0}^{h_1}$ Wind power passing through a vertical strip of unit width, $\mathrm{W/m}$.

Q_M Motor torque, $\mathrm{N.m}$.

R Electrical circuit resistance, Ω.

R_{air} Individual gas constant of air, $\mathrm{J/kg.K}$.

Re Reynolds number.

s_X Sample standard deviation.

T Temperature, K.

T_0 Temperature at the surface in standard atmosphere, K.

t_{max} Maximum profile thickness, m.

u^z Upper bound of fuzzy judgment.

U_{in} Input voltage, V.

U_{out} Output voltage, V.

V_a Apparent wind speed, $\mathrm{m/s}$.

V_C Crosswind speed $\mathrm{m/s}$.

V_H Horizontal tail volume ratio.

V_H Vertical tail volume ratio.

V_w Wind speed, $\mathrm{m/s}$.

V_{ri} Reel-in speed, $\mathrm{m/s}$.

V_{ro} Reel-out speed, $\mathrm{m/s}$.

V_{stall} Stall speed, $\mathrm{m/s}$.

$V_{t\infty}$ Wind tunnel airflow speed at the test section, $\mathrm{m/s}$.

w Comparison matrices resulting weightings.

w_{ts} Tether cross section width.

$\overline{X}$ Mean value of a X set of measurements

z_0 Surface roughness length, m

Subscripts and Superscripts

$_{aero}$ ^{aero} Aerodynamic.

^{G} Generator.

$_{max}$ ^{max} Maximum.

$_{mod}$ ^{mod} Modified aircraft.

$_{in}{}^{in}$ Input.

$_{orig}{}^{orig}$ Original aircraft.

$_{out}{}^{out}$ Output.

Operators

$\otimes$ Fuzzy multiplication.

$min\{\}$ Minimum value.

$\cap$ Set intersection.

$sup\{\}$ Supremum.

$\vec{}$ Vector.

Chapter 1: Introduction

1.1 Energy Consumption and Climate Crisis

In the contemporary times, it is hard to name a day-to-day activity or equipment which does not require electricity consumption at some point. It is even harder when we think at a larger scale, namely in the various business/industrial sectors. In fact, since the beginning of the century, electricity consumption grew 80% [1]. To produce electricity, other types of energy have to be consumed. This global energy consumption has been increasing mainly driven by the expansion of the industry and residential areas in several countries in Middle East, Asia and Africa [2] and it is expected to keep increasing up to 22% by the end of 2050 [3].

Although this increase embodies a worldwide technological development, it also represents one of the most urgent challenges faced nowadays by humankind. This is mainly due to the fact that, with the current distribution of energy production among the different sources, costs to human health and the environment are becoming unbearable. To the date, fossil fuels (coal, natural gas and oil) account for more than 80% of the global primary energy demand - see figure 1.1 [4]. The combustion of these fuels releases chemical compounds as sulfur (SO_x) and nitrogen (NO_x) oxides as well as carbon dioxide (CO_2). On one hand, the first two are major air pollutants, which cause adverse human health effects, reduction of agricultural yields, damage to forests and fisheries (acid rain), and damage to buildings and infrastructure. On the other hand, the increase of the CO_2 concentration in the atmosphere, as being a greenhouse gas, is the main reason of the global warming and its ensuing detrimental effects - climate changes, biodiversity reduction, increase of mean sea level, to name a few [5].

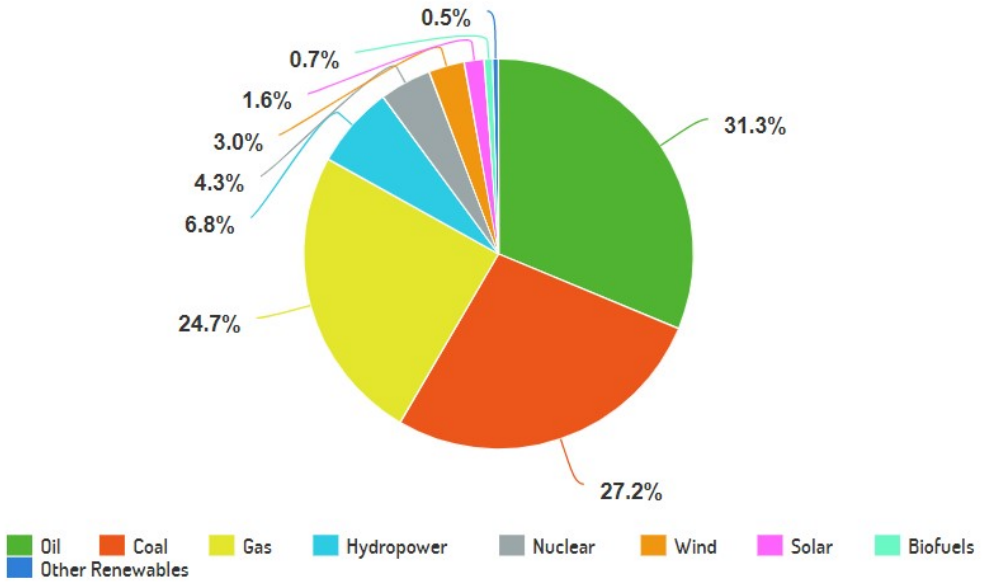

Figure 1.1: Global primary energy demand.

The awareness for these problems is not recent. The Kyoto protocol was adopted by many nations around the world in 1997 with the purpose of committing industrialized countries and economies in

transition to limit and reduce greenhouse gases. In 2016, this protocol was replaced and updated by a legally binding international treaty called the Paris Agreement. It was signed by 196 parties and its ultimate goal is to limit the global warming up to $2^\circ\,\mathrm{C}$ compared to pre-industrial levels [6].

Therefore, in order to reach carbon neutrality, it is imperative to pursue the usage of a suitable combination of alternative and sustainable energy sources. Moreover, studies show that, besides its benefits for the environment, promoting renewable energies influences positively the economic [7] and social [8] conditions of a country.

1.2 Wind Resource Potential and Conventional Technology

The renewable energy technology with the lowest carbon footprint is the wind energy technology [9], and it only accounts for 3% of the global primary energy demand, as depicted in figure 1.1. Nowadays, this resource is mostly explored by using wind turbines (WT) both on- and off-shore. Their main components are the tower (for elevation), the blades (typically three) and the nacelle which contains the electric generator, the gearbox and the control systems. They capture energy as the wind spins the blades of the turbine, transforming wind energy into mechanical energy and then into electrical energy through the generator.

The land occupation of the present wind farms is about $7-8$ and $2-3$ turbines per km^2, respectively for on-shore and off-shore, considering $2-4\,\mathrm{MW}$, $90-120\,\mathrm{m}$ diameter turbines. The corresponding power output density is about $7\,\mathrm{W/m^2}$ on-shore and $3\,\mathrm{W/m^2}$ off-shore, which is $100-300$ times lower than that of large thermal plants [10]. Moreover, due to wind intermittency, a wind farm is able to produce an average power which is only a fraction of its rated power (i.e. the power output for which the electric system was designed), named as "Capacity Factor". Its values are around $0.3-0.45$ on-shore and $0.4-0.6$ off-shore for "good" sites. All these issues make current wind energy production not competitive with respect to fossil energies.

Globally and in general, the wind speed tends to increase with altitude. According to an assessment carried out by Archer and Caldeira [11], the winds are not only stronger but also more consistent with increasing height, both on- and off-shore. Thus, when extracting energy, this allows larger rated powers as well as achieving higher capacity factors. For example, in the land mass and coastal areas of Europe at a variable-height up to $500\,\mathrm{m}$, the wind power density which is available 95% of the time doubles when comparing to the one at a fixed height of a conventional WT [12]. What is more, Marvel et al. [13] show that the extraction of 'only' $18\,\mathrm{TW}$ (i.e. a quantity comparable with the world power demand at the date) of $1800\,\mathrm{TW}$ available in the whole atmospheric layer would not produce significant damaging effects at a global scale. Hence, the geophysical potential is huge.

However, taking advantage of high altitude wind with the conventional technology would be financially very costly, since higher and structurally more resistant towers would be needed as well as more reliable foundations (the tallest wind turbine is Haliade-X with 260 m [14]). Additionally, only part of the blades contributes efficiently to power production: the outer 30% of the blades account for more than half of the production [15].

1.3 Airborne Wind Energy: a solution to develop

Aiming to circumvent the aforementioned difficulties, the concept of Airborne Wind Energy (AWE) arose, being first introduced by Loyd [16] in the eighties. Roughly speaking, AWE systems aim to harvest power from winds at altitudes higher than conventional wind turbines, while replacing their tower and inner part of the blades (which have a relatively low contribution to power generation) by a tether. This connects a flying energy harvesting system, which is replacing the aforementioned 30% outer part of the blades, to a ground station. This idea represents a substantial smaller material investment per unit of usable power than most other renewable energy sources (90% saving as compared to conventional WT [17]). However, that comes at a cost: while a conventional wind turbine is a stationary construction on the ground, an AWE system operates while flying and, whenever a malfunction occurs, the prospect of a total system destruction comes to light. As a consequence, there are several aspects that must be taken into account in the choice and design of these systems.

There are two major groups of AWE systems based on their flight principles / operation: the crosswind and the non-crosswind systems. The first basically consists in flying in a transverse direction (or close to it) with respect to the wind flow, which can be implemented through reciprocating patterns, such as figure eights, or returning patterns, such as circles. Usually, the former pattern is preferred since it avoids the twisting of the tether [18]. This kind of motion allows an increase of the relative velocity of the flying wing, which is very beneficial. The second case, in general, includes the systems that operate using only aerostatic lift, by employing a lighter-than-air gas, as well as the systems which are rotary.

Despite the high power-to-mass ratio promised by AWE, there is still no mature technology available in the market to enable the large-scale deployment of this technology at comparably low costs. Only in most recent years, companies such as Kitepower and SkySails commercially deployed systems in the Caribbean [19] and Mauritius Islands [20], respectively. These are locations with low energy necessities and, being off-grid, they have to resort to Diesel generators, which are very costly. It is the same case for several off-grid activities, such as mining or agriculture. Hence, AWE constitutes a promising alternative that assures local power supply.

1.4 Objectives and Deliverables

The ultimate goal in this industry is to reach a technically reliable and economically viable technology [21] that can be produced in scale in order to further reduce costs and help in the present energetic crisis. Accordingly, the most adequate and propitious system for a given site must be identified. Hence, this work aims to review the scientific advances accomplished all around the world [22] on the most promising AWE systems: the crosswind systems, which Loyd [16] showed to have the largest electric power output. Then, based on the information gathered, one will try to answer the following questions:

1. ”What are the key factors determining the choice and design of a particular AWE system?”;
2. ”From the existing alternatives in the literature, which is the most promising for a certain exploration site?”.

Furthermore, since Portugal currently relies on wind energy to produce around 31% of its electricity [23] and, at the average hub height of a WT, it is, in general, a country with a moderate wind resource both on- and off-shore (extensive coastline) [24, 25], then the necessity and the opportunity to go higher and invest in AWE systems presents itself and has great potential.

That being the case, with this work, one hopes to deliver an initial framework on the subject and contribute to enhance the deployment of this technology in Portugal, by developing and testing a small-scale prototype.

1.5 Thesis Outline

This thesis is organized in seven chapters from which the present is the Introduction.

In chapter 2, an extensive review on the characteristics of currently existing AWE technological solutions, namely crosswind systems, is done. It is focused on their physical (section 2.2) and operative foundations (sections 2.3 and 2.4), as well as on the hardware architecture (sections 2.5 to 2.7). It has the purpose of providing the information required to identify and assess key factors determining the choice and design of a particular AWE system.

In chapter 3, one categorizes and describes the aforementioned key factors. An introductory comparison of the different possibilities, regarding the identified factors, is also the focus of the chapter.

In chapter 4, one makes use of the information presented in the previous two chapters to perform a Multi-Criteria Decision Analysis, from which a site-dependent selection of the most suitable Airborne Wind Energy system is done: in section 4.1, the methodology is described, whereas in section 4.2 it is applied to the AWE system decision scenario.

In chapter 5, an assessment of the high-altitude wind resource for a region of Portugal is performed: in sections 5.1 to 5.3, the fundamentals and methods are described, and in section 5.4 conclusions about the potential for AWE harvesting in the region are taken.

In chapter 6, the development of an experimental testbed for AWE harvesting is carried out. The testbed is described geometrically (6.1) and their aerodynamic and power generation characteristics are obtained, resorting to wind tunnel testing (sections 6.2 to 6.3). Finally, in section 6.4, one describes the procedures for flight testing the testbed, as well as presents the respective results.

At last, in section 7, the conclusions remarks and future development recommendations are given.

Chapter 2: Background

In this chapter, one presents the types of AWE crosswind systems, their physical and operational fundamentals, as well as the characteristics of their components and subsystems.

2.1 Types of Crosswind Airborne Wind Energy Systems

As previously introduced, crosswind systems are the most promising systems in AWE - more detail in section 2.2. In figure 2.1, one showcases a categorization of these systems, as well as, a list of companies / research institutions with accomplished work in prototypes of each category.

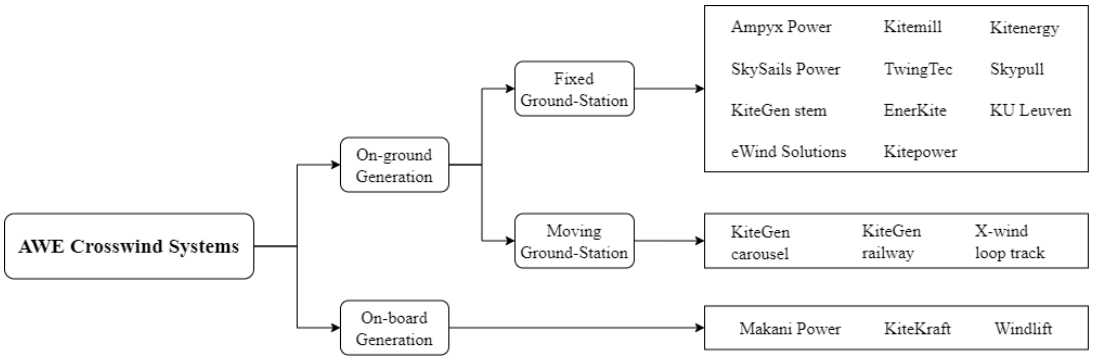

Figure 2.1: Classification of AWE crosswind systems, with list of institutions with developed prototypes.

Crosswind systems are divided into two groups in line with the location of their electricity generators, which also coincides with the distinction between *Lift-* and *Drag-mode* done by Loyd [16]. Power production can be done either in the ground station or on-board of the flying wing. The first of these cases is referred as *Lift-mode* and will be analyzed in detail in section 2.3. One can further split these systems in consonance with the ground station in-operation mobility, i.e. if the station is fixed in one position or moving along a given path while producing power. The second case is designated as *Drag-mode* and will be explored in section 2.4. Here, the flying wing carries on-board generators and sends down the electric current through the tether. For illustration purposes, in figures 2.3 and 2.2, prototypes by the mentioned institutions are presented. Despite belonging to the same categories, all the systems show certain singularities distinguishing them such as wing rigidity, flight control, take-off and landing operations, and more. Recent studies show that both on-board and on-ground generation systems still have a similar chance of achieving design dominance, with a slight advantage to the latter [26].

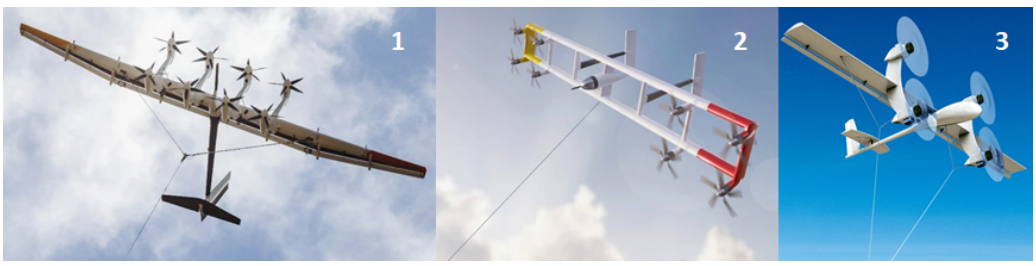

Figure 2.2: Prototypes of on-board generation systems. 1 - Makani Power [27]; 2 - KiteKraft [28]; 3 - Windlift [29].

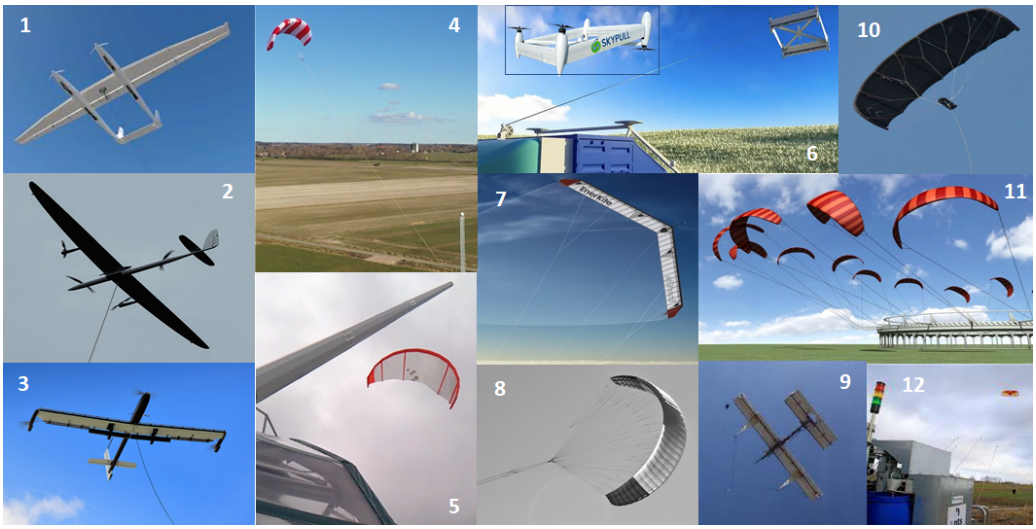

Figure 2.3: Prototypes of on-ground generation systems. Fixed Ground Station: 1 - Ampyx Power [30]; 2 - Kitemill [31]; 3 - Twingtec [32]; 4 - SkySails Power [33]; 5 - KiteGen Stem [34]; 6 - Skypull [35]; 7 - Enerkite [36]; 8 - Kitenergy [37]; 9 - eWind Solutions [38]; 10 - Kitepower [39]; Moving Ground Station: 11 - KiteGen railway [40]; 12 - X-wind loop track [41].

2.2 Physical Foundations of Crosswind Motion

In this section, the fundamentals of AWE exploitation using crosswind motion are presented. The potential power any given wing can extract from a wind field is also established. The following concepts and deductions can be looked up in more detail in [42, 43].

2.2.1 Relevant Forces and Velocities in Crosswind Motion

As mentioned earlier, it is well known that flying in crosswind with a velocity $-\overrightarrow{V_c}$, in the sense indicated in figure 2.4, larger than the true wind speed, $\overrightarrow{V_w}$ (assumed to be uniform and constant, parallel to the ground plane), maximizes performance. The wing, as well as the tether, "sees" an airflow with an apparent airspeed, $\overrightarrow{V_a} = \overrightarrow{V_w} + \overrightarrow{V_c}$, whose intensity may be substantially larger than V_w. In this way, in comparison with non-crosswind generation, the aerodynamic forces Lift (L) and Drag (D) are stronger, providing one or two orders of magnitude higher power [16]. These quantities are represented in figure 2.4 as resultant forces applied at a single point (center of pressure), and are given by equations (2.1) and (2.2), where ρ_{air} is the local air density, A_{wg} denotes the wing area, and C_L and C_D stand for the lift and drag coefficients, respectively.

$$L = \frac{1}{2}\,\rho_{air}\,A_{wg}\,C_L\,V_a^2 \qquad (2.1) \qquad\qquad D = \frac{1}{2}\,\rho_{air}\,A_{wg}\,C_D\,V_a^2 \qquad (2.2)$$

According to Prandtl lifting-line theory [44], the lift coefficient of a finite wing can be obtained from equation (2.3), where α is the angle of attack, measured between the mean chord of the wing, $\bar{c}$, and the velocity vector $\overrightarrow{V_a}$; α_0 is the zero-lift angle of attack; $a_{2\mathrm{D}} = \frac{dC_{L,2\mathrm{D}}}{d\alpha}$ represents the rate of variation of lift with the angle of attack, in the linear region, of a two-dimensional airfoil [44]; and $\mathcal{AR} = \frac{b^2}{A_{wg}}$ is the aspect ratio of the wing, where b denotes the wing span.

$$C_L = \frac{a_{2D}}{1 + \frac{a_{2D}}{\pi\,\mathcal{AR}}}\,(\alpha + \alpha_0) \qquad (2.3)$$

Regarding the drag coefficient, it is calculated as the sum of both wing and tether drag coefficients. On one hand, the wing drag coefficient (C_D) is given as the sum of the *profile drag* C_{D0} and the *induced drag* C_{Di}. The former is due to viscous effects and it can be considered constant in the linear region of $C_L(\alpha)$ (before stall occurs); the latter, again in accordance to the lifting-line theory, is obtained from equation (2.4), where e stand for the *Oswald efficiency*.

$$C_{Di} = \frac{C_L^2}{\pi\,\mathcal{AR}\,e} \tag{2.4}$$

On the other hand, the tether's drag coefficient ($C_{D,t}$) can be easily computed if assumed a straight tether of length l_t with a cross section of width w_t and of drag coefficient $C_\perp$ [43]:

$$C_{D,t} = \frac{C_\perp\, l_t\, w_t}{4\, A_{wg}} \tag{2.5}$$

Hence, the total drag coefficient of a typical AWE crosswind flying system is the result of the following summation:

$$C_{D_{FS}} = C_D + C_{D,t} = C_{D0} + \frac{C_L^2}{\pi\,\mathcal{AR}\,e} + \frac{C_\perp\, l_t\, w_t}{4\, A_{wg}} \tag{2.6}$$

Finally, the total aerodynamic force is given by equation (2.7), where $C_{D,power}$ denotes an extra drag force coefficient applied by an on-board power generation device (e.g., on-board turbine), if it is the case, and C_R is the total aerodynamic coefficient:

$$F_a = \frac{1}{2}\,\rho_{air}\,A_{wg}\,V_a^2\,\sqrt{C_L^2 + (C_{D_{FS}} + C_{D,power})^2} = \frac{1}{2}\,\rho_{air}\,A_{wg}\,V_a^2\,C_R \tag{2.7}$$

The key point is that the high speed of the wing can be maintained by the wind flow. On one hand, in *Drag-mode*, the on-board turbines are facing the airflow, as if they were thrust generators, but rotating by action of a drag force, thus producing electrical power. On the other hand, in *Lift-mode*, the high speed leads to the generation of the aerodynamic force F_a (in great part the lift force) that will traction the tether. The consequent movement can be made useful for harvesting part of the power that the moving wing can potentially extract from the wind field. Furthermore, using crosswind motion also brings an advantage when considering variable wind speed: when the wind speed is too high, the intensity of the local (and useful) wind speed V_a can be kept constant by reducing the crosswind speed.

Figure 2.4 illustrates a simple scheme of the relevant forces and velocities involved in crosswind motion with the wing in a downwind position. Due to the connection to the ground station and the need to reach a certain altitude, there is an elevation angle θ that reduces the extractable power. Considering a completely straight tether, so that F_a is in balance with the tether tensile force (as Loyd did [16]), then the real total power P_w that a flying wing can extract from the wind field is given by:

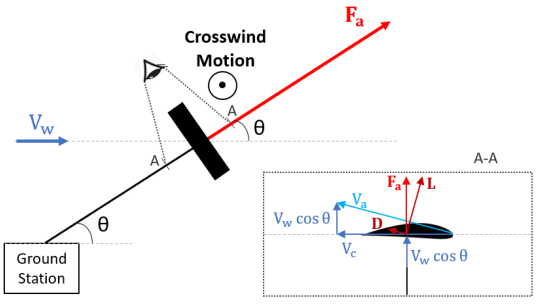

Figure 2.4: Two-dimensional sketch of the relevant speeds and aerodynamic forces around a wing for wind power generation.

$$P_w = V_w\,F_a\,\cos\theta \tag{2.8}$$

This is called the *cosine loss* and gives an upper bound on the usable wind power. Another source of

cosine losses is the weight of the airborne system, which leads to the need of imposing a larger θ in order to the vertical component of F_a compensate the weight. Loyd [16] assumed this force as well as inertia forces were relatively small compared to aerodynamic forces. In fact, for most of the systems flying at strong enough wind speeds, the *cosine losses* due to gravity can be neglected in power estimations. What is more, numerical simulations presented in [45] showed an increase in power of only 0.5% when neglecting those forces. Even so, in accurate system modeling studies, these forces must be considered.

2.2.2 Power Limit of AWE by Loyd and Diehl

In order to derive a physical upper limit on usable power that any given wing can extract from a wind field, one considers the situation sketched in figure 2.4. Hence, the usable power P is defined as $P = P_w - P_{loss}$, where P_w comes from equation (2.8) and P_{loss} are the power losses, which means that at least: $P_{loss} \geq V_a\, D_{FS}$. By combining these considerations, by taking into account equation (2.7), by defining a *wing speed ratio* ($\gamma = {}^{V_a}/_{V_w}$), and by maximizing the resultant expression of P, one gets:

$$P_{max} \;=\; \frac{2}{27}\,\rho_{air}\,A_{wg}\,(V_w\,\cos\theta)^3\,C_R\left(\frac{C_R}{C_{D_{FS}}}\right)^2 \tag{2.9}$$

corresponding to an optimal operational *wing speed ratio*, as:

$$\gamma^* \;=\; \frac{2\,C_R\,\cos\theta}{3\,C_{D_{FS}}} \tag{2.10}$$

This limit is both valid for *Lift-mode* and *Drag-mode*, as no such distinction was made in its derivation. One can also determine the tether traction force that maximizes power extraction by substituting V_a in equation (2.7) by the optimal operation airspeed, as:

$$F_{trac}|_{P_{max}} \;=\; F_a|_{P_{max}} \;=\; \frac{2}{9}\,\rho_{air}\,A_{wg}\,V_w^2\,(\cos\theta)^2\,C_R\left(\frac{C_R}{C_{D_{FS}}}\right)^2 \tag{2.11}$$

Furthermore, the following conclusions can be deduced:

- At optimal operational wing airspeed:

$$P_{max} \;=\; V_w\,F_a\,\cos\theta - \frac{2\,C_R\,\cos\theta}{3\,C_{D_{FS}}}\,V_w\,D_{FS} \;\;\Longrightarrow\;\; P_{max} \;=\; \frac{1}{3}P_w \tag{2.12}$$

  meaning that an optimal operated AWE can only harvest one third of the available power. This is due to the fact that the optimization was done to get the maximum usable power, which is the ultimate goal, rather than achieving maximum aerodynamic efficiency. Hence, two thirds of the power are dissipated as drag losses.

- The impact of the elevation angle on the maximum usable power arises in the form of $\eta_\theta = (\cos\theta)^3$, which can be seen as the *cosine efficiency*. Thus, flying with a mean elevation of 30^o, for example, means the available power is only 60% of the maximum possible.

- If the aerodynamic efficiency ${}^{C_L}/_{C_{D_{FS}}}$ (also referred as *glide ratio*) is high and $C_{D,power}$ is comparatively small (for *Drag-mode* systems), then one can assume $C_R \approx C_L$, which is the same as saying that $V_a \approx V_c$. This is usually a good assumption for AWE systems. In this way, the *glide ratio*

enters the power limit quadratically, which means it is is beneficial to have low drag coefficients. For efficient airfoils, the wing drag is low, so typically the most significant term is the tether drag.

It is important to reinforce that this limit is really idealized and it carries some limitations due to the assumptions made. Firstly, the presumption of a straight cable with a known tension is not valid for very long tethers; by removing it, a fourth-order polynomial shape function arises [46], which is more accurate. Secondly, the hypothesis of steady flight should also be removed when considering very long tethers, since that, in unsteady conditions, the lower part of the cable could reasonably move less, thus dissipating a smaller amount of energy [43].

Furthermore, when considering very high efficient airfoils, more specifically when one takes the drag coefficient $C_{D_{FS}}$ to zero, the maximum power P_{max} (Cf. eq. (2.9)) goes to infinity, as so does the airspeed (eq. (2.10)), which clearly departs from reality. One way to cope with this situation is to consider that the wing, as it flies, slows down the wind going through its path, such that the wind speed reaching the wing should only be a fraction of the undisturbed wind speed. In this way, the conservation of energy in the interaction wind/wing is properly taken into account [47].

This is consistent with the application of the actuator disk theory, which is typically done for conventional wind turbines. A power coefficient is computed, which is a measure of the performance of the energy extracting device [48]. It is defined as the ratio of the extracted power by the turbine rotor and the available power in the wind (first equality in eq. (2.13)), where A_s is the swept area (e.g., by the blades). It is computed, as follows:

$$C_p = \frac{P_{elec}^{out}}{\frac{1}{2}\,\rho_{air}\,A_s\,V_w^3} = 4\,a\,(1-a)^2 \tag{2.13}$$

where a is the *induction factor* - it measures the interference of the disk on the air flow. When the induction factor takes the value of $1/3$, the *Betz limit* is achieved ($C_p = 0.59$) [49]. It is the maximum possible value for this power coefficient.

In [50], Archer states that the C_p of AWE systems is, at the date, unknown. In addition, the relevance of the *Betz limit* for this kind of systems is questionable due to the fact that the concept of a disk-like swept area is not applicable. Loyd's point of view is that the criteria for the efficiency in flying wings and its turbines is different from the one used by Betz and that the maximum power is achieved when the induction factor is minimized [16], so he neglects its effects, as previously seen. Moreover, in [51], the researchers argue that the area swept by the flying wing is generally very large, thus the *Betz limit* "cannot meaningfully be applied".

2.3 On-Ground Generation Systems

In On-Ground Generation Systems, electrical energy is produced on the ground station by means of converting mechanical work. This is done by a traction force of intensity F_a, on which the $C_{D,power}$ term is zero (eq. (cf. 2.7)). That force is transmitted by one or more tethers connected to the flying wing and the way it produces motion on the ground generator is the differentiating aspect of the existing configurations. As introduced in section 2.1, there are two major classes. Most of the research and implemented prototypes encompass a fixed ground-station, namely the Pumping-Cycle AWE system. With respect

to moving ground-station systems, the relevant configurations are the Vertical Axis Generator and the Railway Generator. These three concepts will be analyzed next.

2.3.1 Pumping-Cycle System

A typical Pumping-Cycle system has the following main components [53]:

1. **Flying wing**: it can be a rigid ([30–32, 35, 38]), soft ([33, 34, 36, 37, 39]) or hybrid wing;
2. **Tether** for mechanical work and additional cables for control actuation (e.g., bridle line system in case of soft or hybrid wings);
3. **Control Unit**: it can be placed on the ground station or in-between the tether and control cables (e.g., control-pod in [39] or [33]) or even on-board the rigid wing (autopilot system);
4. **Mechanical Power Converter**: drum winch, gearbox to increase rotation speed and motor/generator, placed on the ground-station;
5. **Electrical Converter**: battery, inverter, transformer and other electronic components, placed on the ground-station;
6. **Launching and Landing systems/platforms**: major part of the ground-station.

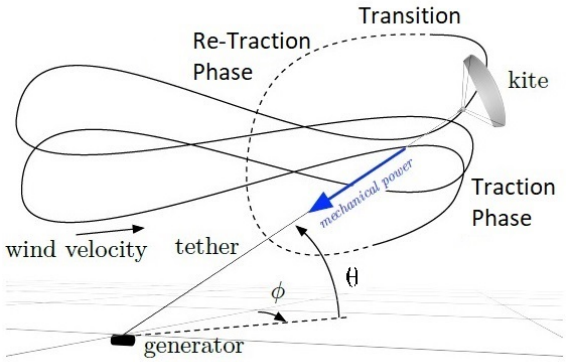

Figure 2.5: Three phases of a pumping-cycle configuration. ϕ is the azimuth angle, which should be zero for optimal operation (downwind) [52].

As its designation points out, this kind of system operates in cycles. Each cycle has three consecutive phases: Traction, Transition, and Re-Traction [54], as sketched in figure 2.5.

In the first phase, electrical energy is produced. The wing operates at a high angle of attack in order to generate high lift force and thus high traction force in the tether. The tether is continuously reeled-out with a constant velocity of $V_{ro} = \gamma_{out} V_w$, where γ_{out} is a constant factor. The reeling-out makes a drum to rotate. This mechanical energy is then converted to electrical energy, for which, to be maximized, the wing must fly in fast crosswind maneuvers. Typically, it flies in figures of eight (instead of circles) only in order to avoid twisting of the tether, since it has been shown the power produced by loop is independent from the chosen trajectory topology [55]. The Traction phase lasts until the maximum variation of tether length is reached. In practice, this reel-out phase can be further subdivided by implementing a *three-stage strategy*, according to the wind speed variation while climbing [56]. This strategy aims to limit the tether force to an upper bound (to preserve the longevity of the tether and for safety reasons) as well as to curb the amount of power produced, so that overloading of the generator may be avoided.

At the end of the reel-out, the transition phase begins. This stage has approximately no power production nor consumption as showcased in figure 2.6 and should be as short as possible. During it, arrangements are done in order to reduce the traction force to a minimum value so that the power consumed in the third phase is also minimal (*wing depower*). There are two main possibilities [57]. The first consists in increasing the elevation angle up to 90^o, which leads to a cease of the crosswind

motion, and thus the apparent wind speed would be equal to the wind speed. However, this approach is relatively slow, so what is usually done is to keep the current elevation angle and decrease the angle of attack by pitching the wing in a nose down direction, which decreases lift, and consequently the traction force as well. Although this approach leads to a larger power consumption in the third phase, it allows high reel-in speeds, therefore compensating in the overall cycle power.

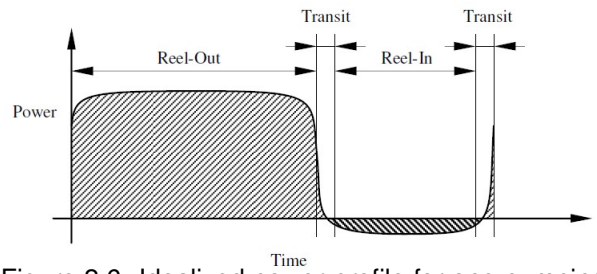

Figure 2.6: Idealized power-profile for one pumping mode cycle [58].

Finally, in the re-traction phase, the generator is switched to a motor configuration and reels-in the tether with a velocity of $V_{ri} = \gamma_{ri} V_w$. Since there is power consumption, this stage should be kept, once again, as short as possible. Ideally, the traction force in this phase only has to compensate the wing profile drag (i.e. $L \approx 0 \Longrightarrow C_{D_{FS}} \approx C_{D0}$). In practice, the zero lift condition is not doable and the minimal tether force needed to reel-in the wing in a controlled way may be considerably more than only its drag [56].

After completely reeling-in, there is a short transition to the initial position and the production phase restarts. However, figure 2.6 highlights one of the main disadvantages of this kind of system: pumping-cycle generators present a highly discontinuous power output, with long alternating time-periods of energy generation and consumption, which brings the need to integrate electrical rectification components, such as large capacitors or extra batteries [43].

The overall mechanical power cycle of these systems may be given by the following equation [56, 59]:

$$P_{cycle} = \frac{1}{2} \rho A_{wg} V_w^2 \left(C_L \left(\frac{C_L}{C_{D_{FS}}}\right)^2 (\cos\theta - \gamma_{out})^2 - C_{D0} (\cos\theta + \gamma_{ri})^2\right) \frac{\gamma_{out}\,\gamma_{ri}}{\gamma_{out} + \gamma_{ri}} \tag{2.14}$$

It is noteworthy that if the re-traction phase was carried out at infinite speed ($\gamma_{ri} = \infty$) without resistance ($C_{D0} = 0$), then the maximum power would be achieved for $\gamma_{out} = \frac{1}{3}\cos\theta$. This result can also be obtained by making P_{max} of equation (2.9) equal to $F_a V_{ro}$, which shows accordance with the upper limit of power derived by Diehl. Therefore, in reality, the reel-out speed should be smaller than one third of the wind speed (optimal case when $\theta = 0$) in order to maximize the net power of the cycle [60]. Moreover, numerical results illustrate that optimal power generation is most sensitive to the cycle time, tether length, and wind speed [61].

The power deduced in equation (2.14) concerns only the resultant mechanical power. On top of that, in order to get the total power output, one should consider the mechanical and electrical efficiencies, and subsequent optimizations [62]. The first has to do with, for example, the efficiency of the motor brakes, of the spindle motor that moves the drum and/or of the gearbox that transmits the mechanical torque from the drum to the electrical generator [63]. The second covers the efficiencies of batteries and mainly of the electric generator/motor, which mainly depends on its type and size (larger generators have better efficiencies [64]). Typically, using synchronous generators (with direct drive, i.e. no gearbox included) provides good efficiencies [65].

At last, one must describe three adaptations of the usual pumping-cycle system. The first two configurations differ in the way mechanical power transfer is performed, whereas the third presents a modification in the tether that increases the cycle efficiency. It is relevant to note that only the first concept was experimentally tested.

2.3.1.1 KG-yoyo from KiteGen

This system consists of a soft wing connected to the ground station by two tethers [66], as shown in the schematic in figure 2.7. The wing is controlled by differential pulling of these two tethers. Each one unreels from a different generator/motor. The resultant aerodynamic force is distributed by the two cables, which implies that the traction force in each one is smaller. This allows having tethers with smaller widths and therefore smaller drag. The reeling-out speeds of each tether may be different and depend on the flight path. In addition, special care must be taken in order to prevent the entanglement of the tethers.

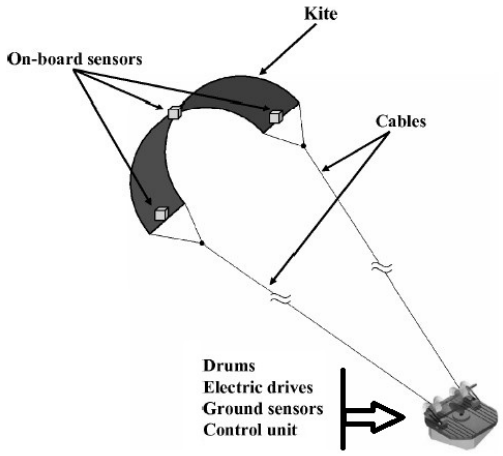

Figure 2.7: Schematic of KG-yoyo pumping-cycle system (at left) [66].

2.3.1.2 High Speed Mechanical Power Conversion System

A first approach is described in [67] and is sketched in figure 2.8. Two wings are connected to a fixed point on a rotating platform, which guarantees omnidirectionality, through tethers of constant length. The mechanical power is transferred to the generator by a belt that only moves in the reel-out direction, thus not producing any drag. The top end of the belt is attached to a motion transfer cable. In the traction phase, which lasts about 50% to 75% of the entire cycle, the wings move from positions $A_{1,2}$ to $B_{1,2}$ pulling the belt at a very high speed and making a sprocket to rotate. Electricity is then produced by the generator. In the re-traction phase, the wings return to the initial position with minimum power consumption. This extremely high speed is found to be problematic, and must be controlled.

The second variant of this concept is described in [68] and it is illustrated in figure 2.9. The working principle is the same as the previous, differing in the mechanism of motion transfer only. The two wings move in counter phase, which allows continuous operation and thus increases the cycle efficiency. No drum is necessary since the belt is connected directly between the two wings and therefore is always in the air, as long the wings are flying. Moreover, two thirds of the fixing tether is common to both wings, which reduces the drag produced.

Although the second variant's belt has a slower motion than the first, both configurations allow significantly higher reel-out speeds than one third of the wind speed. Therefore, the angular velocity of the drum/sprocket is superior to the ones in typical pumping-cycle system, which eliminates the need for a gearbox before connecting to the generator. However, these systems present other challenges, namely with respect to controlled flight operations or installation/maintenance, which may be critical enough and

thereby precluding this concept from being experimentally implemented to the date.

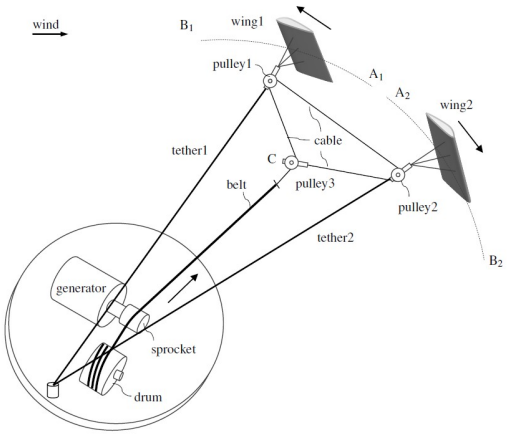

Figure 2.8: Schematic of ultra high speed mechanical power conversion system [67].

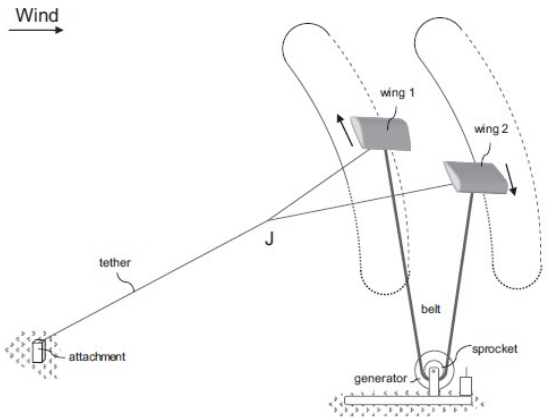

Figure 2.9: Schematic of fast motion mechanical power conversion system [68].

2.3.1.3 "Dancing Kites"

This third variant uses two wings but only one tether to transfer mechanical power [69]. As figure 2.10 illustrates, the wings are connected to the main tether via secondary cables jointed at point J. In traction phase, they fly in anti-symmetric trajectories, which allows the main tether to remain almost static, thus reducing the drag force produced. This allows a greater power output. The re-traction phase also benefits, since the kites can be flown in trajectories where the forces on the secondary cables nearly cancel each other, thus reducing significantly the pulling force in the main tether. Despite these advantages, there are serious challenges for a practical implementation, namely guaranteeing that the flight trajectories in traction phase are completely anti-symmetric, or assuring the kites do not collide in case of turbulence. Therefore, the controllers to be designed are complex and studies are being done [70] using Nonlinear Model Predictive Control [71, 72].

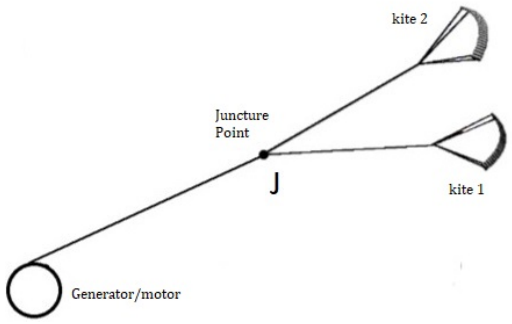

Figure 2.10: Schematic of "Dancing Kites" proposed by Houska and Diehl [69].

2.3.2 Vertical Axis Generator

This is a moving ground-station system, first introduced by KiteGen as "KiWiGen Carousel generator" [73]. It consists of a horizontal circular tensor-structure turning on a vertical axis, whose pivotal center is geared with a conventional alternator [74] - see figure 2.11. Several kite units are connected through tethers to the periphery of the rotor, which has a large diameter (projected to be about $1\,\mathrm{km}$ for $1\,\mathrm{GW}$ of power). The tethers are retractable to allow parking of the kite units in the carousel arms.

The operation of this kind of system is composed by two distinct phases: traction and passive phases, as represented in figure 2.12. For a given wind direction, the flying wings can produce energy for about 300^o of carousel rotation. Thus, in traction phase, the wings have to be controlled in order to pull the rotor arms in the right sense of rotation.

As depicted in figure 2.12, the traction force has to change direction for $\Theta = 270^o$, which implies a change in the kite orientation. Moreover, in this phase, the controller of each kite unit is designed with the goal of maximizing its torque. The produced mechanical power is then computed as the total torque of the kites, in traction phase, times the angular velocity of the rotor, which remains constant. The torque produced by each kite is given by the exterior product between its traction force and its position. The mechanical and electrical efficiencies must be considered after.

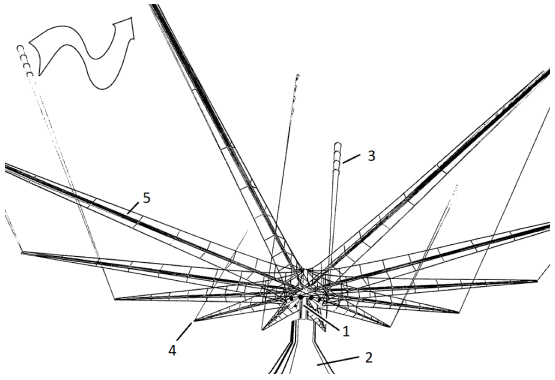

Figure 2.11: Scheme of vertical axis generator. 1 - Vertical shaft; 2 - Electric generator (Alternator); 3 - Kite units; 4 - Peripheral edge; 5 - Rotating arm. Adapted from [74].

The passive phase corresponds to the remaining 60^o of the carousel rotation. Here, since the wings are flying against the wind, energy has to be consumed to drag them through the correspondent fraction of the circular path. As in the re-traction phase described in subsection 2.3.1, the kites are controlled in such a way that power consumption is minimum. With that purpose, this phase can be subdivided in three stages (depicted in fig. 2.12 in gray, red and green): the first and longest is from Θ_0 to Θ_1, where kite orientation is continuously adapted to minimize traction force; in the second (till Θ_2) and third (till Θ_3) stages, the kite is prepared to restart production phase. Simulations have shown that in passive phase only 1% of the generated energy is used [75].

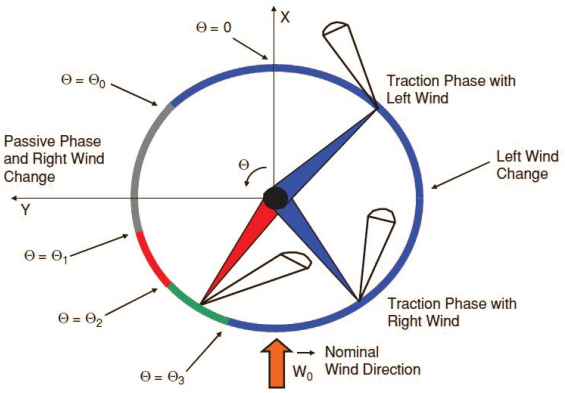

Figure 2.12: Carousel's operational phases [75].

As mentioned earlier, this on-ground crosswind system requires a rotor of large dimensions, which creates the necessity of extensive land areas. In addition, the costs associated to the structure itself are relatively high. Subsequently, the authors of this configuration have proposed an evolution of the concept to a railway generator, which will be addressed next.

2.3.3 Railway Generator

In this type of system, ground stations are integrated on rail vehicles and electric energy is generated from vehicle motion - electric drives are connected to the wheels. The energy generation approach resembles the reverse operation of an electric train. The railways can be open or closed loops . The latter was proposed and studied by KiteGen [76], but only X-wind power plants (NTS-GmbH) experimentally implemented the concept [41]. Schematics of these configurations are presented in figure 2.13.

Besides the control of the kite units to optimize both power production in traction phase and power consumption in passive phase, as in previously presented concepts, regulation of the vehicle speed is required here as well. This is achieved by controlling the electric drives. Two variants were investigated

by KiteGen: constant or variable length of the kite units tethers. On one hand, the first alternative is identical to the carousel configuration described in the previous section - traction and passive phases are the same. On the other hand, the configuration with variable tether length eliminates the phase of purely energy consumption, thus assuring continuous power production. In fact, the operation is based on two phases of energy production: the traction and unroll phases. While the first coincides with the previous traction phases, when the kite units start feeling opposition of the wind and electric drives start acting as motors to drag the vehicles, the wings are reeled-out of a drum and energy is also produced as in a pumping-cycle system [76]. Evidently, the power produced must be greater than the consumed one.

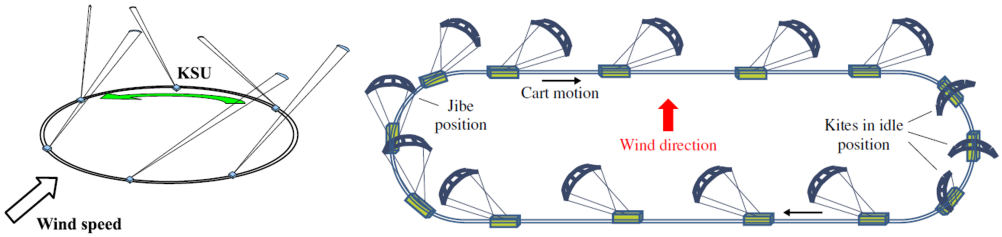

Figure 2.13: Schematic of railway configurations: Circular track by KiteGen on the left; Oval track by X-wind on the right. Adapted from [76, 77].

A comparison between these railway configurations and the KG-yoyo system, mentioned in subsection 2.3.1, was conducted in [78]. It was observed that the constant tether length railway configuration and the pumping-cycle system had similar power outputs. Nevertheless, even though the variable tether length railway system exhibited better maximal overall power generation, it is not enough to disregard its disadvantages, namely higher cost (electrical and mechanical components) and construction complexity. Hence, it was concluded that there were no clear advantages of railway (and by extension of carousel) configurations over pumping-cycle systems.

2.4 On-Board Generation Systems

The second type of crosswind systems produce electric power on-board of the flying wing by on-board wind turbines directly connected to electric generators. In this configuration, the tether remains at constant length, since power is produced not by the traction force acting on the tether but by a drag force D_{power} generated by the turbines. Considering a flying unit with N_{rot} turbines/generators, then the mechanical power produced is [42]:

$$P_{mech} \;=\; D_{power}\, V_a \;=\; \frac{1}{2}\,\rho\, A_{wg}\, V_a^3\, C_{D,power} \tag{2.15}$$

In order to get the electric power output, one must multiply the mechanical power by the generator efficiency. The optimal turbine's drag coefficient is obtained by matching equations (2.15) and (2.9), and by substituting V_a as in equation (2.10). One concludes that the on-board generators have to be projected to increase the intrinsic system drag (from wing and tether) by 50%, as:

$$C_{D,power} \;=\; N_{rot}\, C_{D,rot} \;=\; \frac{1}{2}\, C_{D_{FS}} \tag{2.16}$$

The principle of energy extraction is identical to that of conventional wind turbines, but with extremely lower rotor areas ($A_{rot} = \frac{\pi D_{rot}^2}{4}$) and at a significant higher airspeed due to crosswind. For that reason,

power extraction is subjected to the *Betz Limit*. According to the actuator disk theory [48], the turbine's thrust coefficient (non-dimensionalized by $\frac{1}{2}\,\rho\,V_w^2\,A_{rot}$) is given by $4\,a\,(1-a)$, where a is the induction factor due to the rotor. Thus, the turbine's drag coefficient then results as [79]: $C_{D,rot} = 4\,a\,(1-a)\,\frac{A_{rot}}{A_{wg}}$. By matching it to eq. (2.16), one gets the optimal ratio between turbine rotor area and wing area:

$$\frac{A_{rot}}{A_{wg}} = \frac{C_{D_{FS}}}{8\,a\,(1-a)\,N_{rot}} \tag{2.17}$$

These systems display two main particularities that are seen as advantages with respect to on-ground generation systems. Firstly, they have a continuous power production since there is only energy consumption at take-off (reel-out of the tether until reach desired altitude) and landing (reel-in of the tether) maneuvers, and for staying aloft through a lull in the wind. Secondly, the on-wing turbines can act as propellers, which allows easier take-off and landing operations.

The on-board generators are typically mounted on the wing, hence it must be structurally more sound than in on-ground generation, i.e. of rigid type. The assembly of the generators needs also to guarantee lateral symmetry, in order not to disturb the position of the center of gravity of the aircraft. Moreover, it has to guarantee that the rotors' wake effect do not affect negatively the wing's aerodynamics, namely its lift generation. In fact, unsteady aerodynamic analysis show that the wakes of rotors, mounted as in the prototypes of figure 2.2, lead to an additional increase in force [80]. Another important aspect is to optimize each rotor with respect to the local airflow conditions. The inboard rotors are in a slower airflow than the outboard ones. What is more, the lower rotors also "see" a slower airflow than the upper ones, due to wing recirculation. Makani Power, with their $600\,\mathrm{kW}$ prototype, noticed a great reduction in power produced, since they did not account for this and used the same rotors along the wing.

Concerning the tether, since electricity has to be conducted to and from the ground station, it has to include electric cables and therefore be insulated. For those reasons, these tethers are expected to be thicker than the ones from on-ground generation, thus exhibiting greater weight and drag. Contemplating a reduction of tether drag, systems based on dual airfoils are being studied [81]. This variation, illustrated in figure 2.14, consists in controlling aircraft's trajectories so that the forces on the main tether are balanced, thus minimizing its motion.

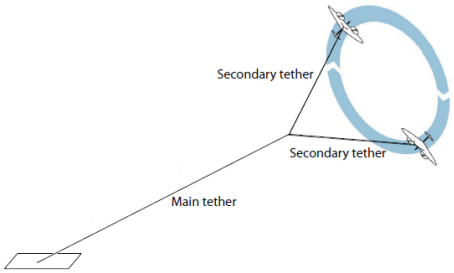

Figure 2.14: Schematic of a dual-airfoil on-board crosswind AWE system [81].

Finally, it is important to mention that these flying units resemble a typical aircraft, hence all sensors and control actuators are on-board. Hence, the ground station only has to assure a platform for take-off and landing, and to handle the electric power.

2.5 Wing Types

The flying wing is arguably the most important component of an AWE system. It must have a high strength-to-weight ratio since it has to withstand large traction loads during climbing and sustaining itself at high altitudes. It must also be controllable in order to be able to operate autonomously (take-off, stay aloft, power production/consumption flight, landing). Moreover, it needs to resist to adverse

weather conditions (e.g. storms) as well as to endure mechanical and chemical wearing (e.g. abrasion, corrosion). Many of these characteristics encompass conflicting requirements to achieve an optimal solution. Therefore, several trade-offs must be made in the design of the flying wing.

Currently, in the industry, both soft flexible wings and rigid wings are being used, with hegemony of the latter (as inquired in 2015 [82]), which are also considered to be more technically mature wings. The following subsections describe in detail the various types and characteristics of soft and rigid wings employed in crosswind AWE systems. Middle rigidity wings are addressed as well.

2.5.1 Soft Wings

Soft wings have been implemented in industry for some time, e.g., in payload carrying systems and meteorology studies [83], so their potential role in airborne wind energy harvesting was easily recognized. Their minimal weight per planform area and compactness, as well as their stable flight behaviour and low manufacturing costs (kite-surfing industry experience) [84] are clear advantages. Moreover, due to the fact they are usually made of fabric, they are more crash resistant then rigid wings.

On the downside, they have a poor depower behaviour (essential for a minimal power consumption in pumping-cycle systems, as seen in subsection 2.3.1), since at that stage there is almost no line tension in the steering system. Soft wings completely rely on line steering systems for control, similarly to kite surfing, thus line tension is a key factor to keep the wings airborne [85]. Another drawback is their lifetime, which is very limited due to the textile involved, so the choice of the material is of extreme importance. Fabrics based on high-tensile fibers (e.g., aramid) were found to be lightweight and to improve durability [86]. The two main types of soft wings are the Leading Edge Inflatable wings and the RAM-Air wings. Both show advantages and disadvantages to be discussed next.

2.5.1.1 Leading Edge Inflatable Wings

The most simple concept of a leading edge inflatable (LEI) kite consists of a span-wise inflated tubular frame on the leading edge (LE) with an attached single lightweight fabric skin called canopy [87]. For steering and transmit power, a set of lines is used and the place of attachment to the kite distinguishes two types of LEI wings:

- **Supported Leading Edge (SLE) kites**: In this configuration, a set of bridle lines is connected to the leading edge and/or to the struts, as illustrated in figure 2.15. These are used to control and maintain the structural shape and orientation of the wing. Specific bridle lines can be pulled to change the kite's angle of attack (power lines - connected to the LE) or to initiate a turn (control lines - connected to the tips) [88]. The lines are actuated by an airborne control pod with micro-winches, at some distance below the wing (Cf. element 10 of figure 2.3). The control pod is then linked to the tether. The traction force provided by the lines in the wing's central region makes the kite flatter than C-kites (see below), which is claimed to improve its aerodynamic efficiency [43].
- **C-kites**: this configuration does not feature a bridle system. The kite lines (one up to four) are directly connected to the tips and they can be controlled both by a flying control unit or from the ground station [89]. Schematics and a practical implementation are portrayed in figure 2.16. The main

characteristics of this kind of LEI wing is its anhedral arc. As the anhedral angle increases (i.e., the kite shape moves more towards a C), the lift forces contribute less to the tether tension, thus reducing power production capabilities (smaller planform area). In addition, drag forces also increase, but since there are less lines used than in SLE kites, this drawback is somehow compensated [90].

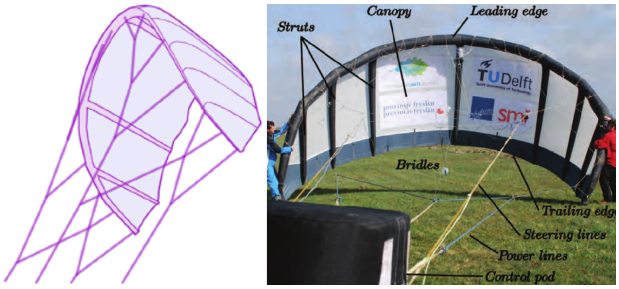

Figure 2.15: Left: Schematics of the bridle system of a supported leading edge kite. Right: SLE from Kitepower captioned. Adapted from [43, 89].

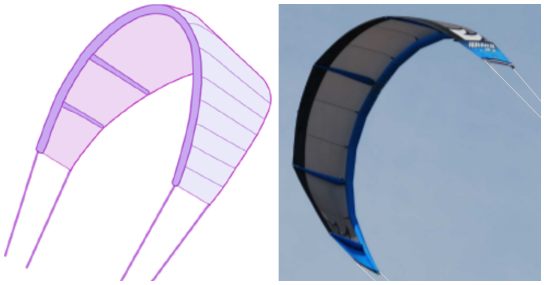

Figure 2.16: Left: Schematics of the C-kite lines. Right: North Rhino C-kite. Adapted from [43, 89].

In general, SLE kites are preferred to C-kites, as it is the case of KiteGen [34] and KitePower [39].

The structural components of these wings are the span-wise inflated leading edge and the chord-wise struts. The LE profile is typically circular and the larger its diameter is the more stable the kite is, hence more power it can provide. However, this brings a scalability issue, since the tubing must be oversized in case of large wings [43]. The struts act as wing ribs and influence its power and stability. Structural resistance of the kite increase with the number of struts, thus providing more power and stability to its flight [91]. Nevertheless, that leads to a larger mass and subsequent negative effects, such as the need for stronger wind speeds for take-off or steeper operational elevation angles. Detailed structural studies are provided in [89, 92].

In terms of aerodynamics, the lightweight flexible construction of the wing allows it to greatly deform while flying, hence influencing significantly the flow field - it carries a poorer aerodynamic performance than other soft wings. Some studies show that, in order to upgrade the role of LEI wings in pumping-cycle generation, the aerodynamic performance of the LEI kite could be improved by delaying the boundary layer transition during the traction phase and triggering it in the retraction phase [93]. Although its great flexibility brings negative effects on aerodynamics, it still allows the wing to operate at a wider range of angles of attack (than RAM-air wings), thus giving it better depowering capabilities [94]. Beside the already mentioned investigations, comprehensive studies on the aerodynamics of these wings are reported in [95] (modeling with non-linear vortex lattice method), [96] (airfoil optimization), [97] (aeroelastic simulations), [98] (experimental aerodynamic characterization), and [99] (influence of chord-wise struts on aerodynamic performance).

2.5.1.2 RAM-Air Wings

A ram-air kite, also called foil kite, is a hollow double skin soft wing. It is normally composed of ribs, top and bottom skins, lines, and eventual risers. The space between two ribs is a cell. Figure 2.17 illustrates a labeled schematics of a ram-air wing and a picture of the SkySails Power kite [33] (Kitenergy [37] also uses this type of wing).

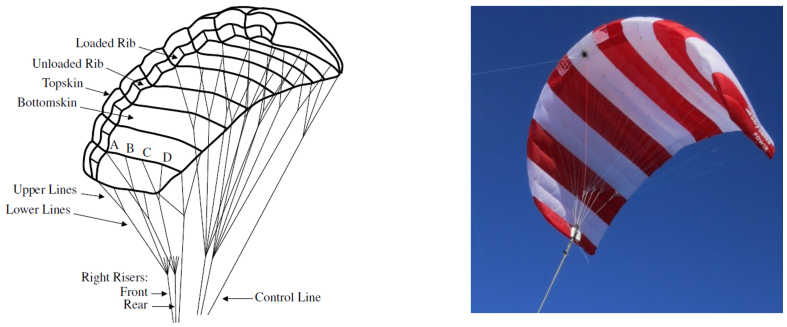

Figure 2.17: Left: Ram-air wing components. Right: SkySails Power wing. Adapted from [100, 101].

This kind of wing typically does not contain any rigid elements (the ribs are made of fabric as well), and it can deflect, twist and fold in ways LEI wings cannot. Moreover, it does not require pre-inflation, as its stiffness and aerodynamic shape are acquired in-flight [100]. In fact, this wing is inflated with high pressure air that is forced into the wing through openings at the stagnation line (region of maximum air pressure in a wing section) on the wing's leading edge. The wing should operate at relatively high angles of attack, so that the stagnation line stays over the air intake, preventing air to flow in and out [102].

The structural elements of a ram-air kite are the ribs. The control and power lines are attached along their chord (in order to reduce drag), thus they need to sustain high tension loads. For that reason, they contain fabric reinforcements, whose layout has a strong influence on the wing profile during flight as well as on the lifetime of the fabric [103]. Another characteristic of the ribs is that they have holes to allow span-wise internal airflow for pressure equalization, incidentally providing also a reduction in weight.

In terms of aerodynamic performance, it is greater than in LEI kites, besides having a more dense bridle line system which increases drag. This is due to the larger thickness and planform area of these wings, that come at the expense of a greater weight. Detailed studies on the wings aerodynamics were done in [102], and in [104] and [105] about its aeroelastic behaviour.

Finally, although this type of wing does not exhibit scalability issues, its greatest limitation is the need for a very specific and stable planform, trim and anhedral arc (essential for flight stability), whereas a LEI wing, for example, display a much wider range of wing geometry options. All the design constraints are well described in [100] and included references.

2.5.2 Rigid Wings

While soft wings were considered due to their previous history in handling high tensions, rigid wings, were taken into account because of their employment in conventional aircrafts. The several decades of experience in developing and optimizing them constitute a good advantage. In AWE, these wings are always used in on-board generation systems, as in [27–29], but they are also utilized in on-ground generation, as in [30–32, 36, 38]. In fact, in case of pumping-cycle generation, rigid wings are claimed to have faster and more efficient traction phases [106].

This kind of wings has a much superior aerodynamic efficiency due to their high aspect ratio, to the usage of profiles with high *glide ratios* [107] and to the fact they almost do not deform. Therefore, the wing withstands great aerodynamic loads which cause high bending moments [108]. In addition, in case of on-board generation, the wings have to support the generators too. Hence, the wing is usually

made of carbon or glass fiber composites [103]. These materials, although more expensive and denser than fabric, have excellent strength-to-weight ratios and are very resistant to wearing, both chemical and mechanical [109]. Thus, with regular maintenance, rigid wings have a substantial higher durability, which provides high process repeatability.

However, these advantages come at the price of more expensive manufacturing and of a higher system mass, which limits their performance on low wind speed conditions [43]. For example, it has higher cut-in speeds (minimum wind speed for operation) and it implies an external power source for taking-off (e.g. on-board propellers, launching mechanisms). However, one should mention that due to the substantially higher aerodynamic performance, for the same intended power output, rigid wings with smaller areas can be used. Thus, the increase in the weight per planform area ratio may not be that large. Another disadvantage is that, in case of an accident, it is unlikely to recover the wing undamaged.

The controlled flight of these wings is typically achieved using on-board actuators, as a typical aircraft with tail and fuselage (gliders): elevator for pitch, ailerons for roll and rudder for yaw. This adds extra mass to the wing and the need to have thicker tethers to pass communication cables, even though that necessity was already entailed by the high aerodynamic loads, leading to higher traction forces, and by the electricity conduction in case of on-board generation. In order to reduce weight and reduce complexity of the wing by eliminating some actuators, control lines can steer the wing, similarly to a kite, as it is done by TwingTec [84].

Another type of rigid wing is implemented for on-ground generation by EnerKite [36]. It has a smaller mass, since there is no fuselage nor tail, and it does not require on-board actuation. This company uses a swept rigid wing, whose flight control and stability is achieved by a bridle system [110] and by the sweep angle. Moreover, this wing requires a mechanical system for launching, such as a rotating arm.

Finally, one mentions the concept of morphing wings which are rigid wings with the potential to achieve optimal performance at different flight conditions by tailoring their airfoil shape and lift distribution at different levels along the wingspan [111]. For example, in a pumping-cycle system, one can the adapt wing shape to maximize the *glide ratio* while in traction phase, and then adapt it to minimize the drag coefficient to the retraction phase.

2.5.3 Other Wing Concepts

In this section one mentions three other concepts of wings that were studied and implemented. Firstly, one addresses the concept of the kiteplane [112], illustrated figure 2.18(a), which was thought in order to combine the lightweight flexible membrane design of soft wings and the favourable control characteristics of gliders [113]. Several versions were tried, but durability, scalability, and ultimately controlability and aeroelastic phenomena led to the abandonment of the concept [88].

Secondly, inflatable kites using the concept of tensairity were tackled - figure 2.18(b). These kites combine inflatable structures with struts, cables and fabric webs in the airbeam. This allows to build lightweight wings with larger aspect ratios and to integrate properties as dihedral, sweep and twist in a way regular soft wings cannot [114]. Some of these concepts were then introduced in the LEI wings.

Finally, KiteGen introduced a semi-rigid curved wing that aims to be lightweight, as soft wings, and

to be able to handle high loads, as rigid wings. As depicted in figure 2.18(c), this wing is constituted by 9 ashlars hinged together by flexible joints, thanks to which it can easily change configuration in order to vary the wing lift distribution [115]. Therefore, the aerodynamics of each curvature should be target of analysis [116] in order to maximize performance. The controlability of these wings is harder than for regular soft wings.

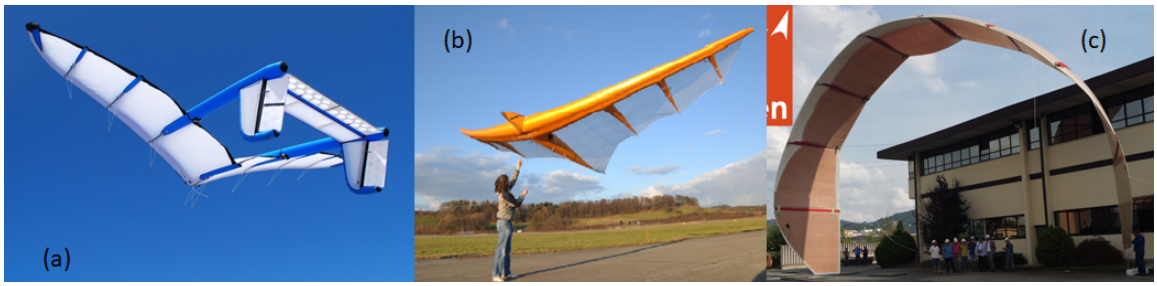

Figure 2.18: Other wing configurations. (a) Kiteplane configuration; (b) Inflatable Kite using tensairity; (c) Semi-rigid curved wing of KiteGen. Adapted from [88, 114, 115].

2.6 Tether

The present section aims to state important considerations about the tether that are inherent to all AWE crosswind systems. The function of this crucial component is, as previously mentioned, to connect the flying wing(s) to the ground station, restraining its flight movement. Therefore, it has to withstand a high traction force which arises from the aerodynamic forces generated by the wing. Hence, the tether is designed to handle a maximum load which should not be outstripped within the flight - it is necessary active control to guarantee it.

The maximum allowable load is a main design criteria for all systems. In addition, on-board generation systems have to consider the conduction of electrical power through the tether, and pumping-cycle systems have to account for the bending behaviour. Thus, with the purpose of designing the tether for a certain system, creep lifetime and bending fatigue checks have to be performed, and these must satisfy a certain expected lifetime [117]. To make considerations about the tether lifetime, three important parameters should be defined: material (breaking strength), dimensions (e.g. width and length), and construction type.

An obvious choice for the tether material is a high performance fiber that has an elevated strength-to-weight ratio. This characteristic not only reduces the impact of gravitational forces on power production, but also allows tethers to have smaller widths, thus reducing its drag. An example is the Ultra-high-molecular-weight polyethylene fiber (e.g. Dynemma® [118]), that not only has a great creep resistance, but also a good abrasion resistance (very beneficial for offshore sites for example) and ultraviolet stability (important for on-board generation systems).

In terms of construction, there are two main types of tethers, depending on the interlacing technique: Laid or Braided tethers - see figure 2.19. The latter is mostly used, since it does not twist when subjected to a load and it has a hollow core that can be used for example to contain conductive cables for electricity transfer or communication.

Besides the tensile loads, one needs also to consider the aerodynamic drag, centrifugal force and gravitational force, which lead to tether sag [119]. It influences the wing angle of attack, thus reducing power production efficiency. Numerical simulations show that the peak of power production occurs when sag disappears and the tether straightens out [120] - maximum traction force. As the wind speed increases, this force also increases, but the tether sag angle remains almost the same [121], which is important for the stability of the wing movement.

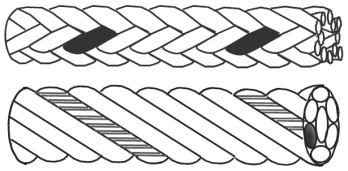

Figure 2.19: Top: Braided; Bottom: Laid [117].

The aerodynamic drag forces are mainly due to the tether dimensions, geometry and aero-structural phenomena. As pointed out by equation (2.5), the larger the tether's width, length and $C_\perp$, the greater the drag. Therefore, it is clear that systems that require conductive cables inside the tether have increased aerodynamic resistance. With respect to the dynamic effects, vortex-induced-vibration (e.g. lock-in) and galloping phenomena can increase the drag up to 300% and 210%, respectively [122]. This effects have to be carefully studied. An option proposed to make the tether less susceptible to all forms of vibration-induced drag and to reduce $C_\perp$ (when compared to the traditional circular-section shape) was a faired tether, whose cross-section is streamlined [123]. This tether has a flow-alignment passive mechanism to guarantee the mentioned positive outcomes. It is also relevant to mention that the larger the AWE system is, the less sensitive to tether drag it becomes [124].

The centrifugal and gravitational forces depend on the tether mass, which is directly linked to the operational altitude. As the latter rises with the purpose of increasing power production, the tether length and consequently its weight (and drag) grow. The direct implication is in the operational elevation angle - it has to be larger, leading to an increase in gravity-caused *cosine losses* [124]. It is then obvious the existence of an optimal operational altitude.

Finally, the tethers play an important role in assuring the ground station integrity, namely the generator safety (for on-ground systems), when thunderstorms occur. The tether may trigger a flash-over along its surface, conducting downwards a huge amount of electric power, which may damage the generator [125]. Hence, lightning protection systems and good cable insulation have to be considered.

2.7 Take-Off and Landing Approaches

This section aims to present different studied and implemented strategies for launching and landing the previous AWE crosswind systems. The necessary platforms/mechanisms are the main constituent of the ground station (apart from the generator). The ground station provides the supportive structure and the power, if it is the case, for these maneuvers to occur. The alternatives depend on the type of wing since rigid wings and soft wings really vary on mass and flight behaviour, thus requiring distinct approaches. At the end of this section, one addresses the possibility of using a tower.

2.7.1 Approaches for Rigid Wings

The take-off approaches for rigid wings may be divided in linear and rotational motion. Furthermore, in linear take-off, one can have vertical or horizontal motion, as follows.

2.7.1.1 Linear Horizontal Take-Off and Landing

The idea for this approach is to resemble the take-off and landing of a typical aircraft, by using a runway (with specific tracks). In order to reduce the platform dimensions, one uses an external power source to faster accelerate the flying unit. It can be either by using a catapult technology or by using the winch that unreels the tether.

The first option is used if no additional power is available during climb. Therefore, all the energy necessary to reach the operational height has to be ”in” the aircraft as kinetic energy, since the take-off. The high acceleration is obtained by using a linear induction motor [126]. One example of this solution is the Electro-Magnetic Aircraft Launch System (EMALS) [127].

In the second and most common option, the aircraft has one or two on-board propellers, so that after launching with high acceleration, they can be employed to sustain the forward speed during the climb to the operational altitude. While still in the ground station, the tether passes through a series of pulleys, the last of which is installed on a slide able to move on linear rails [129]. This slide is controlled by a motor who gives the necessary power for acceleration [130]. One of the companies using this alternative is Ampyx Power [131], and as seen in figure 2.20, it is a quite compact solution. Its platform is omnidirectional (it can rotate), in order to align with every wind direction.

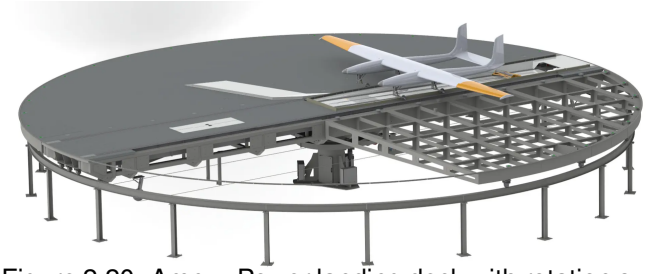

Figure 2.20: Ampyx Power landing deck with rotation system [128].

For landing, in both options, the tether is controlled to help the aircraft aligning with the railway tracks. The landing speed should be small, but some breaking mechanisms may be necessary.

2.7.1.2 Linear Vertical Take-Off and Landing

In this approach, the aircraft is equipped with propellers which provide enough thrust to overcome the flying system weight and take-off vertically. It implies only a platform with more or less the size of the aircraft, similar to a heliport. Thus, it requires a small land occupation.

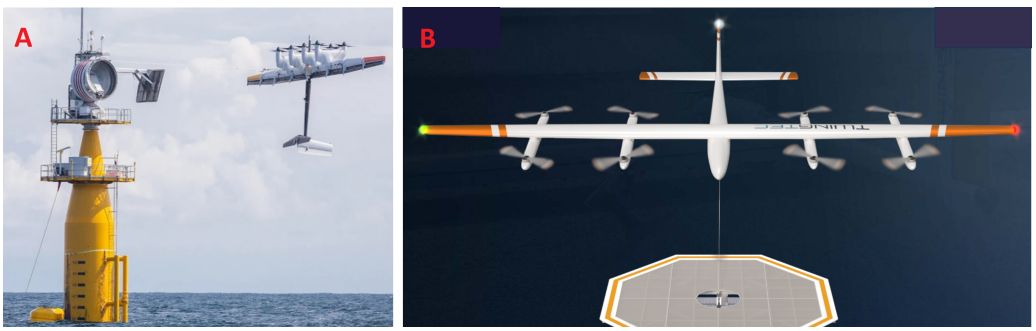

Figure 2.21: A - Vertical Take-Off approaches from Makani Power; B - TwingTec [27, 32].

The propellers can be assembled just like a quadcopter, as TwingTec and Kitemill do (see figure 2.21 on the right), or just like a typical airplane, as Makani Power and Kitekraft do (see figure 2.21

on the left). In the latter, it is necessary to tilt the aircraft vertically in order to use the propellers, and when the operational altitude is reached, a transition phase starts to reset its normal orientation [132]. This approach is taken due to the on-board generation mode, but it requires a very reliable controller to guarantee a stable take-off. It was shown that this alternative is not robust against high wind velocities [133]. In addition, if it is a tail plane configuration, it requires a certain elevation of the ground station.

When the propellers are mounted as in a quadcopter, then if the operation is in *Drag-mode* they would have to be tiltable in order to regain an orientation parallel to the aircraft. If it is the case of *Lift-mode*, then they are turned off and the blades are retracted so that they have a smaller drag contribution.

2.7.1.3 Rotational Take-Off and Landing

In this approach, the hull of the aircraft is initially attached at the tip of a rotating arm. The roll angle of the aircraft at this point depends on the elevation of the platform. The rotation will generate aerodynamic forces, as well as a centrifugal force, which will reel-out the tether and drive the aircraft in a helix flight path [134]. When the operational altitude is achieved, the rotation is slowly stopped. In order to facilitate the take-off, a tilting platform can also be considered [135]. This strategy was first studied at KU Leuven and a control strategy was developed [136]. Regarding landing, the operation is reverse: the tether is slowly reeled in until the aircraft attaches itself to the rotating arm.

Currently, for rigid wings, only EnerKite exploits this alternative, mainly due to the fact they use a swept rigid wing, thus being easier to hold it in the arm. Moreover, in order to increase the airflow at the wing while rotating and to increase the launching height, a telescopic arm is used. Pictures of the system are showcased in figure 2.22.

Figure 2.22: Enerkite rotational arm system [36].

2.7.2 Approaches for Soft Wings

With respect to soft wings, the take-off strategies can be divided in passive and active approaches. Passive approaches count only on the wind speed at the launching platform to generate enough lift force on the kites. Due to the wind shear, the wind speed at the ground generation is typically low, so it is used an arm or mast (might be rotating and telescopic or not) in order to elevate the kite to heights where the wind speed reaches the cut-in values. Companies such as SkySails Power and KiteGen currently pursue this strategy - see figure 2.23. The latter, since employs a LEI kite which starts upside down,

may use on-ground fans to generate airflow to lift the kites. The landing is simply done by reeling in the tether with minimal energy consumption [137].

Active approaches were suggested but not implemented yet, mainly due to the fact they introduce extra airborne mass, power consumption or costs that are seen as not worth it. Nevertheless, further studies are being carried. One option suggested was the use of propellers on the control pod that would generate enough thrust to take the kites to cut-in wind speed altitudes [138]. A downside of this approach, besides the mentioned above, is the fact that the propeller's wake induces an opposing lift force on the kite, which would have to be overcome. Another option proposed was the use of an aerostat to take the kite to operational altitudes by using the buoyancy of a lighter-than-air gas [139].

Figure 2.23: SykySails Power (left) and the KiteGen stem (right) take-off platforms [33, 34].

2.7.3 Use of a Tower for Take-Off

The use of a tower in AWE systems is also considered due to its advantages on reducing the elevation angle of the wing, on reducing tether mass and drag (shorter tethers are necessary), and on facilitating take-off and landing maneuvers [52]. The cost of these towers is significantly lower than for conventional wind turbines. It may be a steel framework supported by suspension lines which reduce the bending moment absorbed by the tower itself and its foundations.

In a linear horizontal take-off approach, the tower would allow for a tilted runway, which would lead to a highly upward take-off; in landing, it would eliminate the necessity for breaking systems since the kinetic energy could be transformed in potential energy to overcame the inclination.

In a linear vertical take-off approach, it would easily allow longer tails and eliminate the necessity of tiltable propellers. On top of the tower, a heliport could be placed for systems like TwingTec's.

In rotational approaches, it would allow easier holding mechanisms of the aircraft since 90^o roll angles would be possible.

Passive approaches for soft-wings already employ towers to reduce cut-in wind speeds.

Besides the advantages previously described, the use of towers would only imply a small land occupation, thus the surroundings could be utilized for other activities such as agriculture, in case of on-shore generation. Furthermore, the steel framework tower, after its lifetime, has a high recyclability.

The disadvantages of using a tower are the increase of material demand, of construction and maintenance costs, of installation complexity and of the visual impact.

Chapter 3: Key Factors for Design Choice

After presenting the types of crosswind airborne wind energy generation and its fundamentals, after introducing the different existing system configurations, and after displaying the main variants of its components/subsystems (flying wings, control systems, tether, taking-off/landing mechanisms/platforms), one addresses the most relevant factors that should be taken into account when deciding for a certain AWE system. The identified factors have been categorized into five distinct classes: Technical Design Factors, Operational Factors, Manufacturability, Logistics, and Social Acceptability Factors.

3.1 Technical Design Factors, TDF

This class concerns factors related to the airborne subsystems performance, namely the flying wing and the associated tether and steering system (if it is the case).

3.1.1 Aerodynamic Performance, AP

Aerodynamic performance is one of the major design drivers of an AWE system, specifically of the flying wing. As seen in equations (2.9) or (2.14), the term $C_R \left({}^{C_R}/_{C_{D_{FS}}}\right)^2$, which in aerodynamically efficient crosswind systems can be approximated by $C_L \left({}^{C_L}/_{C_{D_{FS}}}\right)^2$, appears to be critical to achieve maximum power production. In fact, a global sensitivity analysis done in [140] showed the high dependency of the annual energy production on the aerodynamic performance.

For this matter, there are two possible ways of thinking, which do not bring consensus yet: maximizing the *glide ratio*, which appears squared, or maximizing the lift coefficient, which appears to the power of three, at the account of a substantial increase in the kite's drag coefficient C_D. The second option was suggested for on-board generation, in [141], and it was implemented by using a biplane rigid wing, just like Kitekraft prototype [28]. The simulations showed that, despite having more wing and tether drag, this option led to higher power production and economical profits than a monoplane, besides maximizing strength-to-weight ratio of the airframe. Simulations performed in [142] also show that wings with higher C_L lead to a higher production, although being disadvantageous for low wind speeds. Regarding the first option, [140] showed it was better to have extremely low drag and moderate lift, specially for on-ground generation (pumping-cycle) since, for traction phase, high C_L was required but, for retraction, small C_D, specially C_{D0}, was essential.

The previous considerations are very much linked to the airfoil characteristics. For a more direct comparison, one may say that rigid wings have significantly better aerodynamic performance than soft wings: ${}^{C_L}/_{C_D} \sim 20 - 35$ for rigid [124] and ${}^{C_L}/_{C_D} \sim 4 - 10$ for soft [85, 89]. Between soft wings, RAM-air wings are the ones who perform better.

In order to minimize wing drag, wings with an elliptical lift distribution are better, as well as, wings with higher aspect ratios ($\mathcal{AR}$), however, $\mathcal{AR}$ larger than 10 do not constitute a major benefit [84]. Moreover, in case of soft wings, it is more aerodynamically beneficial to reduce the anhedral angle than to increase

aspect ratio [143].

In addition, it is important to mention that several simulations have shown a major negative impact of tether drag in small-scale systems performance. The tether aerodynamic resistance is higher in the case of on-board generation, as the thicker the tether, the larger the drag. Solutions as the ones in figures 2.10 or 2.14 constitute improvements in this matter.

To sum up, one may note that, simply based on the foregoing discussion, an on-ground generation system with a rigid wing seems more promising.

3.1.2 Mass-to-Area Ratio, MA

The mass and size of an AWE system are directly associated with the rated power for which it is designed. Higher rated powers imply larger masses and sizes. What is most important achieve is the smallest mass-to-area ratio m/A_{wg} possible for a desired power.

As seen in section 2.2, the heavier the system, the larger the *cosine losses*, the smaller the power extracted from the wind. Larger masses also lead to higher inertia loads and increase the necessity for stiffer airframes and tethers. Another major implication is the increase of the minimum wind speed for take-off and operation, which has a strong impact on the potential of power production in a given site. Tether weight is also an important factor. The higher the operational altitude, the longer the tether and consequently its weight. The same happens with thicker tethers.

With respect to the flying wing size, larger areas are in general better, since these allow higher power outputs (e.g., eq. (2.9)), larger swept areas while flying, and reduce the impact of the tether drag [124]. Nevertheless, the way area is increased must be well thought, in consideration of the structural mass needed. Not very high $\mathcal{AR}$, as suggested in the previous topic, means larger chord lengths which implies thicker wings (structurally more stiff) and therefore reduced structural weight [140]. Providing large wing planform areas with a small weight is then optimal since more energy can be harvested at low wind speeds.

Thus, in order to achieve a small m/A_{wg}, the use of soft wings is preferable, with slight advantage to LEI kites. When using rigid wings, on-ground generation system will be lighter since the flying wing does not have to carry generators.

3.1.3 Durability, DU

Durability is a term that defines the ”period of service life of a given material or system under specified conditions of outdoor and indoor climate and construction of the assembly” [144]. Therefore, it is straightly related to the properties of the materials used in each subsystem and to the exposure conditions. When a system is designed, a certain lifetime comes along with it and this should be as long as possible. However, longevity has to be coordinated with maintenance and replacement costs. For example, a system can have a shorter lifetime but have a replacement cost that is inferior to the overall maintenance costs of another system with longer projected lifetime. A trade-off has to be achieved and that can be complex.

In this framework, one can assess the durability of the flying wing based on its materials. Soft wings

use fabric, while rigid wings use glass or carbon fibre composites, which are much more structurally reliable. Therefore, these will resist longer to bending, shear and torsion loads, as well as to wearing. Thus, for such wings, the maintenance is expected to be less regular and less costly.

Regarding tether durability, it is expected to be typically lower for on-ground generation systems, namely for pumping-cycle generation, due to the reeling cycles which lead to fatigue and are associated to high bending moments. In on-board generation, despite also being subjected to high traction forces, these are more constant in time. Hence, the mechanical failure is usually due to creep, and that takes longer to happen.

Concerning the durability of the entire system, one can say that the higher the number of components, the higher the expected maintenance costs. However, as addressed, the durability issues are generally related to the airborne components, not to the ground station.

Worthy of mention is the fact that the relevance of this factor depends on the site conditions in two aspects, as follows. It becomes higher as the potential of the site to harm the system increases (e.g., offshore sites induce stronger wearing), and the accessibility for maintenance decreases (e.g., a remote location will impose extra limitations on maintenance procedures).

Taking all the foregoing considerations into account, an on-board generation system seems more promising in terms of durability. The sensitivity analysis done in [140] concludes the same in terms of profit, as long as the kite is rarely or never replaced.

3.1.4 Survivability, SU

This criterion refers to the capacity of the system to remain operational with small or none reparation after a malfunction or accident. This factor can be essentially assessed based on the cost of replacement of the system and on the existence of mechanisms of adaptation to hazardous conditions (e.g., extreme wind conditions).

Regarding the flying unit, although rigid wings exhibit higher durability, for the same reasons they have lower survivability in the event of a crash. This is exacerbated in the case of on-board generation, due to the usual vulnerability of on-wing turbines to such events. When comparing solely soft wings, LEI kites have lower survivability, mainly because of the pre-inflated leading edge, which is tougher to recover. A RAM-air would probably be damaged in one of the skins and these could be more easily patched. Also, in case of tether break or detachment, systems with other connections to the ground station (e.g. on-ground steering system) or with on-board controllers have higher survivability as well.

3.2 Operational Factors, OF

This class concerns factors related to the whole energy production operation of the system, namely the capability to supply energy continuously, the ability to have an automated controlled flying unit and the complexity of the take-off/landing subsystems.

3.2.1 Continuity of Power Production, CPP

The capability of supplying electric energy without oscillations leads to a simpler ground station and connection to the grid, since it requires less electrical rectification elements, such as capacitors and batteries, in order to keep providing steady electrical power to the grid [43].

Therefore, in this matter, on-board generation systems are preferable since ideally there is only power consumption at the beginning and ending of the operation (for take-off and landing), whereas in on-ground generation (exception made to the second variant described in section 2.3.3) there is a highly discontinuous power output - see figure 2.6. However, this weakness can also be offset when integrating several systems dephased in a wind farm [145].

With respect to soft wings, as LEI kites show better depower capabilities than RAM-Air wings, they have shorter retraction phases, thus a larger continuity in power production.

3.2.2 Controlability, CTR

The study of the characteristics of the existing control strategies are out of the scope of this thesis, thus for that matter the reader is referred to [146], which is a review on two decades of advanced control research. Nevertheless, controlability of the systems is an extremely important factor for AWE, since it is the main feature to allow for fully automated operation, which is absolutely mandatory for a safe and reliable system [147], and its posterior commercialization [148].

Rigid wings have a more reliable automation and controlability, as their geometry is always well defined [149]. The dynamics of a typical aircraft is simpler to model than of a soft kite and it has been done for several decades. The experience on designing controllers for aircrafts is also way longer than for soft kites. Moreover, the actuation surfaces of a rigid wing are more efficient since they are on-board (minimal lag between input and response). Therefore, the only drawbacks are the necessity of a power supply (on-board or via cable, which leads to an increase of weight) and a communication link between the ground station and aircraft (via cable, which leads to an increase of tether weight; or wireless, where problems may arise with long distances).

Concerning only to the control of soft wings, it can be done from the ground station by implementing the steering and depowering actuators as part of it or from an airborne control unit which controls a bridle line system through micro-winches. The main advantages of the airborne control pod are the minimal mechanical delay between activation of the micro-winches and dynamic response of the wing, as well as its use for a more precise wind speed measuring. Furthermore, with this option the kite can still be controlled if the main tether ruptures. However, the airborne unit requires, as in rigid wings, a power supply and a reliable long-distance communication link to the ground [150]. Although the first alternative eliminates the added mass of an airborne unit, the multiple tethers increase aerodynamic drag. From industry developments, the best alternative seems to be the airborne kite control unit.

Finally, regarding control of the operation itself, it is clear that on-board generation yields reduced complexity compared to on-ground, since it has a continuous phase of power production.

3.2.3 Take-Off / Landing Feasibility, TLF

The take-off/landing systems should be as simple as possible since that means the associated costs are as lower as possible and the controllers are easier to develop. Moreover, it should allow for an automated and safe operation for the same reasons discussed earlier.

Regarding rigid wings, a linear vertical take-off/landing maneuver as used by TwingTec or Kitemill (not Makani Power) has the smallest complexity, since it requires the smallest ground area and the system has the ability of hovering. However, numerical simulations [151] allowed to conclude that the best alternative from a technical and economical point of view is a linear horizontal take-off maneuver with a ground acceleration phase and on-board propellers, as described in subsection 2.7.1.1. It requires less on-board propellers, which significantly reduces weight (specially when scaling-up) as well as increases aerodynamic performance. Moreover, it uses the winch that is already employed in power generation, hence the ground station complexity is not large.

With respect to soft wings, a passive approach seems the better option since it does not add extra mass and drag to the flying system. In addition, a sensitivity analysis available in the literature [140] have shown that the construction of a tower may be attractive, specially in sites where wind speeds at the ground station are low, but further studies should be followed.

3.3 Manufacturability, M

This class/factor concerns the complexity and costs of manufacturing AWE systems. It is clear the need for a feasible and reliable system, which should be obtained with the least possible complexity as well as employing materials with the most availability possible. In this way, the costs involved in the fabrication processes will be the smallest possible.

Regarding the airborne components, the manufacturing of the tether for on-board generation becomes more challenging and costly since it has to incorporate electric cables and to be very well insulated. The same can be said about on-ground generation which require a wired communication with the ground station. With respect to the wing, the composite materials and construction processes involved in rigid wings are significantly more costly [152], however with a decreasing tendency in time (integration of technologies such as digital manufacturing and 3D printing) [153, 154]. Although the materials and fabrication processes for soft wings are generally cheaper, since these are essentially manufactured using cutting tables and sewing machines, as their size scales up, additional challenges emerge [100], thereby levelling the differences between the two types wings, in this factor.

The nominal power of a system is usually a major cost driver, thus the generators, electronics and gearboxes (when applicable) also influence the system fabrication cost [155]. Firstly, the use of a gearbox is preferably disregarded due to its high manufacturing and mainly maintenance costs. Hence, direct drive permanent magnet generators are generally used [156]. However, this brings challenges in synchronization and controlling voltage [157]. Moreover, electronic components for energy storage (e.g. capacitors, batteries, flywheels) are also to be accounted for an economically viable fabrication of the system. It was shown that, for low-to-mid altitude ranges, ultracapacitor-based systems are the most vi-

able, whereas for high altitude, ground stations equipped with advanced batteries (such as sodium-sulfur and flow batteries) are the most adequate [158]. Furthermore, a former published sensitivity analysis [140] allowed to conclude that the electronic cost for on-board generation is lower than that of on-ground generation.

3.4 Logistics, L

The logistics complexity and respective costs are mainly linked to the size of the systems and number of components. Facilities for manufacturing, packaging, installation, and maintenance will all be sized around the system, therefore using smaller units may lower costs at multiple points in the supply chain. For transportation, shipping anything that can fit in a standard shipping container will be significantly less expensive than shipping anything that requires special accommodations [159].

Referring to installation only, the ground station and associated subsystems such as the take-off / landing platforms are the key players. The higher the number of components and the complexity of the foundations, the worse regarding the assessment of this factor. Therefore, systems as described in sections 2.3.2 and 2.3.3 are the worse in this aspect. Moreover, systems whose take-off platforms require towers or masts may need stronger and more complex foundations.

Finally, it is relevant to mention that the importance of this factor grows with the difficulties of accessing the exploration site.

3.5 Social Acceptability Factors, SAF

This class concerns factors crucial to the social acceptance of the systems, namely the visual and noise impact, the effects on the ecological environment and its safety. It is noteworthy that this class becomes more relevant the closer to an inhabited area the system is installed.

3.5.1 Visual Impact, VI

The visual impact of AWE systems is considered to be lower than of conventional WT, due to the fact that these systems fly at greater altitudes and do not occupy any airspace while off-operation [148, 160]. The visual impact is as lower as the airborne system is smaller and its flight path is aesthetic. In terms of size, it is obvious the smaller impact of rigid wing systems. Relatively to the visual appeal of the flight trajectories, the advantages are towards the *Drag-mode* operation as it operates continuously in figures of eight.

Regarding the ground station, the visual impact is rather low, but distinctions can be done: Vertical Axis and Railways Generators are the largest systems, thus having the highest visual impact. Moreover, ground stations with towers may be considered less visually appealing than the ones with flat take-off platforms.

3.5.2 Noise Impact, NI

Similarly to visibility of AWE systems, the sound emissions are also expected to be lower than for conventional WT. Noise may lead to annoyance in people, which includes health complaints such as

sleep-disturbance, thus it is of great importance to comply with local noise limits [160]. These disturbances are reported for sound pressure levels over $40\,\mathrm{dB}$ [161].

The main source of sound is the generators. For on-ground generation, the generator is on the ground station, so if this is built soundproof, the noise effects are negligible [162]. This option is not available for on-board generation, hence these systems have the highest noise impact.

3.5.3 Ecological Impact, EI

Another relevant factor for social acceptability is the impact of AWE systems on the local fauna and flora, and on the migrating species that may use the airspace of the exploration site. Currently, there is not enough knowledge about how wildlife will interact with these systems, but some comparisons can be made with aviation, conventional wind turbines and power lines.

The most decisive aspect was determined to be the mortality caused by the moving aircraft and tether. A study done by Ampyx Power for its rigid wing system led to an expected number of fatalities (birds and bats) of 13-24 per year, for an all year round operation with a $1\,\mathrm{km}$ long tether in a site with moderate bird activity [163]. These values were comparable to the ones registered at conventional WT, which shows not to be a very critical factor. In fact, in other studies, the potential impact of an AWE system was found to be low [164, 165]. Even so, ecologists and biologists recommend avoiding known sensitive or high-abundance sites, including bat roost locations, orographic uplift areas preferred by eagles, and prairie grouse lek sites [166]. Moreover, including bird impact detection systems, as in [167], may be considered.

Among the various AWE systems, one may say that the ecological impact of soft wings will be slightly smaller than the one of rigid wings, due to the fact the kites' areas are larger, thus more visible to animals, as well as more likely not to produce a collision. Among rigid wing systems, as on-board generation is louder, it may also reduce the probability of collision.

3.5.4 Safety, SF

The proof of safe operation of AWE systems is a critical factor for social acceptance, thus regulations must be enforced in order to certify these systems [168, 169]. For the purpose of the present study, the relative safety of these systems can be assessed by considering the risks involved for human life and property in case of a failure and crash of the flying wing. People might perceive soft wings as safer than rigid or hybrid wings due to the use of lighter materials [149]. However, that smaller risk is not that clear, since one may note that soft wings are more likely to cause harm due to an uncontrolled crash [160] (rigid wings have higher controllability, as seen in subsection 3.2.2). Furthermore, the mode of electricity production also influences the social perception of safety: the use of on-board generation might raise concerns about electric tethers moving through the air [170].

Chapter 4: Multi-Criteria Decision Analysis

The Multi-Criteria Decision Analysis (MCDA) is a multi-step procedure consisting of a set of methods to structure and formalise decision-making processes in a transparent and consistent manner, although it always requires some sense of subjectivity [171]. The decision maker needs to identify a set of objectives and establish measurable criteria to assess the extent to which the objectives have been achieved by each choosable alternative [172]. MCDA is a vastly used tool in engineering, as well in other fields, and there are several methods developed [173, 174]. The selection of a method is based on the type of decision to make, on the time available to undertake the analysis and on the amount or nature of data available to support the analysis [172]. In the present case, the decision is based on many interdependent criteria and deals with considerable uncertainty due to the data of qualitative nature used, hence the most suitable method was considered to be the Fuzzy Analytic Network Process (FANP).

4.1 Fuzzy Analytic Network Process

The FANP is a method to support decision making in complex and uncertain environments [175]. It is an improvement of the conventional Analytic Network Process (ANP), as it uses *Fuzzy Set Theory* to deal with its inherent uncertainty and subjectivity. Firstly, one introduces the relevant characteristics of the ANP method.

4.1.1 Analytic Network Process

The ANP method is a structured technique widely used to solve real-world problems, since it takes into account complex relationships between decision elements and because it allows quantitative and qualitative attributes to be applied [176]. To model the decision problem, a network with several levels must be constructed. Its levels usually include the goal level, the criteria level and the alternatives level. The criteria may be grouped in clusters. The network represents the several dependencies and influences between its elements, namely the interdependence of criteria in the same or in different clusters and the influence of the available alternatives on the importance of the criteria [177]. This aspect often leads to the prioritization of certain criteria that initially, with merely intuition, seemed not as important, but in fact are very relevant in the decision process [178].

In order to assess these feedback relationships, pairwise comparisons must be performed. This is achieved by computing a matrix whose elements measure the relative importance of one criteria (matrix row - *i*) with respect to the other (matrix column - *j*) according to a certain scale. Every computed matrix is reciprocal, i.e. the importance of element *j* with respect to *i* is expressed by the inverse value of the importance of element *i* with respect to *j*.

The judgements are performed as ”educated guesses” and in order to be the least uncertain, a significant amount of information has to be collected, as in chapter 2. However, characterizing a relationship

between two elements with a crisp value will always lead to a certain degree of subjectivity, vagueness, and imprecision [175]. Hence, to cope with this limitation, the judgments are performed by using fuzzy numbers. Then, for each comparison matrix, a set of weightings is obtained.

The FANP method only differs from the conventional ANP in the way pairwise comparisons are made and their respective weightings are obtained. Therefore, one describes next, step by step, the conventional methodology utilized, leaving what is specific of the *Fuzzy Set Theory* for section 4.1.2:

1. **Compute the Network**

   Firstly, one must identify the goal of the decision, the clusters and respective criteria on which the evaluation will be based and the alternatives on which the decision will act upon. Then, the inter-dependencies between criteria both in the same cluster (inner dependence) and in other clusters (outer dependence) are identified.

2. **Compute the Unweighted Supermatrix**

   One applies the aforementioned pairwise comparisons with respect to each and every network node, by cluster, taking into account the corresponding dependencies. The resulting set of weightings is then inserted in the respective columns and rows of a supermatrix. This matrix is square and each column represents a network node, i.e. the supermatrix has a number of rows and columns equal to the number of criteria plus alternatives plus the goal.

   Some supermatrix elements are already automatically assigned to zero since it is clear there is no influence of one element with respect to the other. That is the case of the supermatrix main diagonal, since a node does not influence itself. Also, one alternative does not influence the other, thus the elements relative to these relationships take the zero value.

3. **Compute the Normalized Weighted Supermatrix**

   In this step, the importance of the clusters themselves is addressed. Each group of nodes - the goal group (single element), the criteria clusters, and the alternatives group - are matter of comparison.

   Having a total of $n_{clusters}$ groups of nodes, one obtains $n_{clusters}$ vectors, each one with $n_{clusters}$ weightings. Each weighting, then, multiplies the respective set of nodes in the unweighted supermatrix. Note that, if a cluster does not influence another, then the respective weighting is zero.

   In order to get meaningful weights, one divides each element of the supermatrix by the sum of all elements in its respective column, obtaining the normalized weighted supermatrix.

4. **Compute the Limit Supermatrix**

   Finally, in order to obtain the preferences of the alternatives and also the priorities in criteria, one must compute the limit supermatrix. Accordingly, the normalized weighted supermatrix will be iteratively raised to larger powers until it converges into one matrix with all its columns equal (limit matrix) or into a cycle of matrices. In the latter, the limit matrix is obtained by averaging those matrices [179]. Computationally, one accelerates convergence by limiting the number of decimals to be equal between columns.

The decision can now be taken by analysing one of the columns of the matrix. Its elements can be normalized either by group or globally, in order to easily identify the criteria preference by cluster or in general. By doing the same to the values relative to the alternatives, one gets the best choice according to the ANP method (correspondent to the biggest value), as well as to the FANP method.

This method is one of the most adequate methods for problems with dependencies between criteria. However, it has some limitations/disadvantages that should be mentioned [180]. Firstly, a large number of pairwise comparisons must be done, which is very time-consuming and makes it more difficult to keep the several judgements proportional and consistent in between. User's misunderstanding of the pairwise comparisons between criteria and/or clusters may also lead to wrong inputs. The most problematic are the ones assessing the influence of a cluster on itself (step 3). Finally, as mentioned, the uncertainty associated to the initial judgments is the most critical downside of the conventional ANP, thus one presents next how *Fuzzy Set Theory* can be applied to minimize this aspect.

4.1.2 Fuzzy Judgments and their Consistency

Fuzzy Set theoretic approaches have been extensively suggested in the literature to address the uncertainty problem. Instead of using a crisp value to represent a judgment, one uses a triangular fuzzy set, which is defined by three real numbers: $l^z \leq m^z \leq u^z$, where m^z is the most probable value for the judgment, and l^z and u^z are the lower and upper bounds. It is also characterized by a membership function $\mu_M(x)$ with the following specifics [181]: 1) $\mu_M(x)$: $\mathbb{R}^+ \rightarrow [0,1]$, continuously; 2) $\mu_M(x) = 0$ for all $x \in]-\infty, l^z]$ and $x \in [u^z, +\infty[$; 3) $\mu_M(x) = 1$ for $x = m^z$; 4) it is strictly linearly increasing on $[l^z, m^z]$ and strictly linearly decreasing on $[m^z, u^z]$.

To perform the fuzzy judgments, one requires a scale that translates a qualitative relation into a quantitative one. The typically utilized scales are adaptations from the one suggested by Saaty for the conventional ANP [177]. Across this decision problem, one uses the two scales, which are presented in tables 4.1 and 4.2. They introduce the concept of fuzzy triangular numbers to deal with uncertainty.

Table 4.1: Triangular Fuzzy Scale, with $m^z = \{1, 2, ..., 8, 9\}$.

Qualitative Importance	**Fuzzy Scale**	**Reciprocal Fuzzy Scale**
Equal	$(1,1,1)$	$(1,1,1)$
Intermediate	$(1,2,3)$	$(\frac{1}{3}, \frac{1}{2}, 1)$
Moderate	$(2,3,4)$	$(\frac{1}{4}, \frac{1}{3}, \frac{1}{2})$
Intermediate	$(3,4,5)$	$(\frac{1}{5}, \frac{1}{4}, \frac{1}{3})$
Strong	$(4,5,6)$	$(\frac{1}{6}, \frac{1}{5}, \frac{1}{4})$
Intermediate	$(5,6,7)$	$(\frac{1}{7}, \frac{1}{6}, \frac{1}{5})$
Very Strong	$(6,7,8)$	$(\frac{1}{8}, \frac{1}{7}, \frac{1}{6})$
Intermediate	$(7,8,9)$	$(\frac{1}{9}, \frac{1}{8}, \frac{1}{7})$
Extreme	$(8.5,9,9)$	$(\frac{1}{9}, \frac{1}{9}, \frac{1}{8.5})$

Table 4.2: Finer Triangular Fuzzy Scale, with $m^z = \{1, 1.5, 2, ..., 8, 8.5, 9\}$.

Fuzzy Scale		**Reciprocal Fuzzy Scale**	
$(1,1,1)$		$(1,1,1)$	
$(1,1.5,2.5)$	$(1,2,3)$	$(\frac{2}{5}, \frac{2}{3}, 1)$	$(\frac{1}{3}, \frac{1}{2}, 1)$
$(1.5,2.5,3.5)$	$(2,3,4)$	$(\frac{1}{3.5}, \frac{2}{5}, \frac{2}{3})$	$(\frac{1}{4}, \frac{1}{3}, \frac{1}{2})$
$(2.5,3.5,4.5)$	$(3,4,5)$	$(\frac{1}{4.5}, \frac{1}{3.5}, \frac{2}{5})$	$(\frac{1}{5}, \frac{1}{4}, \frac{1}{3})$
$(3.5,4.5,5.5)$	$(4,5,6)$	$(\frac{1}{5.5}, \frac{1}{4.5}, \frac{1}{3.5})$	$(\frac{1}{6}, \frac{1}{5}, \frac{1}{4})$
$(4.5,5.5,6.5)$	$(5,6,7)$	$(\frac{1}{6.5}, \frac{1}{5.5}, \frac{1}{4.5})$	$(\frac{1}{7}, \frac{1}{6}, \frac{1}{5})$
$(5.5,6.5,7.5)$	$(6,7,8)$	$(\frac{1}{7.5}, \frac{1}{6.5}, \frac{1}{5.5})$	$(\frac{1}{8}, \frac{1}{7}, \frac{1}{6})$
$(6.5,7.5,8.5)$	$(7,8,9)$	$(\frac{1}{8.5}, \frac{1}{7.5}, \frac{1}{6.5})$	$(\frac{1}{9}, \frac{1}{8}, \frac{1}{7})$
$(7.5,8.5,9)$	$(8.5,9,9)$	$(\frac{1}{9}, \frac{1}{8.5}, \frac{1}{7.5})$	$(\frac{1}{9}, \frac{1}{9}, \frac{1}{8.5})$

The scales measure relative importance from $m^z = 1$ to $m^z = 9$, with 1 meaning that the elements being compared are equally important, and 9 meaning that the element of row i is extremely more important than the element of column j. Apart from the extremes, all fuzzy numbers are symmetric, i.e. $m^z - l^z = u^z - m^z$, being the difference between bounds equal to 2. The scale of table 4.2 is finer, as it also uses the '.5' decimal, and it is applied when the number of elements to be compared in one single matrix is high, requiring a larger degree of distinction between judgments.

According to the problem's network and using the aforementioned scales, the decision maker builds several fuzzy comparison matrices, from which one must derive crisp weightings vectors that can be used to compute the ANP's unweighted supermatrix. Considering a single comparison matrix $\tilde{A}$ of dimensions $n \times n$ and elements $\tilde{a}_{ij} = (l_{ij}^z, m_{ij}^z, u_{ij}^z)\,|_{i,j=1,2,...,n}$, one must obtain a weightings vector $w = \{w_1, w_2, ..., w_n\}$ that satisfies the following double-sided inequality: $l_{ij}^z \tilde{\leq} {}^{w_i}/_{w_j} \tilde{\leq} u_{ij}^z$. Hence, the resulting weightings ratios must approximately satisfy the initial fuzzy judgment. These inequalities may be represented using a membership function similar to the one described earlier, whose object is now the weightings ratio [182]:

$$\mu_M\left({}^{w_i}/_{w_j}\right) = \begin{cases} \frac{{}^{w_i}/_{w_j} - l_{ij}}{m_{ij} - l_{ij}} & , \quad {}^{w_i}/_{w_j} \leq m_{ij} \\ \frac{u_{ij} - {}^{w_i}/_{w_j}}{u_{ij} - m_{ij}} & , \quad {}^{w_i}/_{w_j} \geq m_{ij} \end{cases} \qquad i, j = 1, 2, ..., n \tag{4.1}$$

Since a comparison matrix is reciprocal, one only requires its upper triangular part to derive the weightings, i.e. only $\frac{n(n-1)}{2}$ membership functions must be computed. By intersecting them on the $(n-1)$-*dimensional simplex* $Q^{n-1} = \{(w_1, ..., w_n) | w_i > 0,\, w_1 + ... + w_n = 1\}$, one gets a fuzzy feasible area from which a crisp weightings vector can be obtained. This area may be described by an aggregated membership function, hence each set of possible weightings has a certain degree of membership (also from zero to unity). The solution that is chosen to be the comparison matrix's weightings vector is the one with the highest degree of membership.

This degree of membership can be seen as a *consistency index* (CI) of the pairwise comparison matrix. If $CI \leq 0$, it means there is no feasible area resulting from the intersection of all membership functions. On the contrary, if $CI > 0$, then the judgments performed are consistent, being the consistency as higher as CI is closer to unity (perfect consistency). Note that a 2×2 matrix is always perfectly consistent.

As the area of possible solutions for the weightings vector results from the intersection of all membership functions, then $CI \leq \mu_M({}^{w_i}/_{w_j})$. By applying the specific form of the functions as in eq. (4.1) and resorting only to the upper triangular matrix elements, one obtains two inequalities that serve as constraints to find the weightings vector [182]:

$$\begin{cases} (m_{ij}^z - l_{ij}^z)\, CI\, w_j - w_i + l_{ij}^z\, w_j \leq 0 \\ (u_{ij}^z - m_{ij}^z)\, CI\, w_j + w_i - u_{ij}^z\, w_j \leq 0 \end{cases} \qquad i = 1, ..., n-1; \quad j = 2, ..., n; \quad j > i \tag{4.2}$$

Under these specifications, deriving a set of crisp weightings for each matrix consists of solving an optimization problem. Hence, computational implementation is required, which is described next.

4.1.2.1 Obtain the Weightings Vector

One intends to get, for each comparison matrix, a weightings vector w and a *consistency index* CI. The latter must be maximized and that is the goal of the aforementioned optimization approach. Part of the problem constraints are given by the inequalities in eq. (4.2), which are non-linear with respect to the variables to be calculated (w_k and CI). The remaining constraint is trivial, as follows:

$$\sum_{k=1}^{n} w_k = 1 \qquad , \quad w_k > 0 \tag{4.3}$$

To solve this non-linear constrained problem, one employs the function *fmincon* of Matlab's optimization toolbox, as proposed in [183]. This function uses Sequential Quadratic Programming (SQP), which requires the problem's objective function to be twice continuously differentiable. At each iteration, the algorithm approximates the constraints linearly while a quadratic approximation to the problem's Lagrangian function is employed as an objective function [184]. This is a very efficient method for any type of non-linearities in the problem's constraints or in its objective function.

The function *fmincon* finds the minimum of a problem specified by a set of conditions, as given by:

$$\{c(x) \leq 0 \quad ; \quad ceq(x) = 0 \quad ; \quad A \cdot x \leq b \quad ; \quad Aeq \cdot x = beq \quad ; \quad VLB \leq x \leq VUB\} \tag{4.4}$$

It is implemented as follows:

$$x = fmincon\,(\,f,\, x_0,\, A,\, b,\, Aeq,\, beq,\, VLB,\, VUB,\, nlconst) \tag{4.5}$$

where x is a vector of dimension $(n+1)$ containing the outcome of the optimization problem. The set $\{x_1, \ldots, x_n\}$ corresponds to the comparison matrix's resulting weightings, while x_{n+1} is the *consistency index* CI. In turn, f is the objective function to be minimized, so, as the goal is to maximize CI, then $f = -x_{n+1}$. Also, x_0 is an initialization of x: for $i = 1, \ldots, n$, $x_{0,i} = \frac{1}{n}$, while $x_{0,n+1} = 1$, which is the maximum value possible. Since this optimization problem has no linear inequalities as constraints, then $A = [\,]$ and $b = [\,]$. On the contrary, there is a linear equality constraint given by eq. (4.3), hence $Aeq_{1,\ldots,n} = 1$, $Aeq_{n+1} = 0$, and $beq = 1$. In addition, VLB represents the lower bounds of x, thus: $VLB_{1,\ldots,n} = 0$ and $VLB_{n+1} = -\infty$; VUB represents the upper bounds, but since these are already imposed by the constraints and in order not to overdefine the problem: $VUB_{1,\ldots,n+1} = [\,]$. Finally, $nlconst$ is a function that gives the non-linear constraints: $[c(x), ceq(x)] = nlconst(x, l, m, u, n)$, where $ceq(x)$ are the inequalities presented in (4.2), and $ceq(x) = [\,]$ since there are no non-linear equations constraining the present decision problem.

After solving the optimization problem for each comparison matrix, one must verify if CI, i.e. x_{n+1}, takes a positive value. If not, then the matrix is inconsistent and the judgments must be revised. However, this process may be challenging since it may be only one judgment or a combination of judgments causing the inconsistency. Therefore, in order to facilitate this post-correction of judgments, one resorts to the concept of *Knowledge-Based Consistency Index*.

4.1.2.2 Knowledge-Based Consistency Index

The calculation of this index (KCI) allows the identification of the judgments that are causing the comparison matrix to be inconsistent. When the matrix is consistent, then the resulting *consistency*

index is very similar to the one *fmincon* function provides as the solution of the optimization problem.

The mathematical details of the KCI derivation can be looked up in [185], thus one only presents the fundamentals which are relevant for the inconsistency detection. Every element of the upper triangular comparison matrix has to be analysed. For that, one uses: the direct knowledge provided by the decision maker when comparing the element i with j, i.e. the respective fuzzy set $\tilde{a}_{ij}$; and the indirect knowledge that derives from the transitivity properties of the matrix, which is represented by a fuzzy multiplication $\tilde{a}_{ik} \otimes \tilde{a}_{kj}$, with $k = \{1, ..., n\} \setminus \{i, j\}$. The multiplication of the fuzzy sets leads to another fuzzy set, and it can be easily implemented using Matlab's function *fuzarith*.

Thereby, for each element of the upper triangular comparison matrix, one plots the membership functions correspondent to the respective direct and indirect knowledge. If that judgment is consistent, then the plots have an intersection area described by the following fuzzy set: $\tilde{c}_{ij} = \tilde{a}_{ij} \cap (\tilde{a}_{ik} \otimes \tilde{a}_{kj})$. Moreover, the consistency index of that particular judgment takes the value of the ordinate of the area's upper point: $sup(\tilde{c}_{ij})$. If it is not consistent, then one must identify which membership functions are not making an intersection possible, and then modify the respective judgments in the comparison matrix. An illustrative example is provided in figure 4.1. On the left, the plots of the relevant membership functions for the initial judgment $\tilde{a}_{12}$ of a 4×4 matrix are showcased. As depicted, there is no intersection area and the cause may be pointed to the curve correspondent to $\tilde{a}_{14} \otimes \tilde{a}_{42}$. Hence, matrix elements $\tilde{a}_{14}$ and $\tilde{a}_{42}$ should be revised. After proper modification, one obtains the plots on the right of figure 4.1, where the intersection area is shaded and the correspondent judgment consistency is identified as '*'.

Finally, to obtain the comparison matrix's KCI and ensure that all judgments are consistent (positive KCI), one must compute: $KCI = min\{sup(\tilde{c}_{ij})\}$, with $i = 1, ..., n-1$ and $j = 2, ..., n$ $(j > i)$. From a consistent matrix, the process described in subsection 4.1.2.1 can be applied, followed by the one in section 4.1.1.

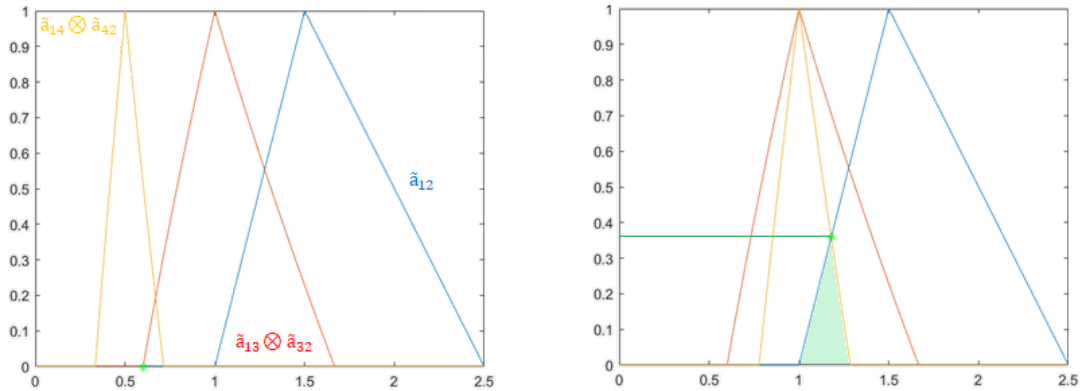

Figure 4.1: Illustrative example of checking for judgment consistency with KCI concept. On the left, the fuzzy sets plots before existing consistency, and on the right, after it exists.

4.2 Choosing an AWE system using the FANP method

By applying the Fuzzy Analytic Network Process, one intends to choose an Airborne Wind Energy system using the factors presented in chapter 3 as criteria. The ultimate goal of this decision process is to pick the most suitable design for a certain exploration site - rural (on-shore) or off-shore. A rural site is characterized by being an open field location close to an inhabited area and where the surrounding

land may be used, for example, for agricultural purposes. An offshore site, as its designation points out, is a high-seas location far from populations but with intense wearing for the systems, and with difficult logistics associated.

Considering this technology's most recent commercial developments in locations such as the Aruba island [19] and the Mauritius islands [20], one initially considered to choose the most adequate system for a remote site as well. After some thought, one concluded that applying the method to general on-shore and off-shore sites was already inclusive enough of the remote scenario, since this exploration site would always be on-shore near some populated area (even if small), or off-shore. Although this site's main characteristic is being an off-grid location with difficult accessibility, at the light of the current methodology and comparing with the other two scenarios, that would not bring any significant changes to the inputs, and subsequently to the results.

For each scenario, the 'best system' will be the one harvesting the largest amount of power at the smallest cost possible, comparing systems with the same power output. It must be mentioned that the systems analysis with respect to the goal is qualitative. Next, the systems on which the decision will act upon are described.

4.2.1 Alternatives for Decision Making

Regarding the design alternatives, one considers only feasible and propitious systems. For example, no vertical axis generator (sec. 2.3.2) nor railway generator (sec. 2.3.3) systems are considered, since they have no advantages over pumping cycle systems. Skypull's system is also discarded since a biplane with vertical take-off is not advantageous in pumping cycles, due to its drag and weight.

One proposes nine alternatives which differ in the electricity generation mode, the wing type, the take-off/landing approaches and the control mechanisms. Since the alternatives are being compared, they are assumed to have the same output power and the same type of generator. They are presented next in table 4.3. For the sake of brevity, the following abbreviations are used: 'OG' - on-ground; 'OB' - on-board; 'SLE' - supported leading edge; 'CT' - conventional tail (1 vertical and 1 horizontal stabilizers); 'TBT' - twin-boom tail (2 vertical and 1 horizontal stabilizers); 'LHT' - linear horizontal take-off; 'LVT-VO' - linear vertical take-off with the aircraft tilted vertically (fig. 2.21-A); 'LVT-HO' - linear vertical take-off with the aircraft in horizontal orientation (fig. 2.21-B); 'BLS' - bridle line system; 'ACU' - airborne control unit.

Table 4.3: Description of the nine choosable alternatives (alt.) in the decision process.

Alt.	Companies with developed prototypes	Electricity Generation	Flying Unit	Take-off / Landing approach	Control Mechanisms
A1	Ampyx Power eWind Sol. [30, 38]	OG Pumping Cycle System with 1 tether	Rigid Mono-plane Wing with CT or TBT	LHT with 1 or 2 OB propellers (sec. 2.7.1.1)	Conventional OB actuators
A2	TwingTec Kitemill [31, 32]	same as A1	same as A1	LVT-HO with 3 or 4 OB propellers	same as A1

A3	EnerKite [36]	same as A1	Swept Rigid Wing	Rotational with no extra OB power (sec 2.7.1.3)	BLS with OG steering mechanisms
A4	SkySails Power [33]	same as A1	RAM-Air Wing (sec. 2.5.1.2)	Passive approach with elevating mast (sec. 2.7.2)	BLS with ACU
A5	Kitenergy [37]	OG Pumping Cycle System with 2 tethers, and 2 generators	same as A4	same as A4	BLS with OG steering mechanisms via the 2 tethers
A6	KitePower KiteGen [34, 39]	same as A4	SLE kite (sec. 2.5.1.1)	Semi-Passive approach with elevating mast and OG fans (sec. 2.7.2)	same as A4
A7	KiteGen [34]	same as A4	Semi-rigid wing in C-shape [115]	same as A4	BLS with OG steering mechanisms
A8	Makani Power Windlift [27, 29]	OB with 8 generators	Rigid Monoplane wing with CT	LVT-VO with 8 propellers	Conventional OB actuators
A9	KiteKraft [28]	same as A8	Rigid Biplane wing with TBT	same as A8	same as A8

4.2.1.1 Classification of Alternatives on each Criterion

In step 2 of the FANP method, one must compare the previous alternatives with respect to each criterion of chapter 3. Accordingly, one presents a ranking of the alternatives based on their performance in each criterion. This will be used further to compute the respective comparison matrices. It follows:

- **Aerodynamic Performance:** A1, A9; A2, A8; A3; A7; A4, A5; A6.

  In their respective modes of electricity generation, A1 and A9 have the best AP, followed by A2 which produces more drag due to the higher number of propellers, and by A8 which produces less lift. Then comes A3 since it is a rigid wing system as well, followed by A7 which is semi-rigid. Finally, for soft wing systems, AP is better in A4 and A5 (RAM-Air wing systems), specially in A4 since it only has one tether. Lastly, it comes A6.

- **Mass-to-Area Ratio:** A6; A4, A5; A7; A3; A1; A2; A8, A9.

  The best MA (smaller value) is achieved by soft wing systems, especially LEI kites. Hence, A6 is the best alternative, followed by A4 which has an airborne control unit, and A5 which has two tethers. Being semi-rigid, A7 is next, followed by A3 which has no on-board propellers. Finally, based on the number of propellers/generators, it comes A1, A2, and then A8 and A9.

- **Durability:** A8, A9; A3; A1; A2; A7; A5; A4; A6.

  This factor is best achieved by A8 and A9 since the wings are of rigid type and the tether has a fixed length while operating, thus minimizing fatigue. Then, for the remaining rigid wing systems, it comes A3, followed by A1 and A2 (includes the maintenance of the propellers), and then A7. For soft wing systems, DU is better in A5 - it has two tethers, thus they are subjected to lower loads. Finally, one has A4 and lastly A6 (inflatable leading edge requires special care).

- **Survivability:** A5; A4, A6; A1, A2; A8, A9; A7; A3.

  The alternatives with soft wings and mechanisms to prevent destructive crashes have higher SU. Hence, in this criterion, A5 is the best system, followed by A4 and then A6. Regarding, rigid wing systems, gliders with less number of propellers are better - A1 and A2, followed by A8 and A9. At last, it comes A7 and A3.

- **Continuity of Power Production:** A8, A9; A1, A2; A3; A7; A6; A4, A5.

  The best alternatives operate in *Drag-mode* - A8 and A9. Then, the faster the retraction phase the better, hence the best alternatives, by preference, are A1 and A2, A3, A7, A6, and lastly A4 and A5.

- **Controlability:** A8, A9; A1, A2; A4, A6; A7; A5; A3.

  To evaluate alternatives in CTR, one must assess not only flight but also operation Controlability. Hence, the best alternatives are the ones composed of rigid wings with on-board actuators that operate in *Drag-mode*, i.e. A8 and A9. Due to the characteristics mentioned first, the following best are A1 and A2. In soft wing systems, CTR is better if they employ airborne control units, hence A4 and A6 are the next best alternatives, followed by A7. Finally, it comes A5 and A3, which are the hardest to control.

- **Take-Off / Landing Feasibility:** A2; A1; A4, A5; A7; A6; A8, A9; A3.

  The smallest complexity is achieved by A2, followed by A1, as explained in subsection 3.2.3. Next, passive approaches for soft wings are as more feasible as the lower the airborne weight and the lower the number of extra components. Hence, by preference, the next best alternatives are A5, A4, A7 and A6. Finally, it comes the vertical approach from on-board generation systems (A8 and A9), and A3's rotational approach.

- **Manufacturability:** A4, A5; A6; A3; A1; A2; A7; A8; A9.

  As mentioned in subsection 3.3, the best alternatives are the ones with soft wings, specially RAM-Air wings since LEI wings have scalability problems. Accordingly, the leading alternatives in this criterion are A4 and A5, followed by A6. Among rigid wing systems, the lower the number of propellers to mount on the structure the better, hence they are ordered as A3, A1, A2, A7 (semi-rigidity is complex), A8 and A9 (since it is a biplane, its fabrication is harder).

- **Logistics:** A2; A1; A4, A5, A7; A8, A9; A6; A3.

  The classification of alternatives in this criterion follows the same tendency as in TLF because of installation logistics, although with less distinction between them. Therefore, they are ordered as A2 and A1, followed by A4, A5. Next, it comes A7 (as it has a bigger weight, it requires installing a higher

mast) and A6 (it requires the installation of on-ground fans). A8 and A9, and lastly A3 are the worse alternatives in this criterion.

- **Visual Impact:** A3; A8, A9; A1, A2; A4, A5, A6, A7.

  As mentioned in subsection 3.5.1, VI is as lower as the airborne system is smaller and its flight path is aesthetic. Hence, A3 is the best alternative, followed right away by A8 and A9, and then A1 and A2. The remaining alternatives are considered to have the same visual impact.

- **Noise Impact:** A4, A5, A7; A3, A6; A1, A2; A8, A9.

  Pumping-cycle systems with no airborne propellers have the lowest NI. Hence, A4, A5 and A7 are the best alternatives in this criterion, followed by A3 and A6 which produce more noise in take-off due to the rotational arm and on-ground fans, respectively. Next, it comes A1 and A2, and finally, due to the on-board generators, A8 and A9.

- **Ecological Impact:** A4, A6; A5; A7; A8, A9; A1, A2; A3;

  In general, the larger the airborne units the lower EI. Also, in case of a collision with flying species, the softer the wing the better in this criterion. Hence, A4 and A6 are considered to be the best, followed by A5 (the two tethers may cause more collisions with flying species), and then A7. In case of rigid wing systems, the louder they are the better in preventing collisions, so it follows that the best alternatives are A8 and A9, and then A1, A2 and A3.

- **Safety:** A5; A4, A6; A7; A1, A2; A3; A8, A9.

  There is no alternative that is the absolute best in this criterion, however one may assume soft wing systems to be safer than rigid wing systems, and, between these, on-ground generation safer than on-board generation. Hence, one considers A5 to be the best alternative (double connection to the ground), followed by A4 and A6. Then, A1 and A2 (due to its better Controlability), followed by A3 and A7, and finally A8 and A9.

4.2.1.2 Evaluation of Alternatives on each Criteria Cluster

In step 2 of the FANP method, one also has to evaluate each alternative on each criteria cluster. Exceptions are made to the Manufacturability and Logistics clusters, which are made of one single criterion and therefore no comparison is needed. One presents an explanation for the fuzzy judgments performed, as follows:

- **Technical Design Factors:** the alternatives with rigid wings (A1, A2, A3, A8 and A9) have their advantages in aerodynamic performance and durability, with preference to AP. The importance of these criteria with respect to the mass-to-area ratio is more substantial in alternatives where MA is more disadvantageous (A8 and A9 due to the numerous on-board propellers), and less substantial when the weight is reduced (A3). Between A8 and A9, AP is even more substantial for the latter since it is a biplane. For the aforementioned alternatives, survivability is the most unfavourable factor, except for A8 and A9 where it has a slight advantage over MA. It is for A3 that the SU factor has the smallest relative importance, since the swept rigid wing is less controllable, hence more probable to have a destructive crash.

The alternatives with soft wings (A4, A5 and A6) have their strength in mass-to-area ratio. The relative importance of this factor is more substantial for systems with LEI wings (A6). Regarding aerodynamic performance, its importance is more substantial for systems with RAM-Air wings (A4 and A5) and less dense bridle systems. Hence, the importance of MA over AP is larger for A6, than for A4 and A5. Since these systems' wings are made of fabric, durability is the less favourable criterion, specially for LEI wings. Regarding survivability, AP is moderately more important.

Alternative 7 is evaluated in between these two groups: MA and AP are closer in importance; DU has a similar role to the one in rigid wing systems; and SU has the approximately the same relevancy as in soft wing systems.

- **Operational Factors:** the alternatives with on-board electricity generation (A8 and A9) have their strength in producing power continuously, whereas their weakness is in take-off / landing complexity, since a vertical maneuver with the aircraft tilted vertically requires an elevated platform as well as imposes difficulties of control at high wind speeds, as mentioned in subsection 2.7.1.2. On the contrary, the alternatives 1 to 7 have their weakness in CPP, that being more substantial for soft wings (longer retraction phases), and even more for RAM-Air wings (worse depower capabilities).

  Alternatives with rigid wings have advantages in CTR, with similar relative importance. Regarding TLF, as seen in subsection 3.2.3, it is A2's major strength, but also constitutes a good advantage of A1. Hence, the relative importance between CTR and TLF in these systems is close to be equal.

  For soft wing systems, CTR has a more relevant role with respect to CPP if its control is obtained via an airborne unit. With respect to TLF, it is slightly less important for A4 and A5, since both systems use a simple passive approach. However, for A6, CTR is moderately more important than TLF, due to its need for on-ground fans.

- **Social Acceptability Factors:** the alternatives with on-board electricity generation are clearly disadvantageous in the NI criterion, due to the continuous operation of their on-board generators, whereas their strength is in the visual impact criterion as every other rigid wing system, except for A3. In fact, since it has no propellers, this alternative has its strength in NI, which is slightly more important than VI (due to the rotating arm, its ground station has a greater visual impact than those of other systems). Regarding EI and SF criteria, in none of the previous alternatives there is a clear advantage of one over the other, except once again from A3 where EI is slightly more important than SF, given that it has a really slim wing, but in case of a failure it may experience a very uncontrolled crash.

  In contrast, alternatives with soft wings have their best quality in producing little noise, while their weakness is having a large VI. The difference in relative importance is as more substantial as larger the elevating towers/masts are. After NI, EI is the second best quality of these systems, being moderately more important than SF (though slightly less important in A5 because it has a double connection to the ground). All these trends are applicable for A7, but in this case the importance of the other criteria over SF is more substantial, due to this wing's increased rigidity.

4.2.2 FANP implementation

The question to be answered at this stage reads: What is the most appropriate design for a certain exploration site - on-shore rural and off-shore? For that purpose, the methodology introduced in section 4.1 is now applied.

1. **Compute the Network**

   This decision problem is represented by 7 clusters, with their respective nodes: the goal cluster (GOAL), the alternatives cluster (ALT), and the remaining correspond to the five criteria classes presented in chapter 3. All clusters are interdependent, exception made to the goal and alternatives clusters which do not bear a direct relationship in between.

   The node dependencies are expressed in table 4.4, together with a few examples to justify the relation (all abbreviations were introduced in chapter 3).

Table 4.4: Dependencies (Dep.) between network nodes. For each node, these are divided by cluster.

Node	Dep.	Explanation Examples
GOAL	All criteria	-
AP	MA	the wing's $\mathcal{AR}$ influences lift and drag forces
	DU	a weathered wing has a poorer aerodynamic performance
	CTR	control wing's angle of attack on optimal values to get the desired AP
MA	AP	the stronger the aerodynamic forces, the larger the required structural mass
DU	GOAL	the durability of the system depends on the site conditions (e.g. humidity)
SU	GOAL	the survivability of the system in an off-shore site is less probable
	MA	the larger/heavier the system, the more chances of destruction in a crash
	CTR	the better the Controlability, the easier to prevent a catastrophic crash
CPP	AP	it affects the duration of the re-traction phase in pumping-cycle systems
	CTR	same as above
CTR	AP	better aerodynamic performance allows better Controlability
	MA	the wing span length influences the required actuator forces
TLF	AP	better AP allows smaller cut-in wind speeds, reducing take-off complexity
	MA	lower MA allows smaller cut-in wind speeds, reducing take-off complexity
	CTR	it influences the need for extra systems, as the previous two nodes do
M	AP	C_L/C_D depends on the wing's rigidity which influences the fabrication processes
	MA	M depends on structural resistance requirements (structural mass and geometry)
	DU	the materials used depend on the required durability of the airborne system

L	GOAL	the site influences the logistics in transporting and, mainly, installing a system
	MA	it influences the logistics in storing and transporting a system
	TLF	it influences the logistics in installing a system
VI	GOAL	the proximity to an inhabited area influences the relevance of visual impact
	MA	the system's size is the most relevant characteristic to assess its visual impact
NI	GOAL	the proximity to an inhabited area influences the relevance of noise impact
EI	GOAL	the existence and type of affected wildlife depends on the exploration site
	MA	the system's size is relevant for birds to detect it and avoid a collision
	SU	a catastrophic crash may have a significant negative impact on an ecosystem
SF	GOAL	the proximity to an inhabited area influences the relevance of the system's safety
	MA	size and weight are linked to the impact the system may cause on property
	CTR	higher controlabiliy reduces the chances of a catastrophic crash, increasing SF
ALT	All criteria	* All criteria depend on the alternatives, as well

Note that, for the GOAL node, the relative importance of the criteria, per cluster, is site dependent. Hence, in the next step, two supermatrices are computed, one for each exploration site.

2. **Compute the Unweighted Supermatrix**

   Each supermatrix is 23×23, being the first column/row correspondent to the GOAL node; the second to fifth to AP, MA, DU and SU nodes; the sixth to eight to CPP, CTR and TLF nodes; the ninth and tenth to M and L nodes; the eleventh to fourteenth to VI, NI, EI and SF nodes; and the remaining to the alternative nodes by order. The two supermatrices corresponding to the two exploration sites only differ in the first column.

   In this step, according to the dependencies in table 4.4, 51 pairwise comparison matrices have to be computed in total for both scenarios. Using the method described in subsection 4.1.2.2, all the resulting comparison matrices were made consistent ($CI > 0$). For the sake of simplicity, one presents next abridged explanations of the fuzzy judgments only, since the core support are chapters 2 and 3. Furthermore, all the comparison matrices (with resultant weightings and CI) are available in [186], although some examples are provided in appendix A.1. In the matrices, only the most probable value m^z is presented, but with the scales of tables 4.1 and 4.2, the fuzzy sets can be obtained.

   - **Compare criteria with respect to the GOAL node** - 6 matrices (3 for each exploration site):

     In these comparison matrices (see SMA.1 in [186] or the example provided in table A.1 in appendix A.1), the scale of table 4.1 was used. The resulting weightings are inserted in the unweighted supermatrix's first column.

     In the TDF cluster, AP and MA are considered to be of almost equal importance with a slight advantage of the former - see, for example, eq. (2.9). Moreover, they are considered moderately

more important than DU, slightly more in a rural exploration site. With respect to SU, these factors are extremely more important in a rural exploration site, but only strongly more important in an off-shore site, since it is harder to recover the system in this scenario. Between DU and SU, the former is considered moderately more important in both scenarios.

In the OF cluster, CTR is considered strongly more important than CPP and moderately more important than TLF (slightly more for a rural scenario), as it is the factor that allows an optimal operation. Then, TLF is taken as moderately to strongly more important than CPP in a rural exploration site and strongly more important in an off-shore site, since the take-off and landing maneuvers in high-seas are more complex.

In the SAF cluster, the differences between scenarios are more tangible. In a rural site, SF is slightly more important than NI, and both are strongly more important than VI, while moderately more important than EI. Then, EI is moderately more important than VI. This factor is the least relevant for the GOAL due to its subjectivity. In an off-shore site, EI is slightly more important than SF, and both are moderately more important than VI, and strongly more important than NI. Since in this scenario the system is more visible than audible, VI is slightly more important than NI.

The first column elements relative to the dependencies on M and L take the value of unity.

- **Compare the dependencies, per cluster, of each criterion node** - 5 matrices

  In these comparison matrices (see SMA.2 in [186] or the example provided in table A.2 in appendix A.1), the scale of table 4.1 was used.

  From table 4.4, four 2×2 matrices are computed: with respect to AP, MA is strongly more important than DU, not only because of the $\mathcal{AR}$, but also because the airborne weight influences the required lift force; with respect to CTR, AP is moderately more important than MA; with respect to TLF, both AP and MA are considered to be equally important; and, with respect to EI, MA is considered strongly more important than SU. Concerning M, a 3×3 matrix is computed, where AP and MA are almost equally important (both are the major factors influencing the materials and fabrication processes involved), and strongly more important than DU.

  The remaining criteria dependencies correspond to values of unity in the respective rows and columns of the unweighted supermatrix. The non-dependencies take the zero value.

- **Compare alternatives with respect to each criterion** - 13 matrices

  These comparison matrices (see SMA.3 in [186] or the example provided in table A.3 in appendix A.1) are the outcome of what was discussed in subsection 4.2.1.1. The scale of table 4.2 was used to perform the judgments. For each criterion, a vector of nine weightings is obtained and inserted in the rows 15 to 23 of the unweighted supermatrix.

- **Compare criteria, per cluster, with respect to each alternative** - 27 matrices

  Using the scale of table 4.1 and what was expounded in subsection 4.2.1.2, these 27 comparison matrices are obtained (see SMA.4 in [186] or the example provided in table A.4 in appendix A.1). The resulting weightings fill in the unweighted supermatrix's columns relative to the alternatives, from row 2 to 14. Note that, the rows correspondent to the Manufacturability and Logistic nodes

are filled with unity, due to the fact that these are clusters of one element.

The resulting unweighted supermatrices for both the on-shore rural and off-shore exploration sites are presented in appendix A.2.

3. **Compute the Normalized Weighted Supermatrix**

   In this step, having the seven network clusters, one has to compute seven comparison matrices for each exploration site, which are available in SMA.5 in [186] (an example is provided in table A.1 of appendix A.1). For the fuzzy sets, the scale of table 4.1 was employed. Also according to the dependencies described in table 4.4: the GOAL and ALT clusters depend on the criteria clusters; the TDF, L, and SAF clusters depend on the GOAL, TDF, OF, and ALT clusters; the OF cluster depends on the TDF, OF and ALT clusters; and, finally, the M cluster depends on the TDF and ALT clusters. The correspondent fuzzy judgments may be justified as follows:

   - **Compare clusters importance for the GOAL cluster:** The TDF and OF clusters are always the most important clusters, as they encompass the most influential criteria for power production, being TDF slightly more important than OF. Then, in a rural exploration site, due to the proximity to inhabited areas, the SAF cluster is the third most important (slightly less important than OF and moderately less important than TDF), followed by M. Finally, the least important for the GOAL is the L cluster. In an off-shore exploration site, as the environmental conditions are harsher, M is the third most important cluster. Accessibility and installation are also more complex, thus the L cluster comes next, being moderately less important than M and slightly more important than the SAF cluster (only the EI factor is more significant is this scenario). The five resulting weightings multiply the five non-null blocks of the unweighted supermatrix's first column (see appendix A.2).
   - **Compare clusters importance for the TDF cluster:** The most important cluster for the technical design factors, in both scenarios, is itself, mainly due to the great dependency of AP on MA and vice-versa. In a rural exploration site, this cluster is very strongly more important than the GOAL and ALT clusters and moderately more important than OF. Then, OF is moderately more important than GOAL and ALT clusters, which are considered to have the same relevancy. Contrarily, the importance for TDF of the GOAL cluster in an off-shore scenario increases, specially due to its impact on DU and SU. Hence, TDF is now only moderately more important than the GOAL (and OF) cluster, and this is slightly more important than OF. The ALT cluster remains as the least relevant for TDF, since are the technical design factors that mainly define the alternatives' importance and not the other way around. The four resulting weightings multiply the second column of non-null blocks of the unweighted supermatrix.
   - **Compare clusters importance for the OF cluster:** Since none of the operation nodes depend on the GOAL, neither on logistics, this comparison matrix is equal for both exploration sites. TDF is considered to be the most important cluster for OF (moderately more than OF and much more than ALT), mainly due to the dependence of all three factors on AP. Then, OF is considered moderately more important than the ALT cluster. The resulting three weightings multiply the third column of non-null blocks of the unweighted supermatrix.

- **Compare clusters importance for the M cluster:** Once again this 2×2 comparison matrix is the same for both scenarios. The TDF cluster is considered strongly more important than the ALT cluster, since its factors are the main definers of the materials and fabrication processes involved. From this comparison matrix, it results two weightings that multiply the fourth column of non-null blocks of the unweighted supermatrix.
- **Compare clusters importance for the L cluster:** The logistics factor/cluster is mainly dependent on the alternatives. Hence, for both scenarios, the ALT cluster is strongly more important than TDF and moderately more important than OF. Moreover, due to installation logistics, it is as important as the GOAL cluster in an off-shore scenario, whereas it is strongly more important in a rural scenario. For the same reasons, the OF cluster is only slightly more important than TDF in a rural scenario, and moderately to strongly more important in an off-shore scenario. The four resulting weightings multiply the fifth column of non-null blocks of the unweighted supermatrix.
- **Compare clusters importance for the SAF cluster:** The social acceptability factors are intrinsically linked to the overall alternatives characteristics. Hence, the ALT cluster has the most relevancy for the SAF cluster. It is considered moderately more important than TDF and strongly more important than OF in both exploration sites, being TDF also moderately more important than OF. In a rural scenario, the GOAL cluster, i.e. the proximity to an inhabited area, has a larger relevancy for the SAF cluster than in an off-shore scenario. Hence, in the first case, the ALT cluster is only slightly more important than the GOAL cluster, while in the second case it is strongly more important. Like so, in a rural scenario the GOAL cluster is moderately more important than TDF and strongly more important than OF, whereas in an off-shore it is only slightly more important than OF and even moderately less important than TDF. From this comparison matrix, one obtains four weightings that multiply the sixth column of non-null blocks of the unweighted supermatrix.
- **Compare clusters importance for the ALT cluster:** For both scenarios, TDF is the most relevant cluster, followed by OF and then M, since its factors are the main definers of the airborne subsystems. The difference between scenarios is in the relative importance of L and SAF clusters to define the alternatives. In a rural exploration site, the SAF cluster is more important than the L cluster, while in an off-shore site the contrary is true. Even so, both factors are the least relevant for the ALT cluster. The resulting five weightings multiply the last column of non-null blocks of the unweighted supermatrix.

After normalizing the supermatrix's columns, one obtains a normalized weighted supermatrix for each exploration site. These are presented in appendix A.3.

4. **Compute Limit Supermatrix**

   The previously obtained normalized supermatrices are raised to increasing powers until all their columns are equal (or approximately equal). It was decided that this computation would end when the columns' elements were equal up to the sixth decimal place. Hence, both limit supermatrices were obtained with powers of six. The resulting column vector is presented in table form, for both rural and off-shore scenarios in tables 4.5 and 4.6, respectively.

Table 4.5: Representation of the Limit Supermatrix Column Vector, for the rural exploration site.

GOAL	0.031428	**CPP**	0.008012	**VI**	0.003886	**A1**	0.016143	**A6**	0.010346
AP	0.353680	**CTR**	0.125032	**NI**	0.003811	**A2**	0.015287	**A7**	0.009775
MA	0.254198	**TLF**	0.014961	**EI**	0.002519	**A3**	0.010970	**A8**	0.015342
DU	0.050120	**M**	0.021889	**SF**	0.003414	**A4**	0.010704	**A9**	0.015635
SU	0.004789	**L**	0.007310			**A5**	0.010748		

Table 4.6: Representation of the Limit Supermatrix Column Vector, for the off-shore exploration site.

GOAL	0.044538	**CPP**	0.007544	**VI**	0.002090	**A1**	0.014549	**A6**	0.010366
AP	0.352049	**CTR**	0.096826	**NI**	0.001435	**A2**	0.013725	**A7**	0.009006
MA	0.271301	**TLF**	0.017203	**EI**	0.002158	**A3**	0.009603	**A8**	0.013271
DU	0.054926	**M**	0.027614	**SF**	0.001536	**A4**	0.010625	**A9**	0.013586
SU	0.005031	**L**	0.010413			**A5**	0.010603		

4.2.3 Decision Results and Discussion

In order to get the relative preferences of the alternatives, one takes the last nine elements of the limit supermatrix's column vector and normalizes using the best and worst alternatives. The same can be done in order to obtain the criteria prioritization order, using the remaining elements. The following formula is used to calculate the preference percentages $\mathrm{Pref}_{\%}$ of a x vector's i^{th} element:

$$\mathrm{Pref}_{\%,\mathrm{i}} = \frac{x_i - x_{min}}{x_{max} - x_{min}} \times 100 \tag{4.6}$$

where x_i are the vector elements, and x_{min} and x_{max} are the smallest and largest elements.

4.2.3.1 Rural Exploration Site

From table 4.5, A1 and A7 are the best and worst alternative, respectively. Regarding criteria (plus the GOAL), AP is the most relevant whereas the least relevant is EI. Using eq. (4.6), one obtains the results on tables 4.7 and 4.8.

According to the methodology employed and as seen in table 4.8, the most relevant criterion is aerodynamic performance, followed by mass-to-area ratio. Accordingly, the five best alternatives are the ones with better AP, even though the score of the fifth is very distant from the fourth - see table 4.7. It is noteworthy that from the first to the fourth best alternatives there is a difference in preference smaller than 15%, which indicates all these four alternatives have potential in this scenario. A1 leads in front of A9 due to its better MA. On the contrary, although A2 has a better MA than A8, the relative distance is smaller than in the previous case, and since A8 has a better Controlability (third most relevant criteria), it gets a better result than A2.

One may also verify that the type of exploration site is the fifth most relevant criterion after durability. With respect to the social acceptability factors, visual and noise impact are the most important, followed by safety. This is an example of the alternatives impact. Since there are alternatives with very good VI, coincident with the five best, this criterion is more relevant for the decision than SF, which intuitively

would be the most significant factor alongside with NI.

Table 4.7: Alternatives Preferences (eq. (4.6)), in a rural exploration site, according to the FANP method.

1^{st}	2^{nd}	3^{rd}	4^{th}	5^{th}	6^{th}	7^{th}	8^{th}	9^{th}
A1	A9	A8	A2	A3	A5	A4	A6	A7
100	92.03	87.42	86.55	18.77	15.29	14.60	8.98	0

Table 4.8: Criteria Prioritization (eq. (4.6)), in a rural exploration site, according to the FANP method.

1^{st}	2^{nd}	3^{rd}	4^{th}	5^{th}	6^{th}	7^{th}	8^{th}	9^{th}	10^{th}	11^{th}	12^{th}	13^{th}	14^{th}
AP	MA	CTR	DU	GOAL	M	TLF	CPP	L	SU	VI	NI	SF	EI
100	71.7	34.9	13.6	8.2	5.5	3.5	1.6	1.4	0.65	0.39	0.37	0.25	0

4.2.3.2 Off-shore Exploration Site

As in the previous scenario, A1 and A7 are the best and worst alternative, respectively - see table 4.6. AP is also the most important criterion, although the least relevant is NI. Using eq. (4.6), one obtains the results on tables 4.9 and 4.10.

In this scenario, the rigid wing systems, excluding A3, are once again the best alternatives. Furthermore, A2 is now a better choice than A9 and A8. This may be explained by an increase of the MA criterion importance, on which A8 and A9 are the worst, and decrease of the CTR criterion importance, on which the *Drag-mode* systems are better than A2. The increase of MA relevancy also leads to an increase of the preference for soft wing systems, as seen in table 4.9.

According with the preference percentages in table 4.9, one may say that in an off-shore exploration site, A1 is clearly the best choice, which is not so emphatic as in the previous scenario. Here, the difference for the second best alternative is around 15%, and almost 25% for the fourth.

Regarding criteria prioritization, one verifies in table 4.10 that logistics surpasses continuity of power production in importance, which makes sense due to the difficulties of accessibility, and installation of an on-ground platform in a high-seas location. Moreover, with respect to SAF, ecological impact is now the most relevant criterion, once again alongside with visual impact.

Table 4.9: Alternatives Preferences (eq. (4.6)), in an off-shore exploration site, according to the FANP method.

1^{st}	2^{nd}	3^{rd}	4^{th}	5^{th}	6^{th}	7^{th}	8^{th}	$\mathbf{9^{th}}$
A1	A2	A9	A8	A4	A5	A6	A3	A7
100	85.13	82.65	76.94	29.20	28.80	24.53	10.77	0

Table 4.10: Criteria Prioritization (eq. (4.6)), in an off-shore exploration site, according to the FANP method.

1^{st}	2^{nd}	3^{rd}	4^{th}	5^{th}	6^{th}	7^{th}	8^{th}	9^{th}	10^{th}	11^{th}	12^{th}	13^{th}	14^{th}
AP	MA	CTR	DU	GOAL	M	TLF	L	CPP	SU	EI	VI	SF	NI
100	77.0	27.2	15.3	12.3	7.5	4.5	2.6	1.7	1.0	0.21	0.19	0.03	0

Chapter 5: Wind Energy Potential in Portugal

In this chapter one intends to evaluate the wind resource potential for AWE in a region of central Portugal including the coastal area. First, the altitude range of interest for AWE is identified, considering both the vertical wind speed gradient and the airspace regulations of the country. Then, the fundamentals and equations used to determine vertical profiles of relevant quantities, such as wind speed and wind power density, are presented. Since AWE systems are omnidirectional, wind direction is not relevant, hence it is not object of study. Finally, the data used and the methodology employed are described and the results are presented and discussed.

5.1 Altitude range of interest for AWE

The purpose of AWE technology is to harvest energy in altitudes above the ones achieved by conventional wind turbines, which are generally around 100-$150\,\mathrm{m}$. Hence, this constitutes a lower boundary for the height range of interest.

The conventional technology is placed within the lowest surface of Earth's atmosphere - the surface layer (SL) - which typically constitutes 10% of the Atmospheric Boundary Layer (ABL) [187]. This layer, in turn, corresponds to the first 1 to $2\,\mathrm{km}$ of the troposphere, which is about $10\,\mathrm{km}$ high (depending on weather conditions), and it is where the effects of the planet's surface on the air motion, by action of the friction forces, are considered to be relevant [188]. On average, around the world, the wind speed tends to increase with height, although some exceptions can be found due to small scale phenomena such as turbulence fluctuations, low-level jet streams, or fronts [189]. As assessed in [11], up to $500\,\mathrm{m}$ of the ABL, this increase is significant, whereas above and up to $2\,\mathrm{km}$, it is very slow (nearly constant wind speed). Then, up to the tropopause, the speed increase is once again very significant, either because of the increase in the geostrophic wind or due to the appearance of jet streams (around the $8^{\mathrm{th}}\,\mathrm{km}$) [190]. Hence, for AWE, it is suggested that is not worth it to go higher than $500\,\mathrm{m}$, unless it is over $2\,\mathrm{km}$. However, airspace regulations also play a big role in the decision for the height range to be explored.

Aviation authorities divide the airspace into classes from A to G, with the latter being the least restrictive. Each class has its own rules, set by the International Civil Aviation Organization (ICAO), and although in general all countries follow these standards, each nation can adjust them to serve their own needs [169]. Class G usually corresponds to the airspace up to $750\,\mathrm{m}$ from ground level, if not close to controlled airspace areas (e.g. airports), and, given airspace complexity and use by other airspace users, it is taken as the most suited class for AWE [148]. In this class, operations may be conducted under instrument or visual flight rules.

In Portugal, according to the Aeronautical Information Service (AIS), class G may go up to $900\,\mathrm{m}$ [191]. Non-toy remotely piloted airplanes may fly in it provided that the flights are carried out in places or runways with areas whose characteristics are available in national aeronautical information publications, and only after authorization by the National Civil Aviation Authority (ANAC).

Thereby, considering both the typical vertical evolution of wind speed and airspace regulations, namely in Portugal, one assumes henceforth the height range of interest for the present work is from $150\,\mathrm{m}$ up to $500\,\mathrm{m}$. This is aligned with what most of AWE companies have been focused on so far.

5.2 Obtaining Vertical Profiles

In order to study the wind resource potential in Portugal within the aforementioned height range, one must obtain wind speed and power density vertical profiles.

5.2.1 Wind Speed Vertical Profile

Within ABL, namely in the SL, the interaction surface-air occurs in two primary forms: mechanical and thermal. The mechanical form is directly linked to the action of viscous forces which arise from the contact between the air flow and the surface. These forces create wind shear and alongside with the surface roughness induce turbulence. Considering only this effect, the wind speed variation with altitude may be described by the commonly referred "log-law", derived from Prandtl's work [192]: $V_w(h) = \frac{v^*}{k}\ln\left(\frac{h}{z_0}\right)$, where v^* is the friction velocity (assumed to be constant for the SL), $k \approx 0.41$ is the Von-Kárman constant, and z_0 is the surface roughness length. This equation is usually valid for the SL and, although this layer is typically referred as 10% of the ABL, as mentioned, its thickness (h_{SL}) varies with the surface roughness [44, 193, 194]: in off-shore or plain areas ($z_0 \sim 0.0002$-$0.005\,\mathrm{m}$), $h_{SL} \sim 200$-$250\,\mathrm{m}$; in rural/open field areas ($z_0 \sim 0.05$-$0.3\,\mathrm{m}$), $h_{SL} \sim 300$-$350\,\mathrm{m}$; in suburban and forest areas ($z_0 \sim 0.5$-$1\,\mathrm{m}$), $h_{SL} \sim 400$-$450\,\mathrm{m}$; in cities ($z_0 \sim 1.5\,\mathrm{m}$), $h_{SL} \sim 500\,\mathrm{m}$.

Regarding the thermal form of the surface-air interaction, it occurs by action of buoyancy forces. Due to solar radiation, Earth's surface heats up and then radiates heat back to the atmosphere, creating a vertical temperature gradient [188]. Hence, by convection, vertical air motion arises. The way this motion occurs defines atmospheric stability, which has a great influence in the vertical wind speed profile. There are several proposals to estimate the impact of atmospheric stability on the wind speed profiles [195]. In the present work, one resorts to the well-established "log-linear law" based on Monin-Obukhov similarity theory [196], as follows:

$$V_w(h) = \frac{v^*}{k}\left[\ln\left(\frac{h}{z_0}\right) - \Psi\left(\frac{h}{L^{Ob}}\right)\right] \tag{5.1}$$

Equation (5.1) includes a correction function $\Psi\left(\frac{h}{L^{Ob}}\right)$, which depends on the Obukhov Length. This characteristic length describes the effect of viscous and buoyancy forces on the turbulent flow, and it is often used to evaluate atmospheric stability: $L^{Ob} > 0$ indicates stable stratification of the atmosphere; $L^{Ob} < 0$ indicates unstable stratification; and $L^{Ob} = +\infty$ (or very large) indicates neutral stratification. This equation for the vertical wind speed profile is once again valid for the SL, however its applicability is very much related to the stability conditions [197], meaning it can resemble reality for a larger or smaller height range depending on the condition of stability.

A neutral atmospheric stratification occurs when the environmental lapse rate ($\Gamma = -\frac{dT}{dh}$), i.e. the rate at which temperature decreases with altitude, is equal to the adiabatic lapse rate, which in the troposphere is in average given by $\Gamma_{ad} = 6.5\,\frac{\mathrm{K}}{\mathrm{km}}$. This means that a parcel of air near the surface

which starts to rise, since it is warmer than the air above, does not continue to rise but it does not sink neither, as it achieves balance with the environment as soon as it cools. Thereby, there are no convection currents, meaning the stability correction function is equal to $\Psi\left(\frac{h}{L^{Ob}}\right) = 0$. It corresponds to the equation where only viscous forces are considered.

An unstable atmospheric stratification occurs when $\Gamma > \Gamma_{ad}$, and it is typical of diurnal conditions, with strong insolation. A rising parcel of air cools down at the adiabatic lapse rate, however, since the surrounding air cools down at a larger rate, the parcel of air continues to be warmer and consequently continues to rise. Therefore, the parcel of air is subjected to an upward buoyancy force, which stimulates convective mixing and turbulent flow, thus reducing wind shear. The stability correction function which better fits experimental results is the following [198]:

$$\Psi\left(\frac{h}{L^{Ob}}\right) = 2\ln\left(\frac{1+x}{2}\right) + \ln\left(\frac{1+x^2}{2}\right) - 2\arctan\left(x\right) + \frac{\pi}{2} \quad , \qquad x = \left(1 - 19.3\frac{h}{L^{Ob}}\right)^{0.25} \tag{5.2}$$

In a study performed at Delft University to estimate wind profile shapes for AWE production from wind speed measurements up to $600\,\mathrm{m}$ [199], it was verified that the "log-linear law" for unstable and neutral conditions fitted well the collected data up to around $500\,\mathrm{m}$, for both off- and on-shore locations. This means that eq. (5.1) alongside with eq. (5.2) can be applied at heights above the SL to produce a good estimate of the vertical wind speed profile.

Finally, a stable atmospheric stratification occurs when $\Gamma < \Gamma_{ad}$, and it is typical of nocturnal and dawn conditions, as the surface is colder. Hence, a rising parcel cooling down at the adiabatic lapse rate becomes colder than the surrounding air, and, by consequence of a downward buoyancy force, it sinks. Contrarily to the unstable condition, the air is stratified in a way that satisfies gravity, and no mixing occurs, unless a source of mechanical energy exists. This leads to larger wind speed gradients. The stability correction function which better fits experimental results is the following [198].

$$\Psi\left(\frac{h}{L^{Ob}}\right) = -\frac{h}{L^{Ob}} - \frac{2}{3}\left(\frac{h}{L^{Ob}} - \frac{5}{0.35}\right)e^{-\frac{0.35\,h}{L^{Ob}}} - \frac{10}{1.05} \tag{5.3}$$

In this case, the same study [199] showed that the "log-linear law" was only a good fit for the off-shore SL height range $(200\,\mathrm{m})$. For the on-shore area, this law followed the measurements up to the same height, which is below the usual SL thickness in this type of location, according to the aforementioned values. Hence, in this case, the law did not provide a good estimate for the whole SL height range. Therefore, in stable conditions, one should have some reservations when using it for heights above the SL, since it only provides a very rough estimate. For more precise estimates, real measurements, for example with LIDAR [200], should be used.

It is noteworthy to mention that the aforementioned equations only describe the mean behaviour of the wind speed, as time small-scale phenomena (e.g. turbulent gusts) are not accounted for. Moreover, regarding atmospheric stability, it is very volatile as it varies during the day, seasonally, and from place to place [199, 201, 202]. Hence, these equations only provide an estimate for the wind speed potential, and not necessarily absolute values for it.

5.2.2 Power Density Vertical Profile

From wind speed, one may derive the wind power density, which is a quantitative measure of the available wind energy at a given location. It is expressed in units of power per square meter of swept area [189], as follows:

$$P_w(h) = \frac{1}{2}\,\rho_{air}(h)\,V_w^3(h) \tag{5.4}$$

ρ is the air density, and its variation with height may be described by eq. (5.5) [189], where $p_0 = 101325\,\mathrm{Pa}$ and $T_0 = 288.15\,\mathrm{K}$ are pressure and temperature at the surface in standard atmosphere; $R_{air} = 287.1\,\mathrm{J/kgK}$ is the individual gas constant of air; Γ denotes again the environmental lapse rate; and $g = 9.80665\,\mathrm{m\,s^{-2}}$ is the gravitational acceleration.

$$\rho_{air}(h) = \frac{p_0}{R_{air}\,T_0}\left(1 - \frac{\Gamma\,h}{T_0}\right)^{\frac{g}{\Gamma R}-1} \tag{5.5}$$

Another relevant quantity for AWE, specially for on-board generation, is the amount of wind power passing through a vertical strip of unit width, ranging from height h_0 to h_1 above a given location [12]. Since on-board AWE systems fly in consecutive "figures of eight" of vertical amplitude $\Delta h = h_1 - h_0$, eq. (5.6) provides information about how much power is available in one "eight".

$$P_{w,\Delta h}|_{h_0}^{h_1} = \int_{h_0}^{h_1} \frac{1}{2}\,\rho(h)\,V_w^3(h)\,dh \tag{5.6}$$

5.3 Wind Speed and Surface Roughness Data used

The present work is supported on the results of a previous study, where mean wind speeds representative of the first $50\,\mathrm{m}$ of the surface layer were obtained for three regions of Portugal [203]. To calculate the regional wind fields, the meso-scale model REWIMET [204] was employed and data from NCEP/NCAR reanalysis, covering more than 40 years of climatology observations, was used. After identifying specific Circulation Weather Types for the regions under investigations and their monthly occurrence frequency, a weighted average was performed and the mean wind speed maps were evaluated.

Resorting to real measurements from anemometric stations, the author confirmed that computed wind speeds were in good agreement with measured data at a height of $20\,\mathrm{m}$. Hence, in the present work, one uses the former study's results to set the wind speed values at a reference height $h_{ref} = 20\,\mathrm{m}$. This allows the calculation of the friction velocity, required in eq. (5.1), as follows:

$$v^* = \frac{v(h_{ref})\,k}{\ln\left(\frac{h_{ref}}{z_0}\right) - \Psi\left(\frac{h_{ref}}{L}\right)} \tag{5.7}$$

It must be noted that v^* is assumed to be constant throughout the height range considered, although, in reality, this is only accurate for the surface layer. In order to take into account its dependence on height, vertical gradients of turbulent fluxes would have to be obtained, which is out of the scope of this study.

Another quantity necessary to obtain the wind speed vertical profiles is the roughness length z_0. In the *Global Wind Atlas* platform [205], its worldwide values are available. They were derived from the European Space Agency's Climate Change Initiative Land Cover (CCI-LC) dataset v2.0.7, which used Medium Resolution Imaging Spectrometer Instrument Fine Resolution to make a land cover, allowing afterwards the attribution of z_0 values, according to the type of terrain [206].

In the present work, one decided to estimate the wind resource potential for region C from Portugal ([203]), which corresponds to a rectangular area with its upper right corner on *Vila de Rei* ($39^o40'5''\mathrm{N}$, $8^o7'59''\mathrm{W}$) and lower left corner on an off-shore location ($38^o13'3''\mathrm{N}$, $9^o37'3''\mathrm{W}$). The mean wind speed map obtained in the former study for region C is shown on the left side of figure 5.1, while the surface roughness length is illustrated on the right side.

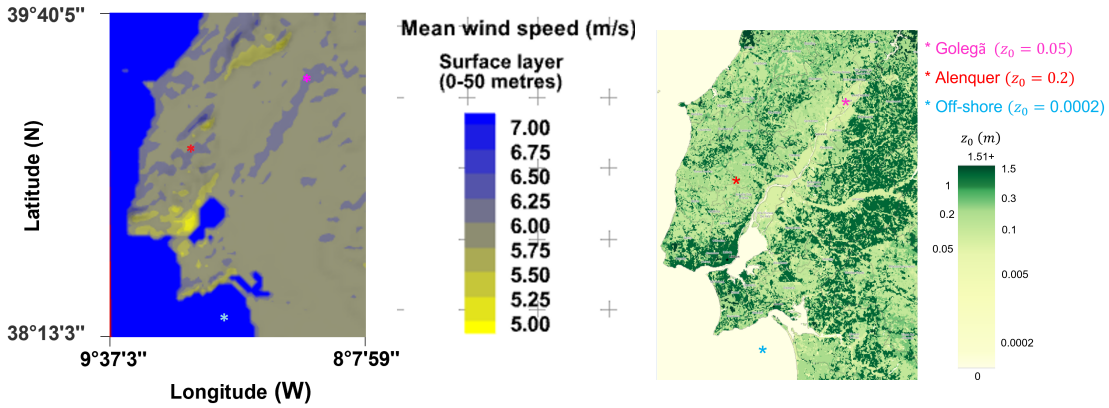

Figure 5.1: Mean wind speed and surface roughness length maps for the relevant region of study. Adapted from [203, 205].

5.4 Results and Discussion

As presented earlier, the wind speed data used consists of a temporal average covering more than 40 years, so it does not correspond to any specific atmospheric stability condition. Therefore, one decided to estimate the wind resource potential for three stability conditions using the wind speed data at the reference height of $20\,\mathrm{m}$ for all of them. Accordingly, one obtains a range of wind speeds and power densities which are expected to be representative.

Based on stability classes of Holtslag [198] and values used by Schelbergen [199], the Obukhov lengths employed in the present work are mentioned in table 5.1. It is noteworthy to mention that no "very stable condition" was selected in order not to decrease the applicability of eq. (5.1). Moreover, in the interest of using eq. (5.5), the lapse rates used are also presented in the table, although they have no direct correspondence to L^{Ob}. To obtain a more precise air density variation with height depending on stability conditions, one would have to resort to additional information (e.g. heat fluxes at the surface), which is not available. Also, neither L^{Ob} nor v^* should be considered constant with height. Hence, at the light of the previous assumptions, using a constant lapse rate to describe $\rho_{air}(h)$ is not considered deterrent.

Table 5.1: Obukhov lengths and Environmental Lapse Rates used in study. Adapted from [199].

Atmospheric Stability	L^{Ob} boundaries $[m]$	Representative L^{Ob} $[m]$	Representative Γ $[K/km]$
Unstable	-500 $\leq L^{Ob} <$ -200	-350	12
Neutral	$\lvert L^{Ob}\rvert >> 500$	10^{10}	6.5
Stable	$200 < L^{Ob} \leq 500$	350	3

5.4.1 Maps of $\mathbf{n_M}$ and $\mathbf{P_{w,\Delta h}}$ for different stability conditions

As justified in section 5.1, the height range of study is from $150\,\mathrm{m}$ up to $500\,\mathrm{m}$. Hence, mean wind speed maps were computed using eq. (5.1) for the following set: $h = \{150, 250, 350, 450\}$. Moreover, considering $\Delta h = 20\,\mathrm{m}$ (reasonable value for *Drag-mode* systems) and applying eq. (5.6), $P_{w,\Delta h}$ maps were also computed for the same set, whose values here correspond to the mean height ($\frac{h_0+h_1}{2}$). These results are presented in figure 5.2 for $h = 250\,\mathrm{m}$. This height was chosen due to the reduced applicability of eq. (5.1) in stable conditions, for larger altitudes, as mentioned in subsection 5.2.1. The results for the remaining altitudes are given in appendix B.

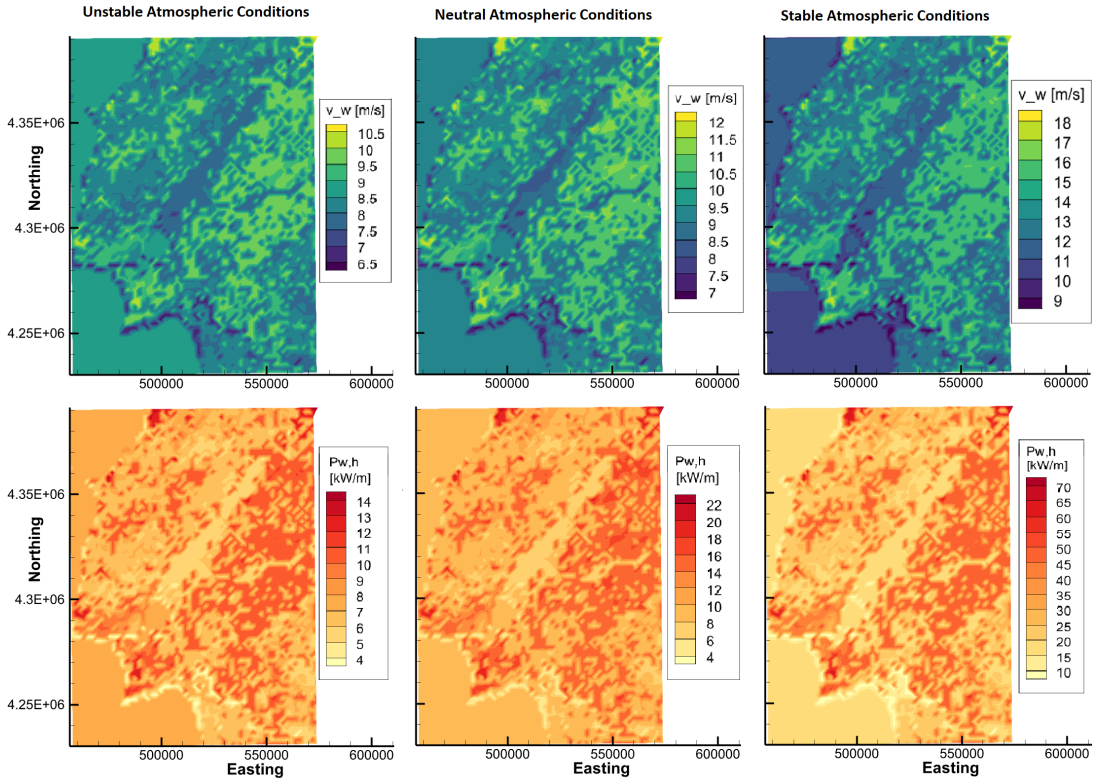

Figure 5.2: Maps of v^* at $h = 250\,\mathrm{m}$ (top) and $P_{w,\Delta h}|_{h_0=240\,\mathrm{m}}^{h_1=260\,\mathrm{m}}$ (bottom) for unstable, neutral, and stable atmospheric conditions. The maps' axes are given in UTM coordinates.

As depicted in the wind speed maps, the minimum wind speeds occur essentially at coastal areas and range from 6.5 to $9\,\mathrm{m/s}$. The correspondent $P_{w,\Delta h}$ ranges from $4\,\mathrm{kW/m}$, in unstable conditions, to $10\,\mathrm{kW/m}$, in stable conditions. Regarding the largest wind speeds, one may observe that these occur more to the interior of region C (eastwards), even though the maximum values also take place in coastal areas. These range from 10.5 to $18\,\mathrm{m/s}$. Regarding the power passing through a vertical strip of unit width, the maximum values vary from 14 to $70\,\mathrm{kW/m}$, which means that there might be an increase of around 400% in available power, from day to night (i.e. from unstable to stable atmospheric conditions).

It is also noteworthy to mention that from $h = h_{ref}$, where the wind speeds in region C ranged from 5 to $7\,\mathrm{m/s}$ (see figure 5.1, right), to $h = 250\,\mathrm{m}$, there was an increase in the wind speed variety. This variety is also more evident for stable atmospheric conditions, a consequence of the larger wind shear with altitude. Moreover, while at $h = h_{ref}$, the maximum wind speeds occurred in off-shore locations, here these occurred in on-shore sites. This is due to the fact that on-shore locations have higher z_0, thus

the wind speed is more vertically stratified. This aspect suggests that exploring wind energy at higher altitudes would be more advantageous in on-shore sites.

5.4.2 Vertical profiles for three exploration sites

In this section, vertical profiles for wind speed and power density are presented. Using equations (5.1) and (5.4), respectively, the profiles were computed for three specific regions (see figure 5.1), in line with the work developed in chapter 4. Two rural sites with different z_0 were selected: one in Golegã ($39^o22'46''\mathrm{N},\ 8^o28'53''\mathrm{W}$), with $z_0 = 0.05\,\mathrm{m}$, and the other in Alenquer ($39^o6'21''\mathrm{N},\ 9^o6'15''\mathrm{W}$), with $z_0 = 0.2\,\mathrm{m}$. The off-shore site is located in ($38^o18'50''\mathrm{N},\ 9^o0'8''\mathrm{W}$) and its $z_0 = 0.0002\,\mathrm{m}$. The results are showcased in figure 5.3

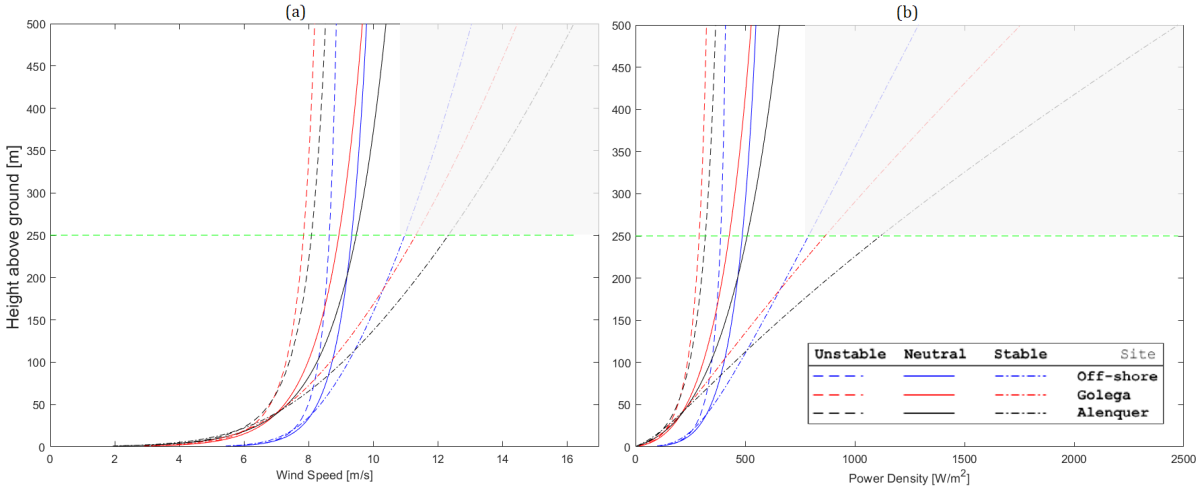

Figure 5.3: Wind speed (a) and power density (b) vertical profiles for three exploration sites and three stability conditions.

Regarding the wind speed profiles in atmospheric unstable conditions, one verifies that there is little stratification and that, within the specified height range, the wind speed off-shore is greater than on-shore. In neutral conditions, the stratification increases and, at the height of $h = 250\,\mathrm{m}$, the wind speed in Alenquer becomes larger than at the off-shore location. Finally, in stable atmospheric conditions, the wind speed stratification is high and, due to the larger z_0 in on-shore locations, the wind speed becomes greater than at the off-shore location: at $h = 120\,\mathrm{m}$ in Alenquer, and at $h = 200\,\mathrm{m}$ in Golegã.

It must be noted that the curves for $h > 250\,\mathrm{m}$, in stable conditions, are shaded for both V_w and P_w, since this is the typical surface layer height in off-shore locations, where it is smaller. As seen in section 5.2.1, above this altitude, the profiles do not provide good estimates. From fig. 5.3(b), in Alenquer at $h = 500\,\mathrm{m}$, one states an increase from $365\mathrm{W/m^2}$, in unstable conditions, to $2474\,\mathrm{W/m^2}$, in stable conditions. This is not reliable, hence caution must be exercised when evaluating these results.

With the purpose of further analysing the benefits of harnessing wind energy at higher altitudes, but also the type of location where it more profitable to do it, one constructed table 5.2. Considering, once more, eq. (5.6) with $\Delta h = 20\,\mathrm{m}$, one intends to compare the gain in $P_{w,\Delta h}$ of going up from $h = 100\,\mathrm{m}$ (typical height for conventional wind turbines) to $h = 250\,\mathrm{m}$, using:

$$\Delta P_{w,\Delta h}\big|^{\text{altitude}} = \frac{P_{w,\Delta h}\big|_{h_0=240\,\mathrm{m}}^{h_1=260\,\mathrm{m}} - P_{w,\Delta h}\big|_{h_0=90\,\mathrm{m}}^{h_1=110\,\mathrm{m}}}{P_{w,\Delta h}\big|_{h_0=90\,\mathrm{m}}^{h_1=110\,\mathrm{m}}} \times 100 \tag{5.8}$$

Moreover, the gain that is predictably achieved, when atmospheric stratification changes from unstable to stable, is also calculated for $h = 250\,\mathrm{m}$, as:

$$\Delta P_{w,\Delta h}|^{\text{stability}} = \frac{P_{w,\Delta h}|_{h_0=240\,\mathrm{m}}^{h_1=260\,\mathrm{m}}\Big|_{stable} - P_{w,\Delta h}|_{h_0=240\,\mathrm{m}}^{h_1=260\,\mathrm{m}}\Big|_{unstable}}{P_{w,\Delta h}|_{h_0=240\,\mathrm{m}}^{h_1=260\,\mathrm{m}}\Big|_{unstable}} \times 100 \tag{5.9}$$

These computations were done for the off-shore site and Alenquer's rural site, since they are expected to provide better wind resources than Golegã's, as depicted in figure 5.3.

Table 5.2: Power gains either when increasing exploration altitude or atmospheric stability, for off- and on-shore locations.

Location	Atmospheric Stability	$P_{w,\Delta h}\|_{h_0=90\,\mathrm{m}}^{h_1=110\,\mathrm{m}}$ $[kW/m]$	$P_{w,\Delta h}\|_{h_0=240\,\mathrm{m}}^{h_1=260\,\mathrm{m}}$ $[kW/m]$	$\Delta P_{w,\Delta h}\|^{\text{altitude}}$ $[\%]$	$\Delta P_{w,\Delta h}\|^{\text{stability}}$ $[\%]$
Off-shore	Unstable	6.95	7.76	11.7	103
	Neutral	8.06	9.74	20.8	
	Stable	9.53	15.78	65.6	
Alenquer	Unstable	4.93	6.37	29.2	251
	Neutral	6.83	10.18	49.0	
	Stable	8.99	22.34	148.5	

Table 5.2 confirms one of the major advantages of Airborne Wind Energy. By going up $150\,\mathrm{m}$ from the typical height of conventional wind turbines, the increase in available power is significant. This gain is even more noticeable in atmospheric stable conditions. In fact, a change from an unstable atmospheric stratification to a stable one leads to gains of over 100%. Although these results are only estimates and some factors are not being accounted for, this hints that the available power may double from day (unstable conditions) to night (stable conditions).

Regarding the type of exploration site, one confirms the previous observation that it may be more advantageous to climb in altitude in on-shore rather than in off-shore locations. Both gains, either in altitude or with changing stability, were found to be more significant in Alenquer.

Summing up, the airborne wind resource potential has been estimated for a region of central Portugal including the coastal area. It has been seen that the wind speed and, consequently, the wind power density widely vary with the atmospheric stability conditions. Therefore, when deciding for an exploration site, a probabilistic study of these conditions should be carried out in order to better understand the potential for extracting airborne wind energy. Moreover, a dependence also exists on the location's surface roughness length, leading to the conclusion that, most likely, the benefits of exploring high-altitude winds are greater in on-shore sites. Finally, regarding the three studied locations and considering only the available wind power, one concluded that the rural site of Alenquer is the best alternative for a potential implementation of a crosswind AWE system of *Drag-mode* type.

Chapter 6: Implementation of a Flying Experimental Testbed

After verifying that harnessing AWE has more potential in an on-shore location and concluding that, for a rural location, the on-board generation alternatives are very suitable, one intends to develop a small-scale flying testbed of a *Drag-mode* system. Firstly, the original aircraft is characterized geometrically as well as aerodynamically by wind-tunnel testing. Then, modifications towards an AWE *Drag-mode* system are implemented and their effects on the aerodynamics and stability of the aircraft are analysed. Finally, one studies the potential of electrical power production using wind-tunnel and flight testing.

6.1 Aircraft Geometrical Characterization and Modifications

The basis of the testbed is a radio-controlled aircraft of $780\,\mathrm{mm}$ length and $944\,\mathrm{mm}$ wing span - see figure 6.1. It has two types of control surfaces: ailerons for rolling and yawing, and elevators for pitching. The thrust, for take-off and landing maneuvers, is provided by a $2400\,\mathrm{kV}$ brushless motor and a $13\,\mathrm{cm}$ diameter 3-blade propeller, in a push configuration. Power is provided by a LiPo battery of $2200\,\mathrm{mAh}$ and $11.1\,\mathrm{V}$. The total weight of the aircraft, battery and the electronic speed controller is $m_{orig} = 0.5\,\mathrm{kg}$.

The aircraft has a semi-inverted V-tail connected, through two carbon-fiber booms, to a high wing of approximately trapezoidal shape with elliptical tips, of eccentricity $e_{tip} = 0.84$, to reduce induced drag. The aircraft's center of gravity (CG) is $60\,\mathrm{mm}$ behind the wing's leading edge. The distance between the wing's aerodynamic center, which is about 25% of the wing chord, and the tail's aerodynamic center is $l_{CA_{wg}-CA_{tl}} = 446\,\mathrm{mm}$. In figure 6.1, sketches of the wing, its aerodynamic profile, and the tail are displayed with their respective dimensions and in table 6.1, one presents important quantities which characterize geometrically these components. The tail is characterized by horizontal and vertical volume ratios, which are given by equations (6.1) and (6.2), respectively, where A_{HT} and A_{VT} are the projected horizontal and vertical tail areas.

$$V_H = \frac{l_{CA_{wg}-CA_{tl}}\, A_{HT}}{A_{wg}\, \bar{c}} \qquad (6.1)$$

$$V_V = \frac{l_{CA_{wg}-CA_{tl}}\, A_{VT}}{A_{wg}\, b} \qquad (6.2)$$

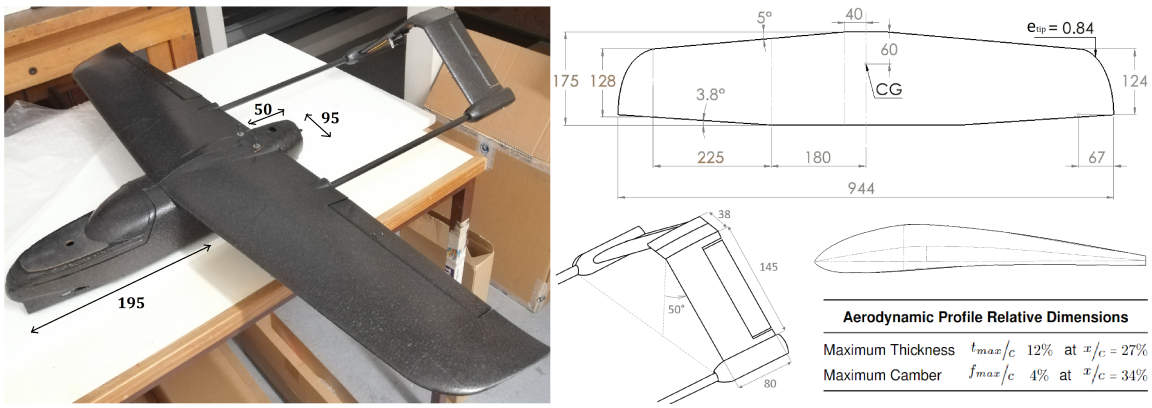

Figure 6.1: Original aircraft for the testbed, with sketches of the wing, aerodynamic profile and tail (with respective dimensions). Lengths are given in millimeters.

Table 6.1: Geometrical characteristics of the wing and tail.

		Wing				**Tail**	
Area, $\mathbf{A_{wg}}$	$0.14\,\mathrm{m}^2$	**Mean chord,** $\bar{\mathbf{c}}$	$0.148\,\mathrm{m}$	**Taper Ratio,** $\lambda_{\mathbf{wg}}$	0.73	$\mathbf{V_H}$	0.45
Span, $\mathbf{b}$	$0.944\,\mathrm{m}$	**Aspect Ratio,** $\mathcal{AR}$	6.4			$\mathbf{V_V}$	0.05

From the presented aircraft, one intends to develop a testbed for a *Drag-mode* AWE crosswind system. Hence, it has to be modified in order to carry electric generators on-board. Accordingly, two XPS foam (lightweight) adapters were hand crafted to serve as interfaces between the generators and the wing. Using hot wire and a blade, one tried to shape them in order to minimally increase the drag and to allow the cooling of the generators. Moreover, the inside is covered in aluminium foil to prevent the heat from the generators to melt the foam. The two generators were mounted, guaranteeing alignment and lateral symmetry, in sections that were originally thought to carry two motors for propulsion. Figure 6.2 shows, on the left side of the wing, one of the adaptors with the generator inside and, on the right side, the adaptor with the generator and respective 3-blade wind turbine of diameter $D_{rot} = 15.2\,\mathrm{cm}$, as well as a lateral view of the interface with the contours highlighted. Details on the generators will be provided in section 6.3. With these modifications, the aircraft's "ready-to-fly" mass became $m_{mod} = 0.65\,\mathrm{kg}$.

Figure 6.2: Interfaces wing-generator, electric generators and wind turbine rotors introduced.

As this constitutes the starting point of the project, it is not prudent nor possible to modify the aircraft to fully achieve a conventional *Drag-mode* flying system. It is necessary to go step by step and, therefore, at this stage, one decided not to include a tether in the system. Furthermore, it is important to mention that this setup is not optimized, rather it establishes foundations for future developments. Suggesting improvements is an expected outcome from this work.

6.2 Wind Tunnel Testing of the Original and Modified Aircraft

In order to characterize the aircraft in terms of its aerodynamics and static stability, one resorted to wind tunnel testing. The tests were performed in a laboratory of the Mechanical Engineering Department at Instituto Superior Técnico, where an open-return low-speed wind tunnel with an open section of area $A_{ts} = l_{ts} \times h_{ts} = 1.35 \times 0.8\,\mathrm{m}^2$ is located. As represented in figure 6.3, the airflow is produced by a centrifugal fan and then it flows through a settling chamber, a honeycomb structure to reduce swirl, and a number of screens to reduce longitudinal velocity variations as well as turbulence intensity. Then, before reaching the test section, it is subjected to a contraction with an area ratio of $9:1$, which increases flow speed and further improves its quality for testing. With the fan operating at 100% power, the maximum airflow velocity $V_{t\infty}$ achieved at the test section is about $10\,\mathrm{m/s}$. The turbulence intensity is estimated to be around 0.15% [207], thus it is considered negligible for this purpose.

In the test section, the model is mounted on a Shenck scale with its CG aligned with the support. The scale has 6 measurement cells that allow to determine three forces ($\mathrm{F_{x,y,z}}$) and three moments ($\mathrm{M_{x,y,z}}$). It also allows the variation of the angle of attack α of $\pm 30^o$. All measurements taken were within the scale limits. The setup and axis are displayed in figure 6.4.

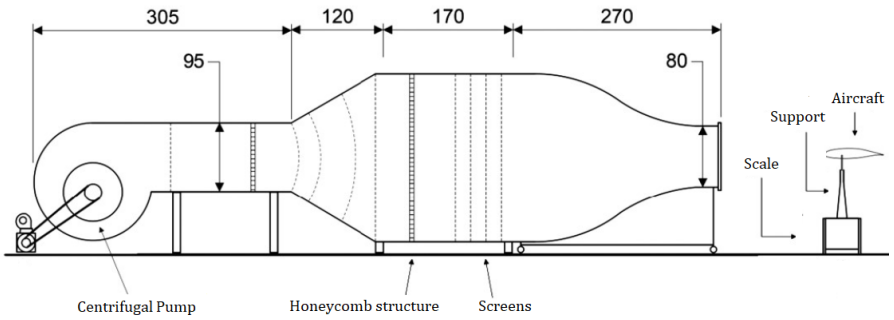

Figure 6.3: Schematic of the wind tunnel used in testing. Dimensions are in centimeters. Adapted from [207].

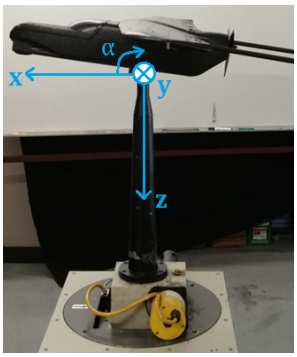

Figure 6.4: Axis of the measurement scale.

In addition, measurements of the dynamic pressure (p_{din}), in $\mathrm{mmH_2O}$, and temperature (T), in $^{\mathrm{o}}\mathrm{C}$ are also provided. The first, which must be multiplied after by 9.80638 to get Pascal units, is obtained by a digital micromanometer (FCO12 from Furness Controls Limited). The second is obtained by a sensor (AP9512TBLK from APC). Both are connected to an Arduino. The uncertainty in these measurements affect the calculation of the airflow velocity, but is expected do be less than 1%, as estimated in [207].

The user interface is the program AeroIST [208], which processes the aforementioned measurement values. Among other aspects, it allows to define the scale of the fan's motor operation (0 to 100%), which implicitly corresponds to the airflow velocity, and the angle of attack of the model in the scale. Moreover, it allows to define the number of measurements per iteration and an integration time to determine the mean value of each measurement. It was established that the most precise results were obtained for an integration time of $10\,\mathrm{s}$ (maximum possible). One can also define the time of stabilization, which is the time given to the airflow to stabilize after each iteration (modification of the model's attitude, namely its angle of attack). Before each test, a calibration of the scale is automatically done to remove the contribution of the model's weight in the forces and moments measured.

6.2.1 Testing and Post-processing Procedures

To analyse both the original and modified aircraft, one performed a test with the motor scale at 100%, covering an angle of attack range of $[-16^o, 26^o]$ with a 2^o step and a $5\,\mathrm{s}$ stabilization time. In each iteration, i.e. for each angle of attack, ten measurements with an integration time of $10\,\mathrm{s}$ were taken. In addition, in order to eliminate the contribution of the model support to the force in x-direction ($F_x^{\mathrm{no\_model}}$) in the post-processing results phase, one also performed a test in the same conditions but without the aircraft mounted and, evidently, without varying the angle of attack.

From the measurements obtained for each angle of attack, one determined the lift (C_L) and drag (C_D) coefficients as well as the pitch moment coefficient (C_{My}), about the CG. The lateral force coefficient (C_{F_y}) and the yaw (C_{Mz}) and roll (C_{Mx}) moment coefficients are also determined, but they are expected to be approximately constant and zero since both the yaw and bank angle are null. At this stage, one

decided not to study lateral aerodynamics and stability of the aircraft since the correspondent coefficients are not relevant to estimate maximum power production, as seen in sections 2.2-2.4. Moreover, all the modifications introduced are longitudinally made and keep lateral symmetry so, in that sense, the aircraft should behave in the same way as the original.

The aforementioned quantities are obtained from the following equations:

$$C_{L,F_y} = -\frac{F_{z,y}}{p_{din}\, A_{wg}} \qquad (6.3) \qquad C_D = -\frac{(F_x - F_x^{\text{no\_model}})}{p_{din}\, A_{wg}} \qquad (6.4) \qquad C_{Mx,y,z} = \frac{M_{x,y,z}}{p_{din}\, A_{wg}\, \overline{c}} \qquad (6.5)$$

6.2.1.1 Measurements Uncertainty

As in any other experimental study, there is uncertainty associated to the measurements due to the instruments limitations and techniques applied. In this particular case, quantifying uncertainty is to determine, for each angle of attack, a range of values about a sample mean of each aerodynamic coefficient. Usually, in Engineering, in order to the results have statistical meaning, this range must be obtained with a confidence level of 95%.

According to Coleman $\&$ Steele [209], a "Student's t-distribution" has been found to describe many real cases of experimental and instrument variability. A set of N measurements of the variable X (representative of the aforementioned aerodynamic coefficients) is described by its mean value $\overline{X}$ and sample standard deviation s_X, which are respectively given by:

$$\overline{X} = \frac{1}{\mathrm{N}} \sum_{i=1}^{\mathrm{N}} X_i \qquad (6.6) \qquad s_X = \sqrt{\frac{1}{\mathrm{N}-1} \sum_{i=1}^{\mathrm{N}} (X_i - \overline{X})^2} \qquad (6.7)$$

With a confidence level of 95%, the uncertainty associated to the measurement of X is given by the range defined as:

$$\overline{X} \pm t_{95}\, \frac{s_X}{\sqrt{N}} \qquad \xrightarrow[\mathrm{N}=10]{t_{95}=2.262} \qquad \overline{X} \pm 0.715\, s_X \qquad (6.8)$$

This uncertainty range is hereinafter represented in the graphical results in the form of error bars.

6.2.1.2 Aerodynamic Corrections

A wind tunnel is a very powerful tool to simulate a free airflow and estimate aerodynamic quantities of a given model. However, it is not ideal and corrections must be applied to the measured values, due to the streamline curvature that arises from the blockage the model produces on the flow and from the development of boundary layers, which in a closed-section tunnel is caused by the walls and in an open section tunnel by the interaction with the surrounding air at rest (free shear layers). Following the procedures of Barlow, Rae $\&$ Pope [210] for open-section wind tunnels, the following corrections must be considered:

- **Solid Blockage**: in an open-section wind tunnel, if the blocking frontal area of the model is less than 25% of the section area A_{ts}, then the corrections are negligible. That is the case, since the blockage area is estimated to be $0.175\,\mathrm{m}^2$ in the worst scenario ($\alpha = 26^o$), which is about 16% of A_{ts}.
- ***Downwash* effects**: in a free airflow, the vortices generated at the wing tip, which induce an angle to the flow (*downwash*) and consequently induce a drag force, may expand freely to "infinite". However,

in the test section, due to the free shear layers that form from the interaction between the airflow and the air at rest in the lateral boundaries, these vortices are constrained and concentrate closer to the wing tip. Hence, there is an increase of the downwash effect on the wing, which reduces the lift force (decrease in the effective angle of attack) and increases the drag force, via induced drag. To eliminate these effects from the measured values, one may fix the lift force measurements and attribute to each of them a smaller angle of attack and drag values. In the coefficients, the corrections are [210]:

$$\alpha_c = \alpha_u + \delta \frac{A_{wg}}{A_{ts}} C_L \tag{6.9}$$

$$C_{D,c} = C_{D,u} + \delta \frac{A_{wg}}{A_{ts}} C_L^2 \tag{6.10}$$

where α_u and $C_{D,u}$ are the measured angles of attack and drag coefficients (uncorrected), $\frac{A_{wg}}{A_{ts}}$ is the ratio between the wing area and the tunnel section area, C_L is the measured lift coefficient, and $\delta = -0.17$, which is obtained from figure 6.5 by assuming uniform wing loading and using:

$$\lambda_{ts} = \frac{h_{ts}}{l_{ts}} = \frac{0.8}{1.35} \approx 0.6 \tag{6.11}$$

$$k_{tb} = \frac{b}{l_{ts}} = \frac{0.944}{1.35} \approx 0.7 \tag{6.12}$$

Graphically, these corrections mean that there is a left shift on the $C_L(\alpha)$ curve, and a left and down shift on the $C_D(\alpha)$ curve.

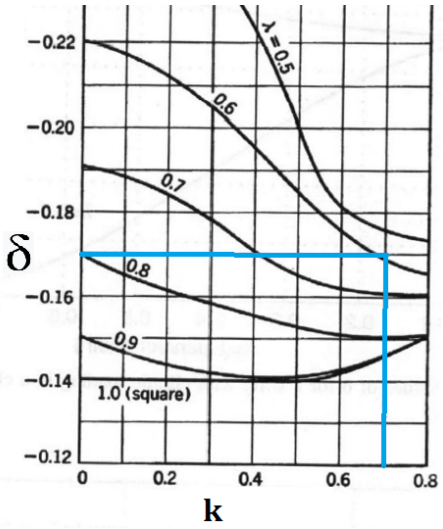

Figure 6.5: δ factor for downwash aerodynamic corrections. Adapted from [210].

6.2.2 Results and Discussion

As mentioned, two tests were performed: one for the original aircraft and one for the modified aircraft. In the latter, the aircraft was tested without the on-board rotors mounted, since that, for the purpose of AWE harvesting, one wants to know solely the wing's aerodynamic coefficients - see eq. (2.9).

In order to compare the results of each test, one has to guarantee their conditions are similar, since they were performed in different days. Namely, the Reynolds number must not differ typically more than 5%. It is given by eq. (6.13):

$$Re = \frac{\rho_{air}\, \overline{c}\, V_{t\infty}}{\mu_{air}} \tag{6.13}$$

$$V_{t\infty} = \sqrt{\frac{2\, p_{din}}{\rho_{air}}} \tag{6.14}$$

where: ρ_{air} is the density of air obtained from the perfect gas law, with $R_{air} = 287.1^{J}/_{kgK}$ - see eq. (6.15) [44]; $\overline{c}$ is the mean wing chord; $V_{t\infty}$ is the airflow velocity obtained from eq. (6.14); and μ_{air} is the fluid's dynamic viscosity, which is obtained from eq. (6.16) [44]. In table 6.2, one presents values of the relevant quantities to determine the Reynolds number of each test. The values of p_{din} and T correspond to mean values of the measurements. In turn, p_{stat} is the static air pressure of the test room, which was obtained from an analog barometer with an uncertainty of $\pm 0.25\,\mathrm{kPa}$.

$$p_{stat} = R_{air}\, \rho_{air}\, \left(\overline{T}\,[^oC] + 273.15\right) \tag{6.15}$$

$$\mu_{air} = \frac{1.458 \times 10^{-6}\, \left(\overline{T}\,[^oC] + 273.15\right)^{1.5}}{\left(\overline{T}\,[^oC] + 273.15\right) + 110.4} \tag{6.16}$$

Table 6.2: Relevant quantities to determine the Reynolds number of each wind tunnel test.

Aircraft	$\boldsymbol{p_{stat}}\,[kPa]$	$\boldsymbol{\overline{T}}\,[^oC]$	$\boldsymbol{p_{din}}\,[Pa]$	$\boldsymbol{\rho_{air}}\,[kg/m^3]$	$\boldsymbol{V_{t\infty}}\,[m/s]$	$\boldsymbol{\mu_{air}}\,[\mu Pa.s]$	$\boldsymbol{Re}\times 10^{-4}$
Original	102.0	25.27	61.28	1.190	10.15	18.385	9.7239
Modified	101.5	25.19	61.98	1.191	10.20	18.382	9.7823

The wind tunnel tests were performed with Reynolds numbers differing by 0.6%, which is perfectly acceptable. Hence, the results are comparable. As expected, the curves for $C_{Mx,z}$ and C_{Fy} were approximately constant and equal to zero and since they are not relevant for the present study, they are omitted.

Next, in figures 6.6 and 6.7, one presents the $C_L(\alpha)$ and $C_D(\alpha)$ curves, respectively.

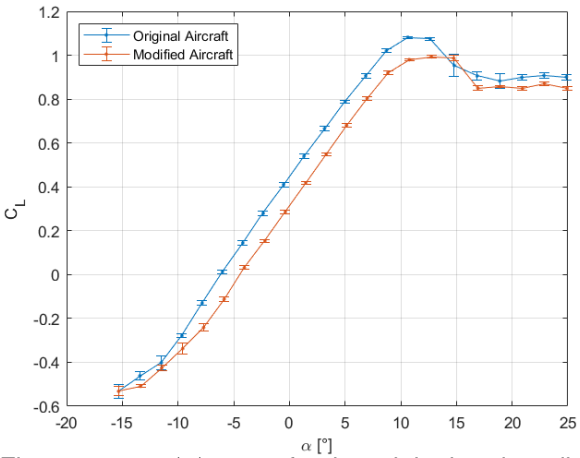

Figure 6.6: $C_L(\alpha)$ curve for the original and modified aircraft.

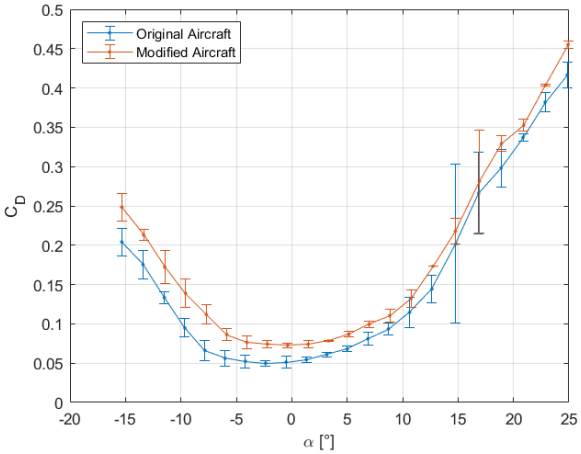

Figure 6.7: $C_D(\alpha)$ curve for the original and modified aircraft.

First of all, the curves in figure 6.6 reflect little uncertainty in the measurements. The analysis of the original aircraft's $C_L(\alpha)$ curve shows a maximum lift coefficient of approximately 1.1 for $\alpha = 11^o$. From this angle of attack, aerodynamic stall occurs. It is smooth, which, from a two-dimensional point of view of the wing, is typical of thick aerodynamic profiles (trailing-edge stall for ${}^t/_{\overline{c}} \geq 12\%$ [44]), as it is the case. In the deep-stall region ($\alpha > 17^o$), the C_L values tend to stabilize. Moreover, one can also identify the zero-lift angle of attack to be approximately $\alpha_{0,orig} \approx -6^o$ and the curve slope, in the linear region, to be equal to $\frac{dC_L}{d\alpha}\big|_{orig} \approx 0.0697/^o$.

When analysing the impact that the modifications on the aircraft's wing brought to the generation of lift, one verifies that these almost did not affect the rate of C_L with α. In fact, in the linear region, $\frac{dC_L}{d\alpha}\big|_{mod} \approx 0.0712/^o$, which corresponds to a variation in the curve's slope of only 2%. However, there was a decrease in C_L values for the whole α range. The maximum lift coefficient became approximately equal to 1 at $\alpha = 13^o$, which represents a 9% decrease. Also, the zero-lift angle increased to $\alpha_{0,mod} \approx -4^o$. Furthermore, one verifies that the stall behaviour remained the same.

With respect to figure 6.7, one may observe that the uncertainty associated to the measurements of the drag force is larger, as it was also verified in [207]. This is specially true in the stall region ($\alpha > 10^o$ for the original aircraft and $\alpha > 13^o$ for the modified one). In fact, the Reynolds number of the tests is about 10^5, which means the airflow around the model, namely the wing, is expected to remain mostly laminar

[44]. Hence, in the beginning of stall, when the boundary layer detaches from the wing, reverse flow cells appear and vortex shedding in the wake occurs. As there are no turbulent mechanisms to dissipate energy, flow fluctuations are intense. Since flow separation is responsible for a massive increase in pressure drag, then the uncertainty in measuring this force also increases. Contrarily, in the deep stall region ($\alpha > 19^o$) the separated boundary layer stabilizes and the separation cells are fragmented in smaller ones [211], reducing the fluctuations and by consequence the uncertainty in the measurements, as observed. Moreover, at this point, transition to turbulent flow may have occurred, enhanced by the adverse pressure gradient, thus helping in the energy dissipation and flow stabilization.

Regarding the C_D values, there is a bucket zone in the α range of $[-5^o, 5^o]$, with minimum values of about 0.05 for the original aircraft and 0.07 for the modified one. Hence, there was an increase of 40%, which was expected since there was an increase of the frontal area due to the wing-generator interfaces. It should be noted that these values for C_D correspond not only to the wing's drag but also to the tail as well as booms and fuselage, which have a relevant parasitic drag contribution. Furthermore, for AWE purposes, one should include the contribution of the tether, which is usually very significant, especially in small-scale systems, as pointed out in section 2.6.

As seen in section 2.4, optimal AWE harvesting with a *Drag-mode* system occurs when the on-board wind turbine rotors increase the flying system's (kite+tether) drag by 50%. To understand how this testbed is characterized in that matter, one may use equation (2.5) to estimate a tether's drag coefficient. Considering a mean operational height of $h = 50\,\mathrm{m}$ (reasonable for the scale of the aircraft) and an elevation angle $\theta = 30^o$, one requires a tether of length $l_t = 100\,\mathrm{m}$. Assuming a cross section of width $w_t = 2\,\mathrm{mm}$ and $C_\perp = 1$ [212], one obtains $C_{D,t} = 0.357$. Considering that the kite mainly operates at $\alpha = 9^o$ (as it will be further justified), its drag coefficient is about 0.11 - see figure 6.7 - making the total flying system's drag coefficient be $C_{D_{FS}} = 0.467$. By using equation (2.17) with the ideal induction factor ($a = 1/3$), one gets $N_{rot}\, A_{rot} = 0.037$. In the present testbed, $N_{rot} = 2$, which means that for optimal power production one must have wind turbine rotor diameters of $15.3\,\mathrm{cm}$, as it is approximately the case.

Next, in figures 6.8 and 6.9, one presents the $C_{My}(\alpha)$ and $V_{stall}(\alpha)$ curves, respectively.

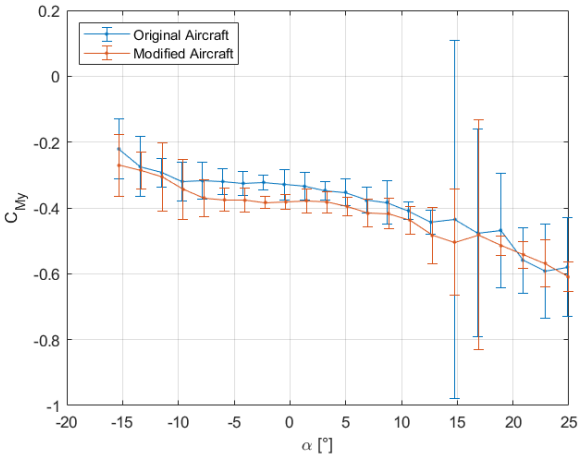

Figure 6.8: $C_{My}(\alpha)$ curve for the original and modified aircraft.

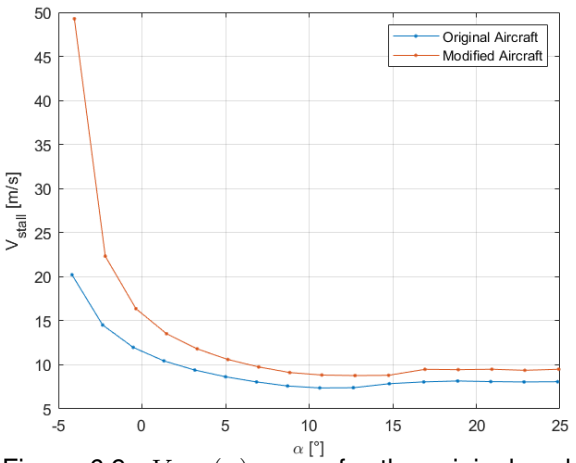

Figure 6.9: $V_{stall}(\alpha)$ curve for the original and modified aircraft.

As depicted in figure 6.8, the measurements of the pitch moment about the aircraft's CG show, for

the whole α range, a larger uncertainty than the previous ones (especially great at post-stall angles, once more). During the test, one verified there were some vibrations of the tail, which were particularly stronger for larger absolute values of α. Since the tail's lift plays a major role in the pitch moment, for longitudinal stability purposes, this may explain the larger uncertainty of the measurements.

From the same figure, one may also observe that the aircraft has a great tendency to pitch down. With the modifications, there was an increase, in absolute values, of C_{My}. This was expected since the generators were placed at the leading edge of the wing, hence having their weight contributing for a negative moment about the original aircraft's CG.

When modifying the aircraft, one of the concerns was the effect on the longitudinal static stability. This can be assessed by comparing the static margin values, which are obtained from the following equation:

$$K_n = -\frac{dC_{My}/d\alpha}{dC_L/d\alpha} \tag{6.17}$$

Being the slope of the curve for the original and modified aircraft approximately equal to $\frac{dC_{My}}{d\alpha}\big|_{orig} = -0.004/^o$ and $\frac{dC_{My}}{d\alpha}\big|_{mod} = -0.0024/^o$, respectively, then the static margins are $K_n^{orig} = 5.74\%$ and $K_n^{mod} = 3.37\%$. This corresponds to a 41% decrease. The original static margin was already small and this reduction, although it maintains the aircraft theoretically stable, may cause some difficulties in a leveled flight.

The curves in figure 6.9 represent, for each angle of attack, the minimum velocity required to keep a leveled flight, i.e. the velocity at which the aircraft's lift force is equal to its weight. It is given by:

$$V_{stall} = \sqrt{\frac{2\,m\,g}{C_L\,\rho_{air}\,A_{wg}}} \tag{6.18}$$

where $g = 9.80665\,\mathrm{ms}^{-2}$ is the gravitational acceleration and $\rho_{air} = 1.19\,\frac{\mathrm{kg}}{\mathrm{m}^3}$ is the air's density at which the wind tunnel tests were performed - see table 6.2.

Naturally, the modifications led to an increase of the aircraft's weight, increasing its V_{stall}, however it was not significant. For the typical α range of operation, the stall velocity is around 9 to $15\,\mathrm{m/s}$. When flying, it is important to keep the aircraft's speed relatively higher than the V_{stall}, since, below it, the aircraft will start to fall and, as seen before, the tendency is to pitch down which increases the speed of the fall.

Finally, one presents, in figures 6.10 and 6.11, the $\frac{C_L}{(C_D+C_{D,t})}(\alpha)$ and $\frac{C_L^3}{(C_D+C_{D,t})^2}(\alpha)$ curves. The previous refers to the aircraft's aerodynamic efficiency (original, modified and with tether), whereas the latter specifies an important quantity for AWE maximum power production (Cf. eq. (2.9)). For that matter, one uses the previously estimated $C_{D,t} = 0.357$.

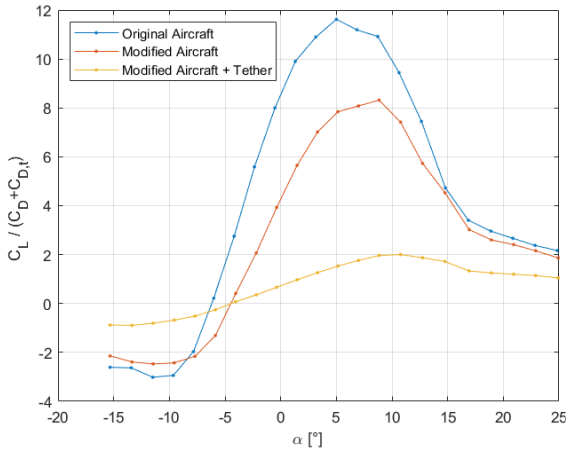

Figure 6.10: $\frac{C_L}{(C_D+C_{D,t})}(\alpha)$ curve for the original and modified aircraft ($C_{D,t} = 0$), as well as for the modified aircraft with a tether.

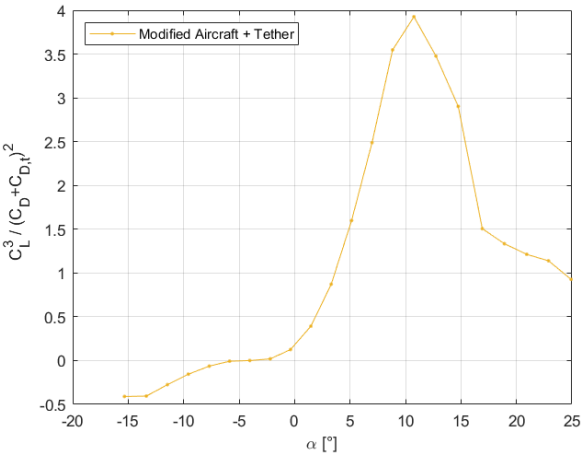

Figure 6.11: $\frac{C_L^3}{(C_D+C_{D,t})^2}(\alpha)$ curve for the modified aircraft with a tether.

Hypothetically, considering the implementation of a complete crosswind AWE system, i.e. the modified aircraft with a tether, one must analyse the curve of figure 6.11. The maximum value is about 4, which is achieved at an angle of attack of approximately 11^o. At that angle, the estimated aerodynamic efficiency of the flying system is about 2 (see fig. 6.10).

By applying equation (2.9) with $C_R \approx C_L$, $\theta = 30^0$, $\rho_{air} = 1.19\,\frac{\text{kg}}{\text{m}^3}$, $A_{wg} = 0.14\,\text{m}^2$, and $V_w = \frac{3\,V_{t\infty}\,(C_D+C_{D,t})}{2\,C_L\,\cos\theta} \approx 8.8\,\text{m/s}$ (cf. eq. (2.10); $V_a = V_{t\infty} = 10.2\,\text{m/s}$), one obtains a $22\,\text{W}$ maximum usable power which can be extracted from the wind with the current wing (and assumed tether) flying in crosswind. However, operating at this angle of attack means that the aircraft is close to stall, thus it is more prudent to operate at a lower angle, say $\alpha = 9^o$. At this angle, the aerodynamic efficiency of the modified aircraft is maximum, while with the tether is still approximately equal to 2. In that case, $\frac{C_L^3}{(C_D+C_{D,t})^2} = 3.5$ and the maximum usable power is $19\,\text{W}$, which constitutes a reduction of only 14%.

6.3 Obtaining Electric Power On-board

As mentioned, one intends to develop a small-scale flying testbed of a *Drag-mode* system for Airborne Wind Energy harvesting. Being the starting point of this venture, one decided not to include a tether in the system. The contrary would bring several complications, which at this stage would not allow to perceive the viability and potential of this testbed. For example, the piloting of the aircraft would be much more challenging - there is no automatic control yet. Also, passing the electrical power produced to a ground station, via tether, would elaborate the required electronics, a topic that requires specific competences in technical fields out of the scope of the present work. Hence, with the first version of the testbed, one intends to fly the aircraft and assess if and how much power can be harvested from the wind, keeping the electronics as simple as possible. Accordingly, one only requires two electric generators, with their respective turbines, and a simple electrical circuit. Both are described next.

6.3.1 Electric Generators

Every company developing prototypes of *Drag-mode* systems uses, for both take-off/landing maneuvers and electric generation, brushless direct current (DC) generators/motors. These type of generators

are known to be very efficient, reliable and with a long lifespan [213], despite their high cost upfront. Moreover, they are light and require low maintenance. These generators provide a 3-phase alternating voltage, which means that, to obtain a constant voltage output, one has to use a 3-phase rectifier such as a full bridge diode rectifier [214].

Although the aforementioned alternative is the most suitable, to minimize costs and wishing to keep the electronics as simple as possible, one decided to use two brushed DC motors, as generators, which were already available in the laboratory. These type of generators, on the contrary, are heavier, less efficient and have a lower lifespan. A schematic of this type of generator is presented in figure 6.12.

The working principle is the following: as the generator's shaft rotates, the commutator ring, which is connected to the rotor coils, also rotates. Since they rotate within the magnetic field created by the stator magnets, electric current is generated by induction. It flows through a commutator ring plate, then through a brush and finally to the positive terminal. Returning from the negative terminal, in a closed circuit, it flows back by the inverse way. The brushes are fixed, but the commutator ring rotates with the rotor so that, when the current in the coils inverts direction, the output current direction in the terminals remains the same. Hence, the ring is composed by pairs of plates, the poles, which allow the alternate contact with the brushes. The generators used in the present work have 2 pairs of poles. It is the friction between the brushes and the rotating ring that increases the maintenance needs and reduces the generator's lifespan. At high rotating speeds, sparking may occur, with corresponding energy losses.

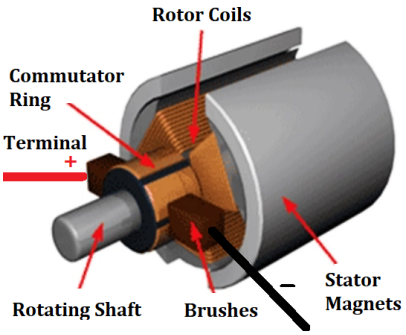

Figure 6.12: Schematic of a brushed DC generator/motor. Adapted from [215].

In order to use the two brushed DC motors/generators available for wind energy harvesting, the turbines have to be mounted. With that purpose, an adaptor to extend the generator's axis must be added. In figure 6.13, one shows a close-up of the generator and respective adaptor. The adaptor was glued to the generator's axis using epoxy resin to increase structural resistance. It is important to guarantee that both the axis and the adaptor are perfectly aligned, so that no vibrations occur while rotating with the turbines. At the scale of these generators, achieving perfect dynamic balancing is a particularly challenging task.

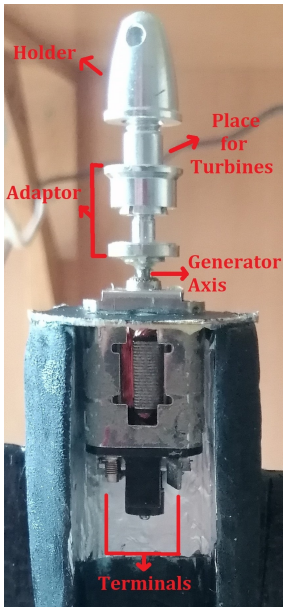

Figure 6.13: Brushed DC generator and turbine adaptor.

Regarding the generator's characteristics, no information was available either about its power output or its past workload. Hence, one did not know how they would behave when harvesting power from an airflow, using wind turbines. Accordingly, it was of most interest to estimate the machine's maximum voltage of operation as well as its electrical efficiency.

In general, this type of small size motors have a supply voltage of 1.5, 3, 6, 9 or $12\,\mathrm{V}$. Hence, using a DC power source, these voltages were supplied to the motor. By evaluating the unloaded shaft's rotating speed and by listening to the noise

produced in each test, one estimates that their supply voltage is $9\,\mathrm{V}$. It is not required to know the exact value, just an estimate so that one may perceive if the power production using the wind turbines is potentially leading to a generator overloading situation or not.

6.3.1.1 Determining the Motor/Generator Efficiency

Concerning electrical efficiency, it is well known that, in general, the efficiency of a machine working as a generator is greater than when working as a motor, since magnetic flux losses are not as critical. Hence, one may determine the motor's efficiency, which is a relatively simple process, and assume that the generator's efficiency is equal or greater than it. The motor's electrical efficiency is obtained by the ratio between the mechanical output power and the electrical input power, as:

$$\eta_{elec} = \frac{P_{mech}}{P_{elec}^{in}} = \frac{{}^{2\pi}/_{60}\; n\; Q_M}{U_{in}\; I_{in}} \tag{6.19}$$

where n_M is the rotational speed of the shaft, in RPM; Q_M is the motor's torque, in $\mathrm{N.m}$; and U_{in} and I_{in} are the input voltage and current, respectively. Both the input current and voltage, as well as the output torque are linearly related with the output angular speed. Hence, one only requires two points to determine each characteristic curve of the motor and subsequently its electrical efficiency.

Accordingly, with a DC power source, one supplied approximately $8.5\,\mathrm{V}$ (slightly less than the previously estimated voltage) to each motor, and obtained a set of measurements in two operational states:

- **Free-rotation**: Having only the adaptor mounted on the generator (without the holder), one measured the input current as well as the maximum angular speed. Since there is no load applied to the generator, one assumes the torque produced is null (it is very small).
- **Mechanical Stall**: In this measurement, a high load is applied to the motor so that, when the input voltage is provided, it generates a torque but it does not rotate - it stalls. This leads to a decrease in the input voltage and an increase in the input current. This measurement has to be done quickly to prevent the overloading of the motor. The setup used is shown in figure 6.14: the turbine was mounted to provide support for the load, which was a $0.45\,\mathrm{kg}$ weight hanging by a string. Under it, there was a scale measuring the weight's mass. When the voltage is imposed to the motor's terminals the torque generated reduces the mass being measured at the scale. The difference to the original value multiplied by the gravitational acceleration as well as by the horizontal distance between the string and the generator's axis gives the torque generated. Hence, in this case, one measured both the input voltage and current, as well as the difference in weight.

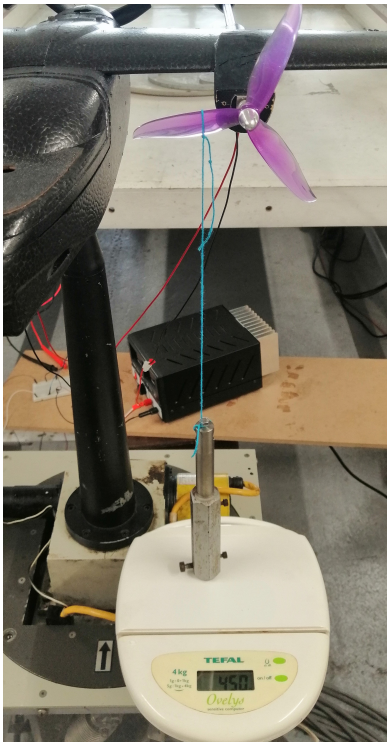

Figure 6.14: Setup for motor stall measurements.

The measurements of the current were performed using a *7551 Yokogawa* digital multimeter, with an uncertainty of $\pm 0.001\,\mathrm{A}$. The angular speed measurements were

obtained by a digital photo tachometer (*HIBOK 22*), with an uncertainty of $\pm 1\,\mathrm{RPM}$. Finally, the uncertainty associated to the weight's mass measurement is $\pm 1\,\mathrm{g}$, while the one associated to the measurement of the horizontal distance between the string and the axis is $\pm 0.05\,\mathrm{cm}$.

6.3.1.2 Results and Discussion

The resulting measurements are presented in table 6.3. Since the input current and voltage, as well as the motor's output torque have a linear correlation with the angular speed, then these measurements represent the end points of the motor's characteristic curves: $I_{in}(n)$, $U_{in}(n)$ and $Q_M(n)$. By dividing each resulting equation by the maximum value, one obtains the normalized characteristic curves, which are displayed in figure 6.15. On the same figure, one also presents the normalized $P_{mech}(n)$ curve and the $\eta_{elec}(n)$ curve, for each motor (M1 and M2).

Table 6.3: Measurements of the input current and voltage, and of the output angular speed and torque, with the motor in free rotation and mechanical stall. In free rotation, one assumes no torque is produced.

	Free Rotation		**Mechanical Stall**	
Motor	**M1**	**M2**	**M1**	**M2**
$\boldsymbol{U_{in}}$ **[V]**	8.51	8.51	8.13	8.03
$\boldsymbol{I_{in}}$ **[A]**	0.292	0.176	1.14	1.38
$\boldsymbol{Q_M}$ **[mN.m]**	0	0	5.148	6.335
$\boldsymbol{n_M}$ **[RPM]**	8150	9250	0	0

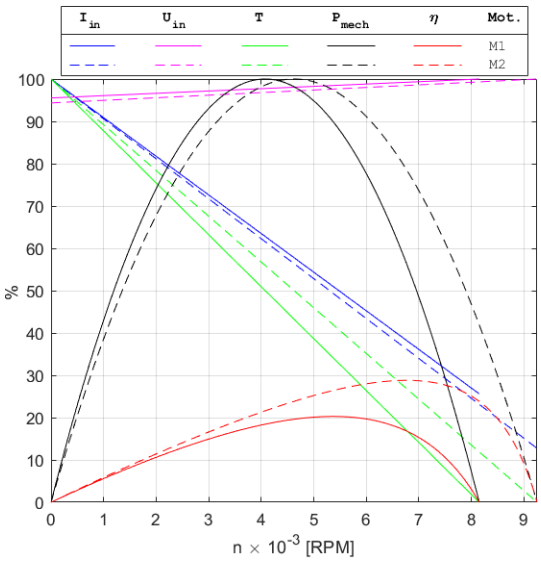

Figure 6.15: $\frac{I_{in}(n)}{I_{in}^{max}}$, $\frac{U_{in}(n)}{U_{in}^{max}}$, $\frac{Q_M(n)}{Q_M^{max}}$, P_{mech} and η_{elec} curves of the motors used.

Firstly, one observes from figure 6.15 that, despite being theoretically equal, the motors have different characteristics. The maximum output power is achieved at $n_M = 4000\,\mathrm{RPM}$ for M1 and at $n_M = 4600\,\mathrm{RPM}$ for M2. Regarding the motor efficiencies, one verifies that M1 has a maximum of approximately 20% achieved at $n_M = 5400\,\mathrm{RPM}$, whereas M2 has a maximum of 30% at $n_M = 6800\,\mathrm{RPM}$.

These efficiencies are particularly low, which may be justified by their small size. In fact, as the size of the motor/generator increases, it becomes more efficient [64]. Furthermore, as mentioned, one has no information about the amount of wear they have been subjected to. It may be significant to the point that the brushes are enough worn out to reduce the electric efficiency.

Finally, the low efficiency values may also be justified by a dynamic unbalance between the generator's axis and the turbine adaptor - the small scale of the motors did not allow a perfect alignment. In fact, this unbalance is visible and it is slightly larger in the motor M1, which may explain the difference in efficiency between both motors. Consequently, when operating, there are vibrations (these were audible during the measurements), which dissipate energy, further reducing the output power. Being a brushed motor/generator, this effect is even more critical, since there is a faster wearing of the brushes. Also, with the turbines mounted, the vibrations will be larger, since the mass is less concentrated near the axis, which means that maximum efficiencies will be even smaller than those estimated here.

6.3.2 Electrical Circuit

In order to estimate the amount of power that can be extracted from the wind using the generators and respective wind turbines mounted on the aircraft, one has to specify a closed electrical circuit, where the two generators are connected and a load consuming power exists.

Regarding the connection of the generators, these may be connected either in series or parallel. Since the goal of a *Drag-mode* AWE system is to send electricity down the tether to a ground station, high output voltages are preferable to minimize the transmission losses. Hence, a connection in series, which sums up the output voltages of each generator, is potentially better. However, as the wing is performing figures of eight, the generators may be subjected to different wind conditions, hence producing different powers. The difference may be such, that one generator starts operating as a motor, supplied by the power of the other generator, leaving none or very little output electric power [213]. Furthermore, if one generator has a malfunction, it breaks the circuit and no electric power is collected. Finally, as described in subsection 2.7.1.2 for *Drag-mode* systems, the take-off and landing maneuvers are performed using the generators as motors for throttle, and if one requires only a number of the motors to do so, it is not possible since their operation cannot be individualized.

Because of the aforementioned reasons, electric generators are, in general, connected in parallel. This means that the current produced by each is summed up and that they must have the same output voltage. If the generators are subjected to different wind conditions, this still must be verified, so, to equalize voltages and prevent electricity to flow from one generator to the other, electronic components such as bus-bars and rheostats are required, which increases the complexity of the circuit [216].

After connecting the generators between themselves, one must connect them further to a load which consumes the electric power produced. In AWE harvesting, this may be a direct connection to the grid or to any off-grid application (e.g. power supply of a household in a deserted area). In the present study, this will be a resistance which will dissipate the energy through heat and will allow to measure the output combined power.

6.3.2.1 Procedures to specify the Electrical Circuit

In order to determine the resistance which maximizes power, as well as which generator connection is most suitable for this testbed, one resorted to the wind tunnel to simulate the wind flow from which energy would be harvested in flight. As concluded in section 6.2.2, the aircraft should fly at an angle of attack of approximately 9^o in order to (almost) maximize power production. This means that the electric generators, for maximum power harvesting, would have to be mounted at an angle of -9^o with respect to the wind section chord, as sketched in figure 6.16. This way, the turbines would be perpendicular to the airflow. However, with the tools available (hand crafted), such was not possible - the generators are approximately aligned with the wing's leading edge, as seen on the detail on the right of figure 6.2. Furthermore, since this aircraft is not automated and there is no tether attached, one cannot precisely guarantee a given operational angle of attack.

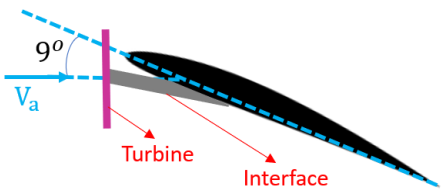

Figure 6.16: Sketch of the optimal alignment between the wing and turbine.

That being the case, the aircraft was positioned in the test section scale at an angle of attack of 0^o (even with the aerodynamic corrections, the "real" angle is very close to 0^o). Tests were performed with the wind tunnel's fan operating at 100%, i.e. producing an airflow with a speed of approximately $10\,\mathrm{m/s}$, at the test section. As discussed, the circuits in figure 6.17 were implemented and tested. When connecting the generators, one must consider that the attached turbines rotate in opposite directions so that the torques generated by each cancel out. Hence, the positive and negative terminals are opposite between generators and, thus, the connections must be done accordingly.

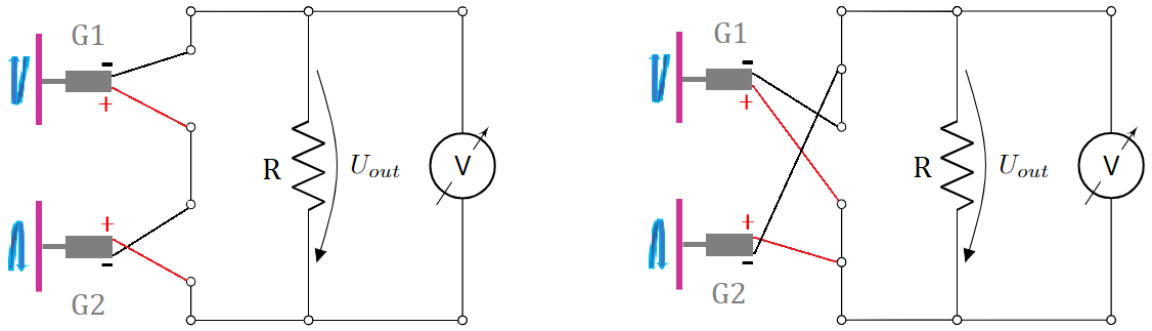

Figure 6.17: Left: Generators connected in series. Right: Generators connected in parallel.

Regarding the circuit resistance, a range from $5\,\Omega$ up to $120\,\Omega$ was covered. For each one, the voltage at its terminals (U_{out}) was measured using the previously mentioned multimeter (uncertainty of $\pm 0.001\,\mathrm{V}$). All the circuit components were connected using a breadboard. From the voltage measurements and applying Ohm's law ($P^{out}_{elec} = \frac{U^2_{Out}}{R}$), one obtained the output electrical power. The results are presented and discussed next.

6.3.2.2 Results and Discussion

In figures 6.18 and 6.19, one presents, for both electrical circuits, the $U_{out}(R)$ and $P^{out}_{elec}(R)$ tendency curves, respectively.

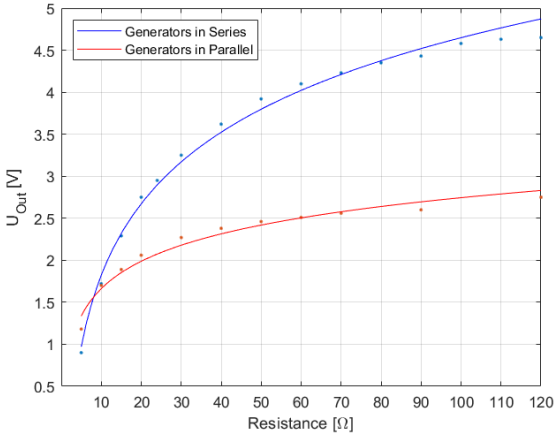

Figure 6.18: Variation of the output voltage with the circuit resistance, with the generators connected in series and in parallel.

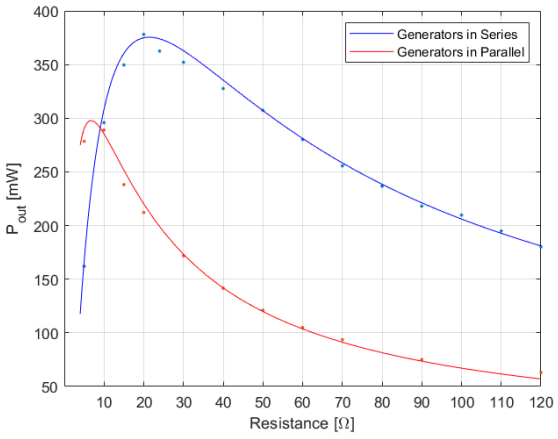

Figure 6.19: Variation of the output power with the circuit resistance, with the generators connected in series and in parallel.

As expected, the generators connected in series produce a larger output voltage. Theoretically, as $R \to \infty$, its values will tend to the double of the output voltage produced by the generators connected in parallel. This is not yet visible within the measurement's range.

Regarding the output power, in each circuit configuration, the maximum value is obtained with different circuit resistances, as expected. However, contrarily to the expectations, the maximum values are different. In fact, with the generators connected in series, the maximum output power was about $375\,\mathrm{mW}$, obtained with a resistance of $R = 20\,\Omega$, whereas with the generators connected in parallel, the maximum was about $300\,\mathrm{mW}$ with a resistance of $R = 5\,\Omega$.

In each test, both generators were operating under the same airflow conditions. However, as seen in subsection 6.3.1.2, they have different electrical efficiencies, which, in turn, means they have different output voltages. Contrarily to what was mentioned earlier in this section and following the same "low-electronics" philosophy as before, in the parallel configuration (see figure 6.17 on the right), it was not included any kind of electronic control to equalize the output voltages of the generators. Hence, as required, that voltage equalisation is being done "automatically" between the generators, which means there is an electric flow between the generators which does not contribute to the circuit's output power. With the generators connected in series, since they are subjected to the same input (meaning they both operate as generators), there is no similar effect, hence justifying the larger output power.

Summing up, at the light of the previous results and with the currently used electronics, one should connect the generators in series and use a resistance of $20\,\Omega$, for maximum power production. Even so, it is noteworthy to mention that this conclusion is only valid if the generators are operating in similar conditions. If not, as discussed for this configuration, there will be a decrease in the circuit's efficiency.

6.3.3 Aerodynamic Efficiency of the Wind Turbines

It is clear that the testbed is not optimized electronically and that several improvements must be done to increase the generation of electric power. However, to assess the potential of on-board generation with this testbed, one also has to quantify the aerodynamic efficiency of the wind turbines, which in the performed wind tunnel tests are operating just like conventional technology.

The input wind power of each turbine is given by:

$$P_w^G = \frac{1}{2}\,\rho_{air}\,A_{rot}\,V_{t\infty}^3 \tag{6.20}$$

where $\rho_{air} = 1.19\,\frac{\mathrm{kg}}{\mathrm{m}^3}$ and $V_{t\infty} = 10.2\,\mathrm{m/s}$, since the tests were performed in similar conditions as earlier (sec. 6.2.2); and $A_{rot} = \frac{0.152^2}{4}\,\pi = 0.01815\,\mathrm{m}^2$ is the turbine's rotor area.

When multiplying this power by the aerodynamic (η_{aero}^G) and electrical (η_{elec}^G) efficiencies of the generator, one obtains its output power, as follows:

$$P_{elec}^{out,G} = \eta_{aero}^G\,\eta_{elec}^G\,P_w^G \tag{6.21}$$

One considers that both generators, with their respective turbines and interfaces, are aerodynamically equal, thus having the same efficiency: $\eta_{aero}^{G1} = \eta_{aero}^{G2} = \eta_{aero}$.

By performing a simple analysis to the circuit on the left of figure 6.17, one verifies that $P_{elec}^{out} = P_{elec}^{out,G1} + P_{elec}^{out,G2}$, which means that:

$$P_{elec}^{out} = \eta_{aero}\,\left(\eta_{elec}^{G1} + \eta_{elec}^{G2}\right)\,P_w^G \iff \eta_{aero} = \frac{P_{elec}^{out}}{P_w^G} = \frac{2\,P_{elec}^{out}}{\rho_{air}\,A_{rot}\,V_{t\infty}^3\,\left(\eta_{elec}^{G1} + \eta_{elec}^{G2}\right)} \tag{6.22}$$

When performing the tests described in subsection 6.3.2.1, one measured the wind turbine's angular speed, using the previously mentioned tachometer (uncertainty of $\pm 1\mathrm{RPM}$). With an airflow speed of $V_{t\infty} = 10.2\,\mathrm{m/s}$, both generators were rotating at $n_{Rot} \approx 4000\,\mathrm{RPM}$, which, evidently, is independent from the circuit configuration and resistance value. At that angular speed, assuming the same efficiency as motors, one obtains, from figure 6.15, an electrical efficiency of 18% for generator G1 and 21% for generator G2.

Considering the maximum output power of the circuit with the generators connected in series (resistance of $R = 20\,\Omega$), i.e. $P_{elec}^{out} = 375\,\mathrm{mW}$, one obtains, using eq. (6.22), an aerodynamic efficiency of the turbines of $\eta_{aero} = 8.4\%$. Usually, optimized, large-scale wind turbine systems have an aerodynamic efficiency of $40 - 50\%$ (the theoretical Betz limit is 59%) [217], which is about five times higher than what was obtained in this study.

Firstly, this particularly low aerodynamic efficiency may be justified by the proximity of the wind turbines to the wing and fuselage, as observed in figure 6.2. The wing may produce a blockage effect on the turbine's wake, which reduces the amount of energy extracted. Regarding the proximity to the fuselage, the boundary layer that forms in its surface may disturb the airflow reaching the turbine, namely reducing its velocity, which consequently reduces the available energy for extraction. Although the wind turbines were positioned in sections which were originally thought for propelled motors (from factory), they might not be optimal for generators. Hence, an optimization study of the wind turbines position should be carried out in the future.

Then, one must not neglect the previously mentioned vibrations of the generators - see subsection 6.3.1.2. As pointed out, these are larger with the turbines mounted. Hence, the electrical efficiencies of the generators are expected to be lower than the ones used. Although it was not possible to quantify this reduction, it means the aerodynamic efficiency may be significantly larger than the one estimated here. These results confirm the need of using better electric generators in future endeavours.

6.4 Flight Testing

In order to further understand the potential of on-board power generation with the developed prototype, one also resorted to flight testing. Contrarily to wind tunnel testing, where the environment is controlled and the airflow is steady with a maximum velocity of approximately $10\,\mathrm{m/s}$, in these tests, the aircraft is subjected to a realistic scenario of operation. Particularly, it has to fly with larger velocities than tested, as depicted in figure 6.9 (section 6.2.2), in order to maintain a sustained flight and it has to perform a number of maneuvers, to follow a certain path, which introduce variability in the aircraft's attitude. Furthermore, it is subjected to real atmosphere conditions, namely a turbulent airflow, varying in space and time, as well as wind gusts.

All the aforementioned aspects impact on-board power production. Hence, the ultimate goal of flight testing was to verify how the aircraft and the wind turbines would behave and quantify the generation of electricity in a real scenario. Once more, it is important to mention that, at this stage, the flight operation is not AWE alike (no figure eights are possible) - there is no tether, thus it is not possible to fly in crosswind just like a kite. However, one may use some of the tested flight conditions to simulate AWE

harvesting, namely climbing and pitching flight as well as turns - as they take part of a figure eight path.

6.4.1 Testbed Setup

As presented, the testbed basis is a radio-controlled aircraft. For on-board power harvesting, two electric generators are connected in series, which provides power to a resistance, which, in turn, dissipates it by heat. Since the main goal of the testing is to quantify the power generated in flight, one has to register it for further analysis. Hence, one needs to add a voltage and current measure device to the previously mentioned circuit, as well as a data storing system. Usually, in flight tests, this is done using telemetry, since it allows ongoing performance monitoring and management. Although it is a very advantageous option, it would increase the system's electronics complexity at a stage when the currently used one still has to suffer maturation. Thereby, one decided to take a very simplistic approach, using a digital voltmeter/ammeter ("USB tester" [218]) and a small camera [219].

As sketched in figure 6.20, by connecting the tester in-between the generators (input) and the resistance (output), one can measure the generated voltage and current with uncertainties of $\pm 0.001\,\mathrm{V}$ and $\pm 0.001\,\mathrm{A}$, respectively. However, in order to the tester to turn on and operate continuously, a "feeding" voltage about $3.5\,\mathrm{V}$ (larger than the factory specifications) has to be provided. From figure 6.18, one verifies that, for the generators connected in series, operating at an airspeed of $10\,\mathrm{m/s}$, this voltage is achieved for a $40\,\Omega$ resistance, which does not correspond to the resistance that maximizes power output. Since several flight conditions were expected to be tested, some of which could be at similar airspeed as in the wind tunnel testing, and considering a safety margin, one decided to use a $50\,\Omega$ resistance in the circuit.

The previous device has no storing capabilities, hence one resorted to a camera [219] which would record the tester during the entire flight and store the video in a micro-usb card, for further measurement analysis. These components are very lightweight as well as small sized, however not enough to fit inside the fuselage. Hence, one had to mount them on the fuselage's nose, using hook-and-loop fastener tape, at the expense of a pressure drag increase. The electrical circuit is inside the fuselage. The final setup is showcased in figure 6.21.

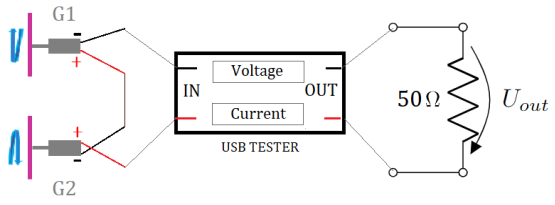

Figure 6.20: Schematic of the electrical circuit used on flight testing.

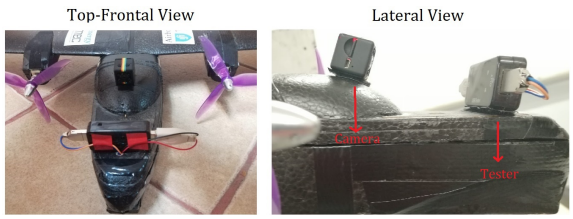

Figure 6.21: Setup of the camera and tester on the fuselage nose.

6.4.2 Obtain Relative Wind Speed In-flight

In order to assess the efficiency of power production, one requires the relative wind speed on the turbines. With that purpose, one may use the previously presented electrical circuit as an anemometer, by matching a generated output voltage to an airflow velocity on the turbines.

Accordingly, one resorted to the wind tunnel to generate airflows with speeds corresponding to the

whole fan operation range (0 - 100%). With the aircraft mounted on the scale's support with a 0^o angle of attack, the turbines only started rotating with the pump operating at 70%, which, after applying eq. (6.14) corresponded to a wind speed of about $7.3\,\mathrm{m/s}$ and a voltage of $2.35\,\mathrm{V}$. Up to 100%, one had to use the laboratory multimeter since the output voltage was to low for the tester to turn on with the lower wind speeds. At 100%, one compared the voltage measurement values of both multimeter and tester and verified that they were similar, hence no corrections to the previous measurements were necessary.

The measurements of voltage and dynamic pressure, which is then used to calculate the wind speed velocity from eq. (6.14), result in the curve of figure 6.22. With a *squared correlation factor* of 0.995, the tendency curve is represented by the following equation:

$$V_{t\infty}(U_{out}) = 1.7501\,U_{out} + 3.2978 \tag{6.23}$$

As mentioned, one expects to fly with relative wind speeds larger than $10\,\mathrm{m/s}$, thus producing voltages larger than $4\,\mathrm{V}$.

Therefore, in order to obtain the flight test wind speeds, one has to extrapolate equation (6.23). Hence, those wind speeds are only estimates.

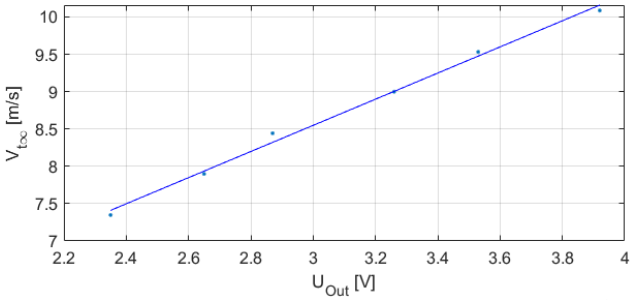

Figure 6.22: Tendency curve of the wind tunnel's airflow velocity over the testbed's electrical circuit output voltage.

6.4.3 Procedures for Flight Testing

Firstly, before every flight, one must confirm that the aircraft is balanced. When positioning the battery and other components, such as the *electronic speed controller* or the tester-camera setup, the center of gravity of the aircraft has to remain (approximately) in the original position to allow a stable flight.

Secondly, for take-off, in this aircraft, it is done by manually throwing it with a slight nose-up inclination, while providing full throttle to the motor. Then, it must climb until a desired altitude, from where it performs a controlled flight, either propelled or gliding.

Since several modifications were made, which increased the aircraft's weight, thus increasing the stall speed, and reduced its aerodynamic efficiency, as seen in section 6.2.2, then it was recommended to firstly fly the aircraft as close to the original version as possible, i.e. without the wind turbines, tester or camera, and understand its flight behaviour. This flight allowed the pilot to gain sensitivity on the control, by observing the in-flight response to the actuators. The aircraft showed a great response to the ailerons, which allowed quick banking and turning, although that is not recommended for the desired flight operation. However, one verified a weaker response to the elevators, mainly for a pitch-up maneuver, which was already hinted by the results in figure 6.8 (section 6.2.2).

Regarding flight testing to study on-board power generation, as mentioned, one intended to test a set of flight conditions which could be of interest for a future AWE implementation, in a realistic outside scenario. The flight test was taken in an open field area in *Cortegaça, Sintra* ($38.833978^oN, 9.325859^oW$), in a day of moderate wind speed conditions (for the aircraft's scale). At the time of flight (around $11\mathrm{am}$),

steady speeds of $7\,\mathrm{m/s}$ and gusts of $11\,\mathrm{m/s}$ were observed [220]. Although these wind speeds bring difficulties to obtain a controlled flight of a small-scale aircraft, it is when more energy is available for harvesting. Thereby, flying in such conditions approximates the test to a real operation scenario.

An illustrative testing path is shown in figure 6.23, and their flight conditions (FC), as recorded by on-ground video, are described next, while pointing similarities to AWE operation (figure 6.24). The approximate direction of the wind speed, at the time, is also represented on the figure. It is noteworthy that being a downwind (DW) or upwind (UW) maneuver is not relevant for that comparison, since an AWE system flies in crosswind. However, it affects the relative wind speed on the turbines, thus affecting power production.

- **UW/DW Climb**: The aircraft is launched against the wind and starts to climb - **FC1**. Then, turns and continues to climb downwind - **FC2**. This may be seen as the take-off climb in an AWE figure of eight maneuver (see (a) on 6.24), although there is no power production at this stage, or even as a part of the turn-climb maneuver (see (b) in fig. 6.24), since the wing's attitude is similar.
- **Turn**: The aircraft makes a turn (**FC3**) to reverse the flight sense, either from a downwind or from an upwind condition. Given the aircraft's attitude in this maneuver as well as the fact it flies in crosswind, this may correspond to a turn in an AWE figure of eight maneuver (see (b) in fig. 6.24).
- **UW/DW Horizontal Leveled Flight**: In the day of flight, the wind was very turbulent, which was observed by the rolling oscillations of the aircraft when trying to perform a steady leveled flight. This was specially clear when flying upwind (**FC4**). However, there were instances when a "quasi-steady" (QS) horizontal leveled flight could be performed. This happened both upwind (**FC5**) and downwind (**FC6**).
- **Aerodynamic Stall**: Due to a gust, the aircraft stalled (**FC7**), which was followed by a steep pitching motion.
- **Pitched Flight**: This flight condition (**FC8**) may correspond to one of the two typical pitching maneuvers in an AWE figure of eight (see (c) in fig. 6.24). It is when maximum power harvesting is expected, due to a largest apparent wind speed.
- **Gliding**: The motor was turned off, while downwind, and the gliding condition was tested (**FC9**).

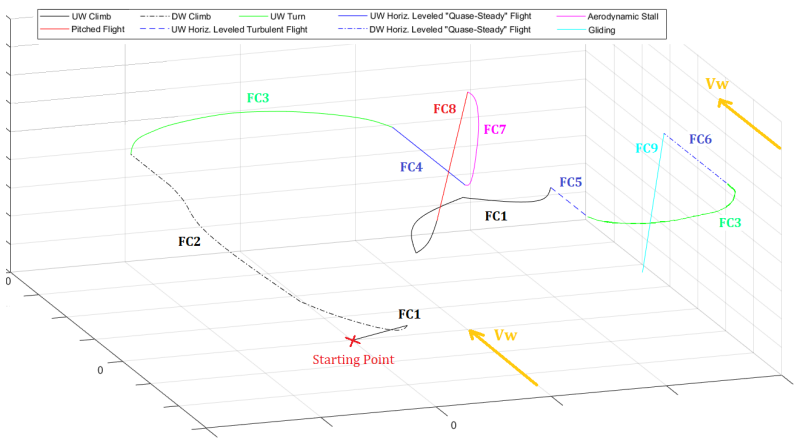

Figure 6.23: Representation of the flight test path and stages.

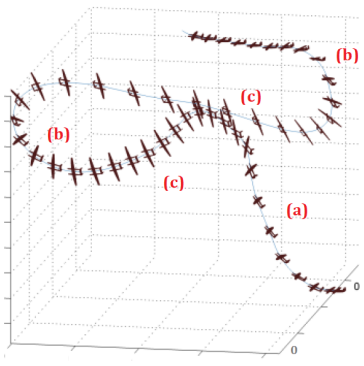

Figure 6.24: Representation of an AWE figure of eight [221].

6.4.4 Results and Discussion

After the flight, one analysed the video obtained by the on-board camera. Since the flight was also filmed, one could match the aforementioned stages to the values measured. The results are presented next in table 6.4, where the relative wind speed (apparent airflow velocity on the turbines, V_a) is estimated by equation (6.23). Video frames of the tester measurements are displayed in appendix C.

Firstly, one verifies that the testbed was subjected to larger airspeeds than in the wind tunnel, as expected, being the maximum around $18.63\,\mathrm{m/s}$, for the pitch maneuver (FC8).

Table 6.4: Apparent wind speed and output voltage, current and power of the electrical circuit, at different flight test conditions.

FC	$\boldsymbol{U_{out}}\,(\mathbf{V})$	$\boldsymbol{I_{out}}\,(\mathbf{A})$	$\boldsymbol{P_{out}}\,(\mathbf{mW})$	$\boldsymbol{V_a}\,(\mathbf{m/s})$
FC1	5.460	0.113	617	12.9
FC2	5.260	0.111	584	12.5
FC3	6.360	0.128	814	14.4
FC4	5.830	0.095	554	13.5
FC5	6.870	0.123	845	15.3
FC6	6.080	0.122	742	13.9
FC7	4.100	0.093	381	10.5
FC8	8.760	0.148	1297	18.6
FC9	4.120	0.093	383	10.5

Comparing the climbing flight conditions, one observes that there is only a 5.67% difference in the power produced. One would expect the difference to be larger, favouring the upwind maneuver (FC1). However, the reduced difference may be justified by the fact that FC1 followed the take-off, hence the aircraft did not have time to accelerate and increase the relative airspeed, whereas, in FC2, it already had a larger velocity, allowing to compensate the downwind condition.

Regarding the turning maneuvers (FC3), one verifies there is an increase in power produced. These turns are performed after long leveled (or almost) flight conditions, which allow the aircraft to increase velocity and subsequently allow turning with a higher centripetal acceleration. The aircraft already turns in crosswind, which means that, in an AWE operation, where the tether allows even a greater centripetal acceleration, the output power is expected to be larger than the $814\,\mathrm{mW}$ obtained.

Analysing the horizontal leveled flight conditions, one verifies the maximum output power was obtained in the ”quasi-steady” upwind condition (FC5), which is expected since that, in the DW condition (FC6), the relative airspeed is naturally smaller. Moreover, in FC4, the high airflow turbulence dissipates energy from the flow and reduces the turbine’s aerodynamic efficiency, leading to smaller power outputs.

Regarding the aerodynamic stall condition, one confirmed in flight it was smooth. Naturally, there is a significant decrease in airspeed, hence in the power output. A similar result was obtained in FC9. When the motor was turned-off, there was a fast decrease in the velocity, and the aircraft started pitching down, not gliding, which suggests the *gliding ratio* is too small. In fact, one verified, in the wind tunnel, a reduction of the modifier’s aircraft C_L/C_D (cf. fig. 6.10) to 8. Adding the turbines, but specially the tester and camera further worsen the testbed’s capability to glide. Evidently, in an AWE implementation, the setup will not include neither the tester nor the camera.

Finally, in FC8, which is the closest to AWE operation, as perceived in figure 6.24, one obtained the maximum output power in the whole flight test: $1.296\,\mathrm{W}$. This result alongside the result of FC3 hint for a good performance of this testbed in a figure eight operation, which confirms its potential for a future AWE implementation.

Chapter 7: Conclusions and Future Development Recommendations

Firstly, one invested in providing an extensive state-of-the-art review on AWE, mostly focusing on the operational and architectural level. The two main electricity generation principles, *Lift-mode* and *Drag-mode*, were presented, as well as their subsystems/components alternatives (wing types, tether and the take-off/landing systems). This profound study enhanced the specific identification of key-factors in AWE exploration, which were then categorized in class groups: Technical Design Factors, Operational Factors, Manufacturability, Logistics, and Social Acceptability Factors. The Technical Design Factors include the AWE system's Aerodynamic Performance, Mass-to-Area ratio, its Durability and its Survivability. The Operational Factors encompass the system's Continuity of Power Production, its Controlabiity, and Take-off and Landing Feasibility. The class of Manufacturability embodies everything related with the fabrication of the systems and the Logistics class concerns the logistical aspects of storing, transporting and installing the systems, Finally, Social Acceptability Factors are composed by Visual, Noise and Ecological Impact, and also Safety.

Then, in order to also identify the most propitious AWE systems, namely the most suitable for an AWE implementation in a on-shore rural or in a off-shore site, one resorted to a Multi-Criteria Decision Analysis, based on all the information collected and using the key-factors as criteria. The object of the analysis were nine existing AWE crosswind systems developed by companies/research institutions. The method used was the Fuzzy Analytic Network Process (FANP). The implemented methodology suggested that a rigid wing *Lift-mode* system with pumping-cycle operation mode and horizontal take-off as the most suitable solution for both investigated sites. However, despite being the clear preferential system for an off-shore location, in a rural site, *Drag-mode* systems also demonstrated to be to be suitable options. In addition, the methodology also revealed Aerodynamic Performance, Mass-to-Area Ratio and Controlability as the most relevant factors in the decision.

These results must be seen with some caution, since the performed analysis, though sustained, was mostly qualitative, by lack of comparable quantitative data between the systems. Although the FANP method takes into account the subjectivity inherent on this type of analysis, additional studies should be performed, when this kind of data is available.

Then, considering a potential AWE implementation, an investigation on the high-altitude wind resource in a region of Portugal was performed, using existing models of the wind speed and power vertical profiles, namely the "Log-Linear Law", and previously computed low-altitude wind speed data maps from NCEP/NCAR reanalysis. For high-altitude wind speed predictions, the importance of considering atmospheric stability conditions was specially acknowledged, so when considering a real implementation, a statistical study of these conditions on the potential exploration site should be performed for more precise wind speed and power predictions. For the studied region, one projected a maximum sustained

wind speed of $18\,\mathrm{m/s}$ at a height of $250\,\mathrm{m}$ in coastal areas, for stable atmospheric conditions. Moreover, by comparing the high-altitude wind resource in two rural on-shore and one off-shore locations, one concluded that harvesting AWE has more potential in on-shore locations.

Finally, aiming to initiate the first crosswind AWE system prototype in Portugal, an experimental testbed of a small-scale *Drag-mode* system was developed. Starting from a radio-controlled aircraft, two electric brushed generators were mounted on the wing. Resorting to wind tunnel testing, the testbed was aerodynamically characterized, thus obtaining a lift-to-drag ratio of 8.3, which is a very important quantity for AWE harvesting. Moreover, tests to determine an optimal generator-load resistance electrical circuit were performed: with the current components, a series connection of the generators and a circuit resistance of $20\,\Omega$ allow the maximum power output. At last, a flight test was performed to assess the potential of power production in a real scenario, while establishing a parallel with AWE operation. In a steep pitched flight condition, typical of AWE figure eights, the prototype produced a power of $1.3\,\mathrm{W}$ for an estimated relative wind speed of $18.6\,\mathrm{m/s}$, which shows good prospects.

In essence, foundations for AWE studying and exploration were settled, and although the developed testbed is a very non-optimized, small-scale system, considering the results obtained, it shows good potential for improvements, some of which are now pointed out:

- **Electronic Optimization**: The electric generators used are very electrically inefficient, either because they are brushed, old or suffer from vibrations. Hence, they should be substituted by brushless generators. Furthermore, as discussed, a parallel connection of the generators has more advantages, hence an optimization of the electronic circuit should be carried out.
- **Aircraft Instrumentation**: For a future AWE operation, an automated flight is an essential requirement. Hence, instrumenting the testbed to provide inputs to a flight controller (which has also to be designed alongside an optimal flight path) is necessary.
- **Include a Tether**: To dimension a tether, test it in the wind tunnel and include it in the testbed for AWE operation.
- **Turbines Aerodynamic Optimization**: A detailed study on which position the wind turbines should be mounted on the aircraft for optimal production, as well as their size, should be followed up.
- **System Scale-up**: After optimizing the small-scale prototype, it is relevant to do a parametric study on how scaling-up the system will affect the power generation, since, for example, it is known that the tether's drag negative impact becomes smaller or that larger generators are more efficient.

Bibliography

[1] Enerdata. Electricity domestic consumption. URL: https://rb.gy/uxcz9l. Visited: 21-03-2022.

[2] Enerdata. Total energy consumption. URL: https://rb.gy/kxsbv8. Visited: 15-03-2022.

[3] Enerdata. Total primary energy consumption. URL: https://rb.gy/taiw22. Visited: 15-03-2022.

[4] H. Ritchie and M. Roser. Energy. URL: https://rb.gy/xzrx9v. Visited: 15-03-2022.

[5] A. Markandya, D. Saygin, A. Miketa, D. Gielen, and N. Wagner. The true cost of fossil fuels: Saving on the externalities of air pollution and climate change. Technical report, International Renewable Energy Agency, May 2016. ISBN : 978-92-95111-87-5.

[6] U. N. C. Change. The paris agreement. URL: https://rb.gy/ozp6oy. Visited: 21-03-2022.

[7] R. Inglesi-Lotz. The impact of renewable energy consumption to economic growth: A panel data application. *Energy Economics*, 53:58–63, 2015, DOI: 10.1016/j.eneco.2015.01.003.

[8] C. Pappas, C. Karakosta, V. Marinakis, and J. Psarras. A comparison of electricity production technologies in terms of sustainable development. *Energy Conversion and Management*, 64: 626–632, 2012, DOI: 10.1016/j.enconman.2012.06.006.

[9] F. Asdrubali, G. Baldinelli, F. D'Alessandro, and F. Scrucca. Life cycle assessment of electricity production from renewable energies: Review and results harmonization. *Renewable and Sustainable Energy Reviews*, 42:1113–1122, 2014, DOI: 10.1016/j.rser.2014.10.082.

[10] P. Enevoldsen and M. Z. Jacobson. Data investigation of installed and output power densities of onshore and offshore wind turbines worldwide. *Energy for Sustainable Development*, 60:40–51, 2020, DOI: 10.1016/j.esd.2020.11.004.

[11] C. L. Archer and K. Caldeira. Global assessment of high-altitude wind power. *Energies*, 2(2): 307–319, 2009, DOI: 10.3390/en20200307.

[12] P. Bechtle, M. Schelbergen, R. Schmehl, U. Zillmann, and S. Watson. Airborne wind energy resource analysis. *Renewable Energy*, 141:1103–1116, Apr. 2019, DOI: 10.1016/j.renene.2019.03.118.

[13] K. Marvel, K. Caldeira, and B. Kravitz. Geophysical limits to global wind power. *Nature Climate Change*, 2013, DOI: 10.1038/nclimate1683.

[14] Meet the haliade-x - powering 16,000 homes. URL: https://rb.gy/zdfn5u. Visited: 21-03-2022.

[15] T. Burton, N. Jenkins, D. Sharpe, and E. Bossanyi. *Wind Energy Handbook*. John Wiley & Sons, 2nd edition, 2011. ISBN 978-0-470-69975-1.

[16] M. L. Loyd. Crosswind kite power. *Journal of Energy*, 4(3), 1980, DOI: 10.2514/3.48021.

[17] Z. Khan and M. Rehan. Harnessing airborne wind energy: Prospects and challenges. *Journal of Control, Automation and Electrical Systems*, 27:728–740, July 2016, DOI: 10.1007/s40313-016-0258-y.

[18] U. Fechner and R. Schmehl. Model-based efficiency analysis of wind power conversion by a pumping kite power system. In U. Ahrens, M. Diehl, and R. Schmehl, editors, *Airborne Wind Energy*, chapter 14, pp. 248–269. Green Energy Technology. Springer, 1st edition, 2014.

[19] Airborne wind energy takes off in the caribbean with kitepower. URL: https://rb.gy/xxo5hb. Visited: 22-03-2022.

[20] Kite power for mauritius. URL: https://rb.gy/pntg0w. Visited: 22-03-2022.

[21] E. Lunney, M. Ban, N. Duic, and A. Foley. A state-of-the-art review and feasibility analysis of high altitude wind power in northern ireland. *Renewable and Sustainable Energy Reviews*, 68: 899–911, Aug. 2016, DOI: 10.1016/j.rser.2016.08.014.

[22] A. K. S. Mendonça, C. R. Vaz, A. G. R. Lezana, C. A. Anacleto, and E. P. Paladini. Comparing patent and scientific literature in airborne wind energy. *Sustainability*, 9(915), May 2017, DOI: 10.3390/su9060915.

[23] Electricity generation by energy sources in mainland portugal in 2022. URL: https://rb.gy/h3iuyc. Visited: 22-03-2022.

[24] Portugal. URL: https://rb.gy/h4w92o. Visited: 22-03-2022.

[25] A. Pacheco, E. Gorbeña, C. Sequeira, and S. Jerez. An evaluation of offshore wind power production by floatable systems: A case study from sw portugal. *Energy*, 131:239–250, May 2017, DOI: 10.1016/j.energy.2017.04.149.

[26] G. van de Kaa and L. Kamp. Exploring design dominance in early stages of the dominance process: The case of airborne wind energy. *Journal of Cleaner Production*, 321, 2021, DOI: 10.1016/j.jclepro.2021.128918.

[27] Makani harnessing wind energy with kites to create renewable electricity. URL: https://rb.gy/c3yamt. Visited: 23-03-2022.

[28] Kitekraft airborne wind energy. URL: https://rb.gy/ssbxc2. Visited: 23-03-2022.

[29] Windlift airborne power generators. URL: https://rb.gy/rbpowr. Visited: 23-03-2022.

[30] Ampyx power airborne wind energy. URL: https://rb.gy/cjyybc. Visited: 23-03-2022.

[31] Kitemill. URL: https://rb.gy/ris0ah. Visited: 23-03-2022.

[32] Twingtec energy 2.0 wind energy drones. URL: https://rb.gy/1h70jz. Visited: 23-03-2022.

[33] Skysails power airborne wind. URL: https://rb.gy/vzgoyr. Visited: 23-03-2022.

[34] Kitegen stem. URL: https://rb.gy/6mfyoq. Visited: 23-03-2022.

[35] Skypull wind for energy get the power from high altitude winds. URL: https://rb.gy/utzwhn. Visited: 23-03-2022.

[36] Enerkite airborne wind energy. URL: https://enerkite.de/en/. Visited: 23-03-2022.

[37] Kitenrg. URL: https://rb.gy/bwffuh. Visited: 23-03-2022.

[38] ewind airborne technology. URL: https://www.ewindsolutions.com/. Visited: 23-03-2022.

[39] Kitepower. URL: https://rb.gy/tlgziw. Visited: 23-03-2022.

[40] Kitegen research carousel. URL: https://rb.gy/dgud7v. Visited: 23-03-2022.

[41] X-wind energy without regret. URL: https://www.x-wind.de/. Visited: 23-03-2022.

[42] M. Diehl. Airborne wind energy: Basic concepts and physical foundations. In U. Ahrens, M. Diehl, and R. Schmehl, editors, *Airborne Wind Energy*, chapter 1, pp. 3–22. Green Energy Technology. Springer, 1st edition, 2014, DOI: 10.1007/978-3-642-39965-7_1.

[43] A. Cherubini, A. Papini, R. Vertechy, and M. Fontana. Airborne wind energy systems: A review of the technologies. *Renewable and Sustainable Energy Reviews*, 51:1461–1476, 2015, DOI: 10.1016/j.rser.2015.07.053.

[44] V. de Brederode. *Incompressible Aerodynamics: Fundamentals* (in Portuguese). IST Press, Instituto Superior Técnico, Lisboa, 2nd edition, July 2018. ISBN 9789898481320.

[45] I. Argatov, P. Rautakorpi, and R. Silvennoinen. Estimation of the mechanical energy output of the kite wind generator. *Renewable Energy*, 34:1525–1532, Jan. 2009, DOI: 10.1016/j.renene.2008.11.001.

[46] I. Argatov, P. Rautakorpi, and R. Silvennoinen. Apparent wind load effects on the tether of a kite power generator. *Journal of Wind Engineering and Industrial Aerodynamics*, 2011, DOI: 10.1016/j.jweia.2011.07.010.

[47] M. D. Lellis, R. Reginatto, R. Saraiva, and A. Trofino. The betz limit applied to airborne wind energy. *Renewable Energy An International Journal*, 2018, DOI: 10.1016/j.renene.2018.04.034.

[48] R. E. Wilson and P. B. S. Lissaman. *Applied Aerodynamics of Wind Power Machines*. Oregon State University, Corvallis (USA), July 1974.

[49] V. Okulov and G. A. M. van Kuik. The betz-joukowsky limit for the maximum power coefficient of wind turbines in Russian. *International Scientific Journal for Alternative Energy and Ecology*, 1(6): 106–111, 2009. URL: `https://findit.dtu.dk/en/catalog/537f0fac74bed2fd21002753`.

[50] C. L. Archer. An introduction to meteorology for airborne wind energy. In U. Ahrens, M. Diehl, and R. Schmehl, editors, *Airborne Wind Energy*, chapter 5, pp. 81–94. Green Energy Technology. Springer, 1st edition, 2014, DOI: 10.1007/978-3-642-39965-7_5.

[51] S. Costello, C. Costello, G. Francois, and D. Bonvin. Analysis of the maximum efficiency of kite-power systems. *Journal of Renewable and Sustainable Energy*, 7(5), 2015, DOI: 10.1063/1.4931111.

[52] F. Bauer, C. M. Hackl, K. Smedley, and R. M. Kennel. Crosswind kite power with tower. In R. Schmehl, editor, *Airborne Wind Energy: Advances in Technological Development and Research*, chapter 18, pp. 441–462. Green Energy Technology. Springer, 1st edition, 2018, DOI: 10.1007/978-981-10-1947-0_18.

[53] M. Zolfaghari, F. Azarsina, and A. Kani. Feasibility analysis of airborne wind energy systems (awes) pumping kite (pk). *Journal of Advanced Research in Fluid Mechanics and Thermal Sciences*, 2020, DOI: 10.37934/arfmts.74.1.133143.

[54] P. Faggiani, R. Schmehl, and R. van der Vlugt. Pumping kites wind farm. Master's thesis, Delft University of Technology, The Netherlands, Dec. 2014.

[55] G. Licitra, J. Koenemann, A. Bürger, P. Williams, R. Ruiterkamp, and M. Diehl. Performance assessment of a rigid wing airborne wind energy pumping system. *Energy*, 173:569–585, Feb. 2019, DOI: 10.1016/j.energy.2019.02.064.

[56] R. H. Luchsinger. Pumping cycle kite power. In U. Ahrens, M. Diehl, and R. Schmehl, editors, *Airborne Wind Energy*, chapter 3, pp. 47–64. Green Energy Technology. Springer, 1st edition, 2014, DOI: 10.1007/978-3-642-39965-7_3.

[57] R. van der Vlugt, J. Peschel, and R. Schmehl. Design and experimental characterization of a pumping kite power system. In U. Ahrens, M. Diehl, and R. Schmehl, editors, *Airborne Wind Energy*, chapter 23, pp. 403–425. Green Energy Technology. Springer, 1st edition, 2014, DOI: 10.1007/978-3-642-39965-7_23.

[58] F. Fritz. Application of an automated kite system for ship propulsion and power generation. In U. Ahrens, M. Diehl, and R. Schmehl, editors, *Airborne Wind Energy*, chapter 20, pp. 359–372. Green Energy Technology. Springer, 1st edition, 2014, DOI: 10.1007/978-3-642-39965-7_20.

[59] F. Trevisi, M. Gaunaa, and M. William. Unified engineering crosswind models for the performance and cost of ground-gen and fly-gen crosswind airborne wind energy systems. *Renewable Energy*, 162:893–907, Aug. Feb., DOI: 10.1016/j.renene.2020.07.129.

[60] R. Schmehl, M. Noom, and R. van der Vlugt. Traction power generation with tethered wings. In U. Ahrens, M. Diehl, and R. Schmehl, editors, *Airborne Wind Energy*, chapter 2, pp. 23–45. Green Energy Technology. Springer, 1st edition, 2014, DOI: 10.1007/978-3-642-39965-7_2.

[61] P. Williams, B. Lansdorp, and W. Ockels. Optimal crosswind towing and power generation with tethered kites. *Journal of Guidance, Control and Dynamics*, 31, Feb. 2008, DOI: 10.2514/1.30089.

[62] J. Stuyts, G. Horn, W. Vandermeulen, J. Driesen, and M. Diehl. Effect of the electrical energy conversion on optimal cycles for pumping airborne wind energy. *IEEE Transactions on Sustainable Energy*, 6(1):2–10, Jan. 2015, DOI: 10.1109/TSTE.2014.2349071.

[63] I. Argatov and R. Silvennoinen. Efficiency of traction power conversion based on crosswind motion. In U. Ahrens, M. Diehl, and R. Schmehl, editors, *Airborne Wind Energy*, chapter 4, pp. 65–79. Green Energy Technology. Springer, 1st edition, 2014, DOI: 10.1007/978-3-642-39965-7_4.

[64] F. Torabi. Chapter 2 - wind properties and power generation. In F. Torabi, editor, *Fundamentals of Wind Farm Aerodynamic Layout Design*, Wind Energy Engineering, pp. 25–75. Academic Press, 2022. ISBN 978-0-12-823016-9, DOI: 10.1016/B978-0-12-823016-9.00008-5.

[65] U. Fechner and R. Schmehl. Model-based efficiency analysis of wind power conversion by a pumping kite power system. In U. Ahrens, M. Diehl, and R. Schmehl, editors, *Airborne Wind Energy*, chapter Jan., pp. 248–269. Green Energy Technology. Springer, 1st edition, 2014, DOI: 10.1007/978-3-642-39965-7_14.

[66] L. Fagiano, M. Milanese, and D. Piga. High-altitude wind power generation. *IEEE Transactions on Energy Conversion*, 25(1):168–180, 3 2010, DOI: 10.1109/TEC.2009.2032582.

[67] L. Goldstein. Airborne wind energy conversion systems with ultra high speed mechanical power transfer. In U. Ahrens, M. Diehl, and R. Schmehl, editors, *Airborne Wind Energy*, chapter 13, pp. 235–247. Green Energy Technology. Springer, 1st edition, 2014, DOI: 10.1007/978-3-642-39965-7_13.

[68] L. Goldstein. Theoretical analysis of an airborne wind energy conversion system with a ground generator and fast motion transfer. *Energy*, 55:987–995, May 2013, DOI: 10.1016/j.energy.2013.03.087.

[69] B. Houska and M. Diehl. Optimal control for power generating kites. In *2007 European Control Conference (ECC)*, pp. 3560–3567, 2007, DOI: 10.23919/ECC.2007.7068861.

[70] M. Diehl, B. Houska, and A. Ilzhöfer. Nonlinear mpc of kites under varying wind conditions for a new class of large-scale wind power generators. *International Journal of Robust and Nonlinear Control*, 17:1590 – 1599, Apr. 2007, DOI: 10.1002/rnc.1210.

[71] M. Diehl, L. Magni, and G. D. Nicolao. Efficient nmpc of unstable periodic systems using approximate infinite horizon closed loop costing. *Annual Reviews in Control*, 28(1):37–45, Jan. 2004, DOI: 10.1016/j.arcontrol.2004.01.011.

[72] M. Diehl, I. Uslu, R. Findeisen, S. Schwarzkopf, F. Allgöwer, H. G. Bock, T. Burner, E. D. Gilles, A. Kienle, and J. P. Schlöder. Real-time optimization for large scale processes: Nonlinear model predictive control of a high purity distillation column. In *Online Optimization of Large Scale System*, pp. 363–383, 2001, DOI: 10.1007/978-3-662-04331-8_20.

[73] M. Canale, L. Fagiano, M. Milanese, and M. Ippolito. Kitegen project: control as key technology for a quantum leap in wind energy generators. In *2007 American Control Conference*, pp. 3522–3528, 2007, DOI: 10.1109/ACC.2007.4282697.

[74] U.S. Pat. No. Vertical axis wind turbine with control system steering kites (Sequoia Automation S.R.L, Ippolito, Massimo,).

[75] M. Canale, L. Fagiano, and M. Milanese. Power kites for wind energy generation [applications of control]. *IEEE Control Systems Magazine*, 27(6):25–38, 2007, DOI: 10.1109/MCS.2007.909465.

[76] L. Fagiano. *Control of Tethered Airfoils for High–AltitudeWind Energy Generation*. PhD thesis, Politecnico di Torino, 2009.

[77] U. Ahrens, B. Pieper, and C. Töpfer. Combining kites and rail technology into a traction-based airborne wind energy plant. In U. Ahrens, M. Diehl, and R. Schmehl, editors, *Airborne Wind Energy*, chapter 25, pp. 437–441. Green Energy Technology. Springer, 1st edition, 2014, DOI: 10.1007/978-3-642-39965-7_25.

[78] L. Fagiano, M. Milanese, and D. Piga. Optimization of airborne wind energy generators. *International Journal of Robust and Nonlinear Control*, 22(18):2055–2083, 2012, DOI: 10.1002/rnc.1808.

[79] D. V. Lind. Analysis and flight test validation of high performance airborne wind turbines. In U. Ahrens, M. Diehl, and R. Schmehl, editors, *Airborne Wind Energy*, chapter 28, pp. 472–490. Green Energy Technology. Springer, 1st edition, 2014, DOI: 10.1007/978-3-642-39965-7_28.

[80] J. Mehr, E. J. Alvarez, and A. Ning. Unsteady aerodynamic analysis of wind harvesting aircraft. Technical Report 4054, Brigham Young University, Utah, United States, 2020.

[81] M. Zanon, S. Gros, J. Andersson, and M. Diehl. Airborne wind energy based on dual airfoils. *IEEE Transactions on Control Systems Technology*, 21(4), July 2013, DOI: 10.1109/TCST.2013.2257781.

[82] G. Lütsch. Airborne wind energy network hwn500 - shouldering r&d in co-operations. URL: `https://rb.gy/hdshyn`.

[83] W. Schmidt and W. Anderson. Kites: Pioneers of atmospheric research. In U. Ahrens, M. Diehl, and R. Schmehl, editors, *Airborne Wind Energy*, chapter 6, pp. 95–116. Green Energy Technology. Springer, 1st edition, 2014, DOI: 10.1007/978-3-642-39965-7_6.

[84] R. Luchsinger, D. Aregger, F. Bezard, D. Costa, C. Galliot, F. Gohl, J. Heilmann, H. Hesse, C. Houle, T. A. Wood, and R. S. Smith. Pumping cycle kite power with twings. In R. Schmehl, editor, *Airborne Wind Energy: Advances in Technology Development and Research*, chapter 24, pp. 603–621. Green Energy Technology. Springer, 1st edition, 2018, DOI: 10.1007/978-981-10-1947-0_24.

[85] R. Paelinck. High-performance soft kite technology state of the art, limits and opportunities. URL: `https://rb.gy/dserc2`.

[86] R. F. Verheul, J. Breukels, and W. J. Ockels. Material selection and joining methods for the purpose of a high-altitude inflatable kite. In s.n., editor, *AIAA conference proceedings*, pp. 1–13, United States, 2009. American Institute of Aeronautics and Astronautics Inc. (AIAA).

[87] A. Viré, P. Demkowicz, M. Folkersma, A. Roullier, and R. Schmehl. Reynolds-averaged Navier-Stokes simulations of the flow past a leading edge inflatable wing for airborne wind energy applications. *Journal of Physics: Conference Series*, 1618, 2020, DOI: 10.1088/1742-6596/1618/3/032007.

[88] S. Sachdeva. Impact of turning induced shape deformations on aerodynamic performance of leading edge inflatable kites: Master thesis. Master's thesis, Delft University of Technology, The Netherlands, 08 2017.

[89] H. Bosch. Finite element analysis of a kite for power generation: Computational modelling of flight dynamics of a tethered wing including non-linear fluid-structure interaction. Master's thesis, Delft University of Technology, The Netherlands, 04 2012.

[90] R. Leloup, K. Roncin, G. Bles, J.-B. Leroux, C. Jochum, and Y. Parlier. Estimation of the lift-to-drag ratio using the lifting line method: Application to a leading edge inflatable kite. In U. Ahrens, M. Diehl, and R. Schmehl, editors, *Airborne Wind Energy*, chapter 19, pp. 339–355. Green Energy Technology. Springer, 1st edition, 2014, DOI: 10.1007/978-3-642-39965-7_19.

[91] Kite design basics. https://rb.gy/gtl9bv. Visited: 25-03-2022.

[92] A. Bosch, R. Schmehl, P. Tiso, and D. Rixen. Dynamic nonlinear aeroelastic model of a kite for power generation. *Journal of Guidance, Control, and Dynamics*, Sep. 2014, DOI: 10.2514/1.G000545.

[93] M. Folkersma, R. Schmehl, and A. Viré. Boundary layer transition modelling on leading edge inflatable kite airfoils. *Wind Energy*, 22:908–921, Feb. 2019, DOI: 10.1002/we.2329.

[94] B. Franca. A tool for aerodynamic analysis of flexible kites: A mems sensor implementation. Master's thesis, Delft University of Technology, The Netherlands, 06 2014.

[95] R. H. M. van Kappel. Aerodynamic analysis tool for dynamic leading edge inflated kite models. Master's thesis, Delft University of Technology, The Netherlands, Oct. 2012.

[96] R. J. Coenen. Single skin kite airfoil optimization for awes. Master's thesis, Delft University of Technology, The Netherlands, Dec. 2018.

[97] J. Breukels, R. Schmehl, and W. Ockels. Aeroelastic simulation of flexible membrane wings based on multibody system dynamics. In U. Ahrens, M. Diehl, and R. Schmehl, editors, *Airborne Wind Energy*, chapter 16, pp. 287–305. Green Energy Technology. Springer, 1st edition, 2014, DOI: 10.1007/978-3-642-39965-7_16.

[98] J. Oehler and R. Schmehl. Aerodynamic characterization of a soft kite by in situ flow measurement. *Wind Energy*, 4:1–21, Dec. 2018, DOI: 10.5194/wes-4-1-2019.

[99] A. Viré, G. Lebesque, M. Folkersma, and R. Schmehl. Effect of chordwise struts and misaligned flow on the aerodynamic performance of a leading-edge inflatable wing. *Energies*, 15, 02 2022, DOI: 10.3390/en15041450.

[100] S. Dunker. Ram-air wing design considerations for airborne wind energy. In U. Ahrens, M. Diehl, and R. Schmehl, editors, *Airborne Wind Energy*, chapter 31, pp. 517–546. Green Energy Technology. Springer, 1st edition, 2014, DOI: 10.1007/978-3-642-39965-7_31.

[101] D. Pantua. Flugwindkraftanlage mit drachen von bis zu 120 m² besteht tests. URL: https://www.contextcrew.de/flugwindkraftanlage-mit-drachen-von-bis-zu-120-m%C2%B2-besteht-tests/. Visited: 25-03-2022.

[102] A. de Wachter. Deformation and aerodynamic performance of a ram-air wing. Master's thesis, Delft University of Technology, The Netherlands, Sep. 2008.

[103] P. Thedens, G. de Oliveira, and R. Schmehl. Ram-air kite airfoil and reinforcements optimization for airborne wind energy applications. *Wind Energy*, 22:653–665, May 2019, DOI: 10.1002/we.2313.

[104] N. J. Adam. Computational simulation of fluid-structure interaction of soft kites. Master's thesis, Delft University of Technology, The Netherlands, Nov. 2018.

[105] M. Folkersma, R. Schmehl, and A. Viré. Steady-state aeroelasticity of a ram-air wing for airborne wind energy applications. *Journal of Physics Conference Series*, 1618, Sep. 2020, DOI: 10.1088/1742-6596/1618/3/032018.

[106] S. Schnez. Take-off & landing - a challenge for lift-based, rigid wing awe systems.

[107] E. J. Kroon. Airborne wind energy airfoils: Design of pareto-optimal airfoils for rigid wing systems in the field of airborne wind energy. Master's thesis, Delft University of Technology, The Netherlands, Oct. 2018.

[108] K. Vimalakanthan, M. Caboni, J. G. Schepers, E. Pechenik, and P.Williams. Aerodynamic analysis of ampyx's airborne wind energy system. *Journal of Physics: Conference Series*, 1037, 2018, DOI: 10.1088/1742-6596/1037/6/062008.

[109] Materials & processes: Fibers for composites. `https://rb.gy/mg5dpy`. Visited: 25-03-2022.

[110] A. A. Candade, M. Ranneberg, and R. Schmehl. Structural analysis and optimization of a tethered swept wing for airborne wind energy generation. *Wind Energy*, 23:1006–1025, Dec. 2019, DOI: 10.1002/we.2469.

[111] U. Fasel, D. Keidel, G. Molinari, and P. Ermanni. Aerostructural optimization of a morphing wing for airborne wind energy applications. *Smart Materials and Structures*, 26(9), Aug. 2017, DOI: 10.1088/1361-665X/aa7c87.

[112] J. Breukels and W. Ockels. Design of a large inflatable kiteplane. In s.n., editor, *AIAA conference proceedings*, pp. 1–13, United States, 2007. American Institute of Aeronautics and Astronautics Inc. (AIAA), DOI: 10.2514/6.2007-2246.

[113] E. J. Terink, J. Breukels, R. Schmehl, and W. J. Ockels. Flight dynamics and stability of a tethered inflatable kiteplane. *Journal of Aircraft*, 48(2):503–513, Mar. 2011, DOI: 10.2514/1.C031108.

[114] J. Breuner and R. Luchsinger. Inflatable kites using the concept of tensairity. *Aerospace Science and Technology*, pp. 557–563, Apr. 2010, DOI: 10.1016/j.ast.2010.04.009.

[115] Kitegen power wing. `http://www.kitegen.com/en/2014/09/12/kitegen-power-wing/`. Visited: 26-03-2022.

[116] G. Maneia, C. Tribuzi, D. Tordella, and M. Iovieno. Aerodynamics of a rigid curved kite wing. *Renewable Energy*, June 2013.

[117] R. Bosman, V. Reid, M. Vlasblom, and P. Smeets. Airborne wind energy tethers with high-modulus polyethylene fibers. In U. Ahrens, M. Diehl, and R. Schmehl, editors, *Airborne Wind Energy*, chapter 33, pp. 563–585. Green Energy Technology. Springer, 1st edition, 2014, DOI: 10.1007/978-3-642-39965-7_33.

[118] Hmpe/dyneema® ropes stronger than steel! `https://rb.gy/90griu`. Visited: 24-03-2022.

[119] F. Trevisi, M. Gaunaa, and M. McWilliam. The influence of tether sag on airborne wind energy generation. *Journal of Physics Conference Series*, 1618, Sep. 2020, DOI: 10.1088/1742-6596/1618/3/032006.

[120] D. Eijkelhof, S. Rapp, U. Fasel, M. Gaunaa, and R. Schmehl. Reference design and simulation framework of a multi-megawatt airborne wind energy system. *Journal of Physics Conference Series*, 1618, Oct. 2020, DOI: 10.1088/1742-6596/1618/3/032020.

[121] I. Argatov, P. Rautakorpi, and R. Silvennoinen. Apparent wind load effects on the tether of a kite power generator. *Journal of Wind Engineering and Industrial Aerodynamics*, 99:1079–1088, Aug. 2011, DOI: 10.1016/j.jweia.2011.07.01.

[122] S. Dunker. Tether and bridle line drag in airborne wind energy applications. In R. Schmehl, editor, *Airborne Wind Energy: Advances in Technology Development and Research*, chapter 2, pp. 29–56. Green Energy Technology. Springer, 1st edition, 2018, DOI: 10.1007/978-981-10-1947-0_2.

[123] U.S. Pat. No. Faired tether for wind power generation systems (Griffith, Saul and Lynn, Peter and Montague, Don and Hardham, Corwin,).

[124] M. Sommerfeld, J. D. Schutter, M. Dörenkämper, and C. Crawford. Ground-generation airborne wind energy design space exploration [preprint]. *Wind Energ. Sci. Discuss.*, 2020, DOI: 10.5194/wes-2020-123.

[125] Y. Ji and J. He. Analysis on lightning triggering possibility along transmission tethers of high altitude wind energy exploitation system. *Electric Power Systems Research*, 94:16–23, June 2012, DOI: 10.1016/j.epsr.2012.05.021.

[126] E. Bontekoe. Up! how to launch and retrieve a tethered aircraft. Master's thesis, Delft University of Technology, The Netherlands, Aug. 2010.

[127] M. R. Doyle, D. J. Samuel, T. Conway, and R. R. Klimowski. Electromagnetic aircraft launch system-emals. *IEEE Transactions on Magnetics*, 31(1):528–533, 1995, DOI: 10.1109/20.364638.

[128] A. Power. Landing deck with rotation system being readied for manufacturing. `https://rb.gy/fqj7bh`. Visited: 26-03-2022.

[129] L. Fagiano, E. Nguyen-Van, F. Rager, S. Schnez, and C. Ohler. A small-scale prototype to study the takeoff of tethered rigid aircrafts for airborne wind energy. *IEEE/ASME Transactions on Mechatronics*, 22(4):1869–1880, 2017, DOI: 10.1109/TMECH.2017.2698405.

[130] L. Fagiano, E. Nguyen-Van, F. Rager, S. Schnez, and C. Ohler. Autonomous take-off and flight of a tethered aircraft for airborne wind energy. *IEEE Transactions on Control systems Technology*, 99:1–16, Feb. 2017, DOI: 10.1109/TCST.2017.2661825.

[131] M. Kruijff. Preparing for a commercially viable awe system in the utility sector. URL: `https://rb.gy/dibupw`.

[132] M. A. Rushdi, A. A. Hussein, T. Dief, S. Yoshida, and R. Schmehl. Simulation of the transition phase for an optimally-controlled tethered vtol rigid aircraft for airbornewind energy generation. In *AIAA Scitech 2020 Forum*, Jan. 2020, DOI: 10.2514/6.2020-1243.

[133] H. Fuest, D. F. Duda, T. Islam, T. Ostermann, and D. Moormann. Stabilization of the vertical take-off of a rigid flying wing for an airborne wind energy system. *CEAS Aeronautical Journal*, 12: 895–906, Sep. 2021, DOI: 10.1007/s13272-021-00545-3.

[134] K. Geebelen, M. Vukov, A. Wagner, H. Ahmad, M. Zanon, S. Gros, D. Vandepitte, J. Swevers, and M. Diehl. An experimental test setup for advanced estimation and control of an airborne wind energy system. In U. Ahrens, M. Diehl, and R. Schmehl, editors, *Airborne Wind Energy*, chapter 27, pp. 459–471. Green Energy Technology. Springer, 1st edition, 2014, DOI: 10.1007/978-3-642-39965-7_27.

[135] M. Clinckemaillie. An experimental set-up for energy generation using balanced kites. Master's thesis, K. U. Leuven, Belgium, 2012.

[136] M. A. Rushdi, A. A. Hussein, T. Dief, S. Yoshida, and R. Schmehl. Rotational start-up of tethered airplanes based on nonlinear mpc and mhe. In *Control Conference (ECC), 2013 European*, July 2013, DOI: 10.23919/ECC.2013.6669743.

[137] J. Koenemann, P. Williams, S. Sieberling, and M. Diehl. Modeling of an airborne wind energy system with a flexible tether model for the optimization of landing trajectories. *IFAC-PapersOnLine*, 50(1):11944–11950, Sep. 2017, DOI: 10.1016/j.ifacol.2017.08.1037.

[138] F. Bauer, C. M. Hackl, K. Smedley, and R. M. Kennel. Multicopter-based launching and landing of lift power kites. In R. Schmehl, editor, *Airborne Wind Energy: Advances in Technological Development and Research*, chapter 19, pp. 463–489. Green Energy Technology. Springer, 1st edition, 2018, DOI: 10.1007/978-981-10-1947-0_19.

[139] I. J. Breukels. Kite launch using an aerostat. Master's thesis, Delft University of Technology, The Netherlands, Aug. 2007.

[140] F. Trevisi. Configuration optimisation of kite-based wind turbines. Master's thesis, Technical University of Denmark, Denmark, Oct. 2019.

[141] F. Bauer, R. M. Kennel, C. M. Hackl, F. Campagnolo, M. Patt, and R. Schmehl. Drag power kite with very high lift coefficient. *Renewable Energy*, 118:290–305, Apr. 2018, DOI: 10.1016/j.renene.2017.10.073.

[142] F. Bauer, R. M. Kennel, C. M. Hackl, F. Campagnolo, M. Patt, and R. Schmehl. Drag-mode airborne wind energy vs. wind turbines: An analysis of power production, variability and geography. *Energy*, 193, Dec. 2019, DOI: 10.1016/j.energy.2019.116765.

[143] F. Gohl and R. H. Luchsinger. Simulation based wing design for kite power. In U. Ahrens, M. Diehl, and R. Schmehl, editors, *Airborne Wind Energy*, chapter 18, pp. 325–338. Green Energy Technology. Springer, 1st edition, 2014, DOI: 10.1007/978-3-642-39965-7_18.

[144] M. Bomberg and T. Kisilewicz. Durability of materials and components. In M. Bomberg, T. Kisilewicz, and C. Mattock, editors, *Methods of Building Physics*, chapter 4, pp. 173–217. CracowU of technology, 1st edition, 2015. ISBN 978-83-7242-886-8.

[145] E. C. Malz, M. Zanon, and S. Gros. A quantification of the performance loss of power averaging in airborne wind energy farms. In *2018 European Control Conference (ECC)*, pp. 58–63, 2018, DOI: 10.23919/ECC.2018.8550357.

[146] C. Vermillion, M. Cobb, L. Fagiano, R. Leuthold, M. Diehl, R. S. Smith, T. A. Wood, S. Rapp, R. Schmehl, D. Olinger, and M. Demetriou. Electricity in the air: Insights from two decades of advanced control research and experimental flight testing of airborne wind energy systems. *Annual Reviews in Control*, 52:330–357, Mar. 2021, DOI: 10.1016/j.arcontrol.2021.03.002.

[147] V. Salma, F. Friedl, and R. Schmehl. Improving reliability and safety of airborne wind energy systems. *Wind Energy*, 23(5), Oct. 2019, DOI: 10.1002/we.2433.

[148] K. van Hussen, E. Dietrich, J. Smeltink, K. Berentsen, M. van der Sleen, R. Haffner, and L. Fagiano. *Study on Challenges in the commercialisation of airborne wind energy systems*. European Commission, Belgium, 1st edition, Sep. 2018. URL: `https://rb.gy/cpbw1i`.

[149] X. Paulig, M. Bungart, and B. Specht. Conceptual design of textile kites considering overall system performance. In U. Ahrens, M. Diehl, and R. Schmehl, editors, *Airborne Wind Energy*, chapter 32, pp. 547–562. Green Energy Technology. Springer, 1st edition, 2014, DOI: 10.1007/978-3-642-39965-7_32.

[150] U. Fechner and R. Schmehl. Design of a distributed kite power control system. In *2012 IEEE International Conference on Control Applications (CCA)*, Oct. 2012.

[151] L. Fagiano and S. Schnez. On the take-off of airborne wind energy systems based on rigid wings. *Renewable Energy*, 107:473–488, Feb. 2017, DOI: 10.1016/j.renene.2017.02.023.

[152] C. E. Harris, J. H. S. Jr., and M. J. Shuart. Design and manufacturing of aerospace composite structures, state-of-the-art assessment. *Journal of Aircraft*, 39(4), Aug. 2002, DOI: 10.2514/2.2992.

[153] Fortify. 4 reasons why composites are replacing traditional materials. URL: `https://rb.gy/ggkrim`. Visited: 26-03-2022.

[154] G. D. Goh, S. Agarwala, G. L. Goh, V. Dikshit, S. L. Sing, and W. Y. Yeong. Additive manufacturing in unmanned aerial vehicles (uavs): Challenges and potential. *Aerospace Science and Technology*, 63:140–151, Apr. 2017, DOI: 10.1016/j.ast.2016.12.019.

[155] J. Heilmann and C. Houle. Economics of pumping kite generators. In U. Ahrens, M. Diehl, and R. Schmehl, editors, *Airborne Wind Energy*, chapter 15, pp. 271–284. Green Energy Technology. Springer, 1st edition, 2014, DOI: 10.1007/978-3-642-39965-7_15.

[156] J. Coleman, H. Ahmad, E. Pican, and D. Toal. Modelling of a synchronous offshore pumping mode airborne wind energy farm. *Energy*, 71:569–578, Apr. 2014, DOI: 10.1016/j.energy.2014.04.110.

[157] M. E. Salari, G. Dooly, J. Coleman, and D. Toal. Direct interconnection of offshore airborne wind energy systems. In *OCEANS 2015 - MTS/IEEE Washington*, pp. 1–8, Oct. 2015, DOI: 10.23919/OCEANS.2015.7404504.

[158] D. Pavković, M. Hoić, J. Deur, and J. Petrić. Energy storage systems sizing study for a high-altitude wind energy application. *Energy*, 76, May 2014, DOI: 10.1016/j.energy.2014.04.001.

[159] M. Aull, A. Stough, and K. Cohen. Design optimization and sizing for fly-gen airborne wind energy systems. *Automation*, 10:1–16, June 2020, DOI: 10.3390/automation1010001.

[160] H. Schmidt, G. de Vries, R. J. Renes, and R. Schmehl. Public responses to airborne wind energy: A literature review.

[161] L. D. Knopper, C. A. Ollson, L. C. McCallum, M. L. W. Aslund, R. G. Berger, K. Souweine, and M. McDaniel. Wind turbines and human health. *Renewable Energy*, June 2014, DOI: 10.3389/fpubh.2014.00063.

[162] M. D. L. Oliveira. *Airborne Wind Energy with Tethered Wings: Modeling, Analysis and Control*. PhD thesis, Federal University of Santa Catarina, Florianópolis, Santa Catarina, Brazil, July 2016. URL: `https://repositorio.ufsc.br/xmlui/handle/123456789/173661`.

[163] L. W. Bruinzeel, A. Brenninkmeijer, E. Klop, and J. Bosch. Ecological impact of airborne wind energy technology: Current state of knowledge and future research agenda. In R. Schmehl, editor, *Airborne Wind Energy: Advances in Technological Development and Research*, chapter 28, pp. 679–701. Green Energy Technology. Springer, 1st edition, 2018, DOI: 10.1007/978-981-10-1947-0_28.

[164] A. Håland. Testing of kitemill's airborne wind energy system at lista, norway. assessing the impacts on birds. a pilot study. Technical report, Kitemill AS, Paradis, Norway, Dec. 2018. URL: `https://rb.gy/roe0qo`.

[165] R. E. David and K. C. Kawahara. Bird and bat conservation plan makani energy kite project, south kohala district, island of hawai. Technical report, Makani Power, Nov. 2018. URL: `https://rb.gy/hxjxwv`.

[166] J. Weber, M. Marquis, A. Cooperman, C. Draxl, R. Hammond, J. Jonkman, A. Lemke, A. Lopez, R. Mudafort, M. Optis, O. Roberts, and M. Shields. Airborne wind energy. Technical report, National Renewable Energy Laboratory, Colorado, United States, Aug. 2021. URL: `https://rb.gy/xfiohi`.

[167] *Agile Airborne Wind Energy System Design with Bird Impact Detection*, Texas, United States, Jan. 2017. American Institute of Aeronautics and Astronautics, DOI: 10.2514/6.2017-1170.

[168] K. Petrick, U. Zillmann, and R. Schmehl. Policies for airborne wind energy - preparing the grounds for awe-specific incentive schemes (scoping study). In *Airborne Wind Europe*, Brussels, Belgium, Jan. 2018. URL: `https://rb.gy/rwryyu`.

[169] V. Salma, M. Kruijff, R. Ruiterkamp, and M. M. V. Paassen. Current and expected airspace regulations for airborne wind energy systems. In R. Schmehl, editor, *Airborne Wind Energy: Advances in Technological Development and Research*, chapter 29, pp. 703–725. Green Energy Technology. Springer, 1st edition, 2018, DOI: 10.1007/978-981-10-1947-0_29.

[170] G. Abbate and E. Saraceno. What else is emerging from the horizon? In A. Vasel and D. Ting, editors, *Advances in Sustainable Energy*, volume 70, chapter 10, pp. 177–213. Lecture Notes in Energy. Springer, 2019, DOI: 10.1007/978-3-030-05636-0_10.

[171] B. Zlaugotne, L. Zihare, L. Balode, A. Kaknbalkite, A. Khabdullin, and D. Blumberga. Multi-criteria decision analysis methods comparison. *Environmental and Climate Technologies*, 24(1):454–471, 2020, DOI: 10.2478/rtuect-2020-0028.

[172] J. S. Dodgson, M. Spackman, A. D. Pearman, and L. D. Phillips. *Multi-criteria analysis: a manual*. Department for Communities and Local Government, London, UK, Jan. 2009.

[173] A. Mardani, A. Jusoh, K. M. Nor, Z. Khalifah, N. Zakwan, and A. Valipour. Multiple criteria decision-making techniques and their applications – a review of the literature from 2000 to 2014. *Environmental and Climate Technologies*, 28(1):516–571, July 2015, DOI: 10.1080/1331677X.2015.1075139.

[174] A. Kumar, B. Sah, A. R. Singh, Y. Deng, X. He, P. Kumar, and R. C. Bansal. A review of multi criteria decision making (mcdm) towards sustainable renewable energy development. *Renewable and Sustainable Energy Reviews*, 69:596–609, Mar. 2017, DOI: 10.1016/j.rser.2016.11.191.

[175] U. Asan, A. Soyer, and S. SerdarAsan. *A Fuzzy Analytic Network Process Approach*, chapter 8, pp. 159–183. Atlantis Press, Jan. 2012, DOI: 10.2991/978-94-91216-77-0_8.

[176] S. Kheybari, F. M. Rezaie, and H. Farazmand. Analytic network process: An overview of applications. *Applied Mathematics and Computation*, 367, Sep. 2019, DOI: 10.1016/j.amc.2019.124780.

[177] T. L. Saaty and L. G. Vargas. *The Analytic Network Process*, pp. 1–26. Springer US, Boston, MA, 2006. ISBN 978-0-387-33987-0, DOI: 10.1007/0-387-33987-6_1.

[178] *Tutorial on Complex Decision Models (ANP)*. SuperDecisions, 2021. URL: `https://rb.gy/etn1bj`.

[179] B. Adams. Superdecisions limit matrix calculations. URL: `https://rb.gy/74sfds`.

[180] N. Kadoić. Characteristics of the analytic network process, a multi-criteria decision-making method. *Croatian Operational Research Review*, 9(2):235–244, Dec. 2018, DOI: 10.17535/crorr.2018.0018.

[181] R. Lowen. *Fuzzy Set Theory*, chapter 4, pp. 133–141. Springer, 1996, DOI: 10.1007/978-94-015-8741-9.

[182] L. Mikhailov. Deriving priorities from fuzzy pairwise comparison judgements. *Fuzzy Sets and Systems*, 134(3):365–385, Mar. 2003, DOI: 10.1016/S0165-0114(02)00383-4.

[183] X. Zhou. Fuzzy analytical network process implementation with matlab. In *MATLAB - A Fundamental Tool for Scientific Computing and Engineering Applications*, chapter 6. IntechOpen, Rijeka, 2012, DOI: 10.5772/46466.

[184] P. T. Boggs and J. W. Tolle. Sequential quadratic programming. *Acta Numerica*, 4:1–51, Jan. 1995, DOI: 10.1017/S0962492900002518.

[185] S. Kubler, W. Derigent, A. Voisin, J. Robert, and Y. Le Traon. Knowledge-based consistency index for fuzzy pairwise comparison matrices. In *2017 IEEE International Conference on Fuzzy Systems (FUZZ-IEEE)*, 2017, DOI: 10.1109/FUZZ-IEEE.2017.8015380.

[186] A. F. C. Pereira and J. M. M. de Sousa. Assisted site-dependent selection of the most suitable airborne wind energy system via fuzzy analytic network process: Datasets and supplementary materials. URL: `https://data.mendeley.com/datasets/d9xh5552vn/1`.

[187] M. Optis, A. Monahan, and F. C. Bosveld. Moving beyond monin–obukhov similarity theory in modelling wind-speed profiles in the lower atmospheric boundary layer under stable stratification. *Boundary-Layer Meteorology volume*, 153(3):497–514, Dec. 2014, DOI: 10.1007/s10546-014-9953-z.

[188] B. Cushman-Roisin. *Environmental Fluid Mechanics*, chapter 12, pp. 165–185. John Wiley & Sons, Inc., Thayer School of Engineering, Hanover, New Hampshire, USA, 2022. URL: `https://rb.gy/fbmagt`.

[189] C. L. Archer. An introduction to meteorology for airborne wind energy. In U. Ahrens, M. Diehl, and R. Schmehl, editors, *Airborne Wind Energy*, chapter 5, pp. 81–94. Green Energy Technology. Springer, 1st edition, 2014, DOI: 10.1007/978-3-642-39965-7_5.

[190] L. M. Miller, F. Gans, and A. Kleidon. Jet stream wind power as a renewable energy resource: little power, big impacts. *Earth System Dynamics*, 2(2):201–212, Nov. 2011, DOI: 10.5194/esd-2-201-2011.

[191] *Manual VFR*. Aeronautical Information Service, Portugal, 12 2021. Available in `https://rb.gy/zedsia`.

[192] L. Prandtl. The mechanics of viscous fluids. In W. F. Duran, editor, *Aerodynamic theory; a general review of progress, under a grant of the Guggenheim fund for the promotion of aeronautics.*, volume 3. Springer, Berlin, Germany, 1935. ISBN 9783662397657.

[193] A. G. Davenport. The treatment of wind loading on tall buildings. In A. Coull and B. S. Smith, editors, *Tall Buildings*, pp. 3–45. Pergamon, 1967, DOI: 10.1016/B978-0-08-011692-1.50006-7.

[194] J. Y. R. Liew, T. Balendra, and W. F. Chen. Multistory frame structures. In W. F. Chen, editor, *Handbook for Structural Engineering*, chapter 22. CRC Press, Boca Raton, 2nd edition, Feb. 2005, DOI: 10.1201/9781420039931.

[195] C. P. Albornoz, M. E. Soberanis, V. R. Rivera, and M. Rivero. Review of atmospheric stability estimations for wind power applications. *Renewable and Sustainable Energy Reviews*, 163, Apr. 2022, DOI: 10.1016/j.rser.2022.112505.

[196] A. Monin and A. Obukhov. Basic laws of turbulent mixing in the surface layer of the atmosphere. *Trudy Geofiz. Inst. Akad. Nauk SSSR*, 151:163–187, 1954. (in Russian).

[197] R. H. Thuillier and U. O. Lappe. Wind and temperature profile characteristics from observations on a 1400 ft tower. *Journal of Applied Meteorology and Climatology*, 134(3):299–306, June 1964, DOI: 10.1175/1520-0450(1964)003¡0299:WATPCF¿2.0.CO;2.

[198] M. Holtslag, W. Bierbooms, and G. van Bussel. Estimating atmospheric stability from observations and correcting wind shear models accordingly. *Journal of Physics Conference Series*, 555(1), Dec. 2014, DOI: 10.1088/1742-6596/555/1/012052.

[199] M. Schelbergen, P. Kalverla, R. Schmehl, and S. Watson. Clustering wind profile shapes to estimate airborne wind energy production. *Wind Energy Science*, 5(3):1097–1120, Aug. 2020, DOI: 10.5194/wes-5-1097-2020.

[200] M. Sommerfeld, C. Crawford, A. Monahan, and I. Bastigkeit. Lidar-based characterization of mid-altitude wind conditions for airborne wind energy systems. *Wind Energy*, 22:1101–1120, Mar. 2019, DOI: 10.1002/we.2343.

[201] K. Essa, M. Embaby, A. Kozae, F. Mubarak, and I. Kamel. Estimation of seasonal atmospheric stability and mixing height by using different schemes. In *Proceedings of the Eigth Radiation Physics and Protection Conference (RPC-2006)*, Egypt, 2007. URL: `https://rb.gy/9njz7m`.

[202] A. Hassoon, S. Mohammed, and H. Al-Saleem. Atmospheric stability and its effect on the polluted columns of concentrations in north west of baghdad city. *Iraqi Journal of Science*, 55(2):572–581, Jan. 2014, DOI: 10.13140/RG.2.2.10928.00006.

[203] J. M. M. Sousa. Using meso-scale modelling for the prediction of wind resources in portugal. In N. H. Afgan and M. G. Carvalho, editors, *New and Renewable Energy Technologies for Sustainable Development*, volume 4 of *5*, chapter Wind Energy Resources, pp. 201–213. Swets & Zeitlinger, 3rd edition, Jan. 2004, DOI: 10.1201/9781003078883-14.

[204] D. Heinmann. Estimation of regional surface layer wind field characteristics using a three-layer meso-scale model. *Contributions to Atmospheric Physics*, 59:518–537, Nov. 1986.

[205] EnergyData. Global wind atlas. URL: https://rb.gy/wspmui. Visited: 11-07-2022.

[206] EnergyData. Global wind atlas datasets. URL: https://rb.gy/djqwyv. Visited: 11-07-2022.

[207] H. E. C. Delgado. *Novas Tecnologias Biomiméticas para a Aerodinâmica de Veículos Aéreos a Baixo Número de Reynolds*. PhD thesis, Instituto Superior Técnico, Lisboa, Portugal, 2018. URL: https://rb.gy/lgu1yp.

[208] F. J. M. Roque. Desenvolvimento de uma plataforma aberta e escalável para aquisição de dados no túnel aerodinâmico de baixa velocidade. Master's thesis, Instituto Superior Técnico, Lisboa, Portugal, 2012. URL: https://rb.gy/ljgjw6.

[209] H. W. Coleman and W. G. Steele. *Experimentation, Validation, and Uncertainty Analysis for Engineers*. Wiley, United Kingdom, 4th edition, 2018. ISBN 9781119417705.

[210] J. B. Barlow, J. William H. Rae, and A. Pope. *Low-Speed Wind Tunnel Testing*. Wiley, USA, 3rd edition, 1999. ISBN 9780471557746.

[211] S. A. Yon and J. Katz. Study of the unsteady flow features on a stalled wing. *AIAA Journal*, 36(3): 305–312, Mar. 1998, DOI: 10.2514/3.13821.

[212] G. Sánchez-Arriaga, A. Pastor-Rodríguez, M. Sanjurjo-Rivo, and R. Schmehl. A lagrangian flight simulator for airborne wind energy systems. *Applied Mathematical Modelling*, 69:665–684, May 2019, DOI: 10.1016/j.apm.2018.12.016.

[213] J. W. Kolar, T. Friedli, F. Krismer, A. Looser, M. Schweizer, P. Steimer, and J. Bevirt. Conceptualization and multi-objective optimization of the electric system of an airborne wind turbine. In *2011 IEEE International Symposium on Industrial Electronics*, pp. 32–55, 2011, DOI: 10.1109/ISIE.2011.5984131.

[214] A. H. Niasar and M. Moazzemi. Design and implementation of direct power control system for brushless dc generator in standalone dc applications. *Electric Power Components and Systems*, 45(7):752–762, 2017, DOI: 10.1080/15325008.2017.1309722.

[215] D. Collins. Are brushed motors suitable for industrial applications? URL: https://rb.gy/bdryag. Visited: 21-10-2022.

[216] Electrical4U. Parallel operation of dc generators? URL: https://rb.gy/nqpysf. Visited: 10-09-2022.

[217] M. Stiebler. *Wind Energy Systems for Electric Power Generation*. Springer, Berlin, Germany, 1st edition, 2008. ISBN 978-3-540-68762-7.

[218] SeeSensor. Usb tester 3-bit high precision current voltmeter. URL: https://rb.gy/5eigaj. Visited: 25-10-2022.

[219] ChinaTech. Sq11 mini dv camera setup, review, instructions and sample footage! URL: https://rb.gy/dwhkky. Visited: 25-10-2022.

[220] Windfinder. Relatórios de vento de quinta-feira, 27 de outubro de 2022. URL: https://rb.gy/dq6zcl. Visited: 27-10-2022.

[221] P. Williams, S. Sieberling, and R. Ruiterkamp. Flight test verification of a rigid wing airborne wind energy system. In *2019 American Control Conference (ACC)*, pp. 2183–2190, 2019, DOI: 10.23919/ACC.2019.8814338.

Appendix A: FANP Method Matrices

A.1 Example Comparison Matrices

A few examples of comparison matrices relative to step 2 and 3 of the Fuzzy Analytic Network Process are presented here. Let it be noted that only the most probable value of the fuzzy set (m^z) is presented.

Table A.1: Comparison of TDF with respect to the GOAL - Rural scenario.

	AP	**MA**	**DU**	**SU**	**w**
AP	1	2	4	8	0.4567
MA	1/2	1	4	8	0.3753
DU	1/4	1/4	1	3	0.1160
SU	1/8	1/8	1/3	1	0.0520
CI	0.2170				

Table A.2: Comparison of AP dependencies.

	MA	**DU**	**w**
MA	1	5	0.8333
DU	1/5	1	0.1667
CI	1		

Table A.3: Comparison of alternatives with respect to AP.

	A1	**A2**	**A3**	**A4**	**A5**	**A6**	**A7**	**A8**	**A9**	**w**
A1	1	1.5	3	6	6	7	4	2	1	0.1987
A2	2/3	1	3	5.5	5.5	6.5	4	1	2/3	0.1876
A3	1/3	1/3	1	4	4	4.5	2.5	1/3	1/3	0.0913
A4	1/6	1/5.5	1/4	1	1.5	2	1/2.5	1/5.5	1/6	0.0299
A5	1/6	1/5.5	1/4	2/3	1	1.5	1/2.5	1/5.5	1/6	0.0291
A6	1/7	1/6.5	1/4.5	1/2	2/3	1	1/3	1/6.5	1/7	0.0255
A7	1/4	1/4	1/2.5	2.5	2.5	3	1	1/4	1/4	0.0547
A8	1/2	1	3	5.5	5.5	6.5	4	1	2/3	0.1864
A9	1	1.5	3	6	6	7	4	1.5	1	0.1968
CI	0.0544									

Table A.4: Evaluation of A1 with respect to TDF.

	AP	**MA**	**DU**	**SU**	**w**
AP	1	5	3	7	0.5720
MA	1/5	1	1/3	2	0.1066
DU	1/3	3	1	4	0.2469
SU	1/7	1/2	1/4	1	0.0745
CI	0.3166				

Table A.5: Cluster comparison with respect to the GOAL cluster - Rural scenario.

	TDF	**OF**	**M**	**L**	**SAF**	**w**
TDF	1	2	5	7	4	0.4604
OF	1/2	1	3	4	2	0.2492
M	1/5	1/3	1	2	1/2	0.0931
L	1/7	1/4	1/2	1	1/3	0.0603
SAF	1/4	1/2	2	3	1	0.1370
CI	0.3606					

A.2 Unweighted Supermatrix

The resulting unweighted supermatrix, subdivided per clusters, for both on-shore rural and off-shore exploration sites portrayed in figure A.1 is presented here.

Since these matrices only differ in the first column, relative to the GOAL dependencies, that is given in the bottom of the figure, for each type of exploration site.

	Goal	AP	MA	DU	SU	CPP	CTR	TLF	M	L	VI	NI	EI	SF	A1	A2	A3	A4	A5	A6	A7	A8	A9
Goal	0	0	0	1	1	0	0	0	0	1	1	1	1	1	0	0	0	0	0	0	0	0	0
AP	a	0	1	0	0	1	0.7500	0.5000	0.4449	0	0	0	0	0	0.5721	0.5752	0.4444	0.1591	0.1507	0.1301	0.3592	0.5976	0.6042
MA	b	0.8333	0	0	1	0	0.2500	0.5000	0.4551	1	1	0	0.8333	1	0.1066	0.0852	0.2977	0.6557	0.6553	0.6976	0.4097	0.0701	0.0671
DU	c	0.1667	0	0	0	0	0	0	0.1	0	0	0	0	0	0.2469	0.2662	0.2077	0.0741	0.0862	0.0775	0.1599	0.2401	0.2364
SU	d	0	0	0	0	0	0	0	0	0	0	0	0.1667	0	0.0745	0.0734	0.0502	0.1111	0.1077	0.0947	0.0712	0.0922	0.0923
CPP	e	0	0	0	0	0	0	0	0	0	0	0	0	0	0.0916	0.0840	0.1128	0.0628	0.0670	0.1128	0.1012	0.5486	0.5486
CTR	f	1	0	0	1	1	0	1	0	0	0	0	0	1	0.5168	0.3801	0.6265	0.4044	0.3757	0.6265	0.5467	0.3904	0.3904
TLF	g	0	0	0	0	0	0	0	0	1	0	0	0	0	0.3916	0.5359	0.2607	0.5328	0.5573	0.2607	0.3522	0.0610	0.0610
M	h	0	0	0	0	0	0	0	0	0	0	0	0	0	1	1	1	1	1	1	1	1	1
L	i	0	0	0	0	0	0	0	0	0	0	0	0	0	1	1	1	1	1	1	1	1	1
VI	j	0	0	0	0	0	0	0	0	0	0	0	0	0	0.5761	0.5761	0.3914	0.0593	0.0542	0.0593	0.0613	0.6311	0.6311
NI	k	0	0	0	0	0	0	0	0	0	0	0	0	0	0.1075	0.1075	0.4397	0.4532	0.4089	0.4532	0.4666	0.0701	0.0701
EI	l	0	0	0	0	0	0	0	0	0	0	0	0	0	0.1582	0.1582	0.0928	0.2932	0.3055	0.2932	0.3330	0.1548	0.1548
SF	m	0	0	0	0	0	0	0	0	0	0	0	0	0	0.1582	0.1582	0.0761	0.1942	0.2315	0.1942	0.1391	0.1439	0.1439
A1	0	0.1987	0.0537	0.1548	0.0646	0.0920	0.1816	0.2681	0.0794	0.2191	0.1440	0.0976	0.0411	0.0582	0	0	0	0	0	0	0	0	0
A2	0	0.1875	0.0392	0.1446	0.0647	0.0920	0.1817	0.3067	0.0718	0.2517	0.1440	0.0976	0.0411	0.0582	0	0	0	0	0	0	0	0	0
A3	0	0.0913	0.0801	0.1628	0.0309	0.0828	0.0259	0.0347	0.1284	0.0348	0.2095	0.1239	0.0374	0.0457	0	0	0	0	0	0	0	0	0
A4	0	0.0299	0.2073	0.0262	0.2353	0.0324	0.0414	0.0986	0.2155	0.1115	0.0372	0.1711	0.2171	0.2129	0	0	0	0	0	0	0	0	0
A5	0	0.0291	0.2073	0.0339	0.2554	0.0324	0.0289	0.0986	0.2155	0.1115	0.0372	0.1711	0.1957	0.2610	0	0	0	0	0	0	0	0	0
A6	0	0.0255	0.2232	0.0208	0.2120	0.0328	0.0414	0.0589	0.1833	0.0436	0.0372	0.1227	0.2171	0.2090	0	0	0	0	0	0	0	0	0
A7	0	0.0547	0.1373	0.0882	0.0364	0.0525	0.0326	0.0612	0.0499	0.1115	0.0372	0.1711	0.1302	0.0761	0	0	0	0	0	0	0	0	0
A8	0	0.1864	0.0259	0.1843	0.0504	0.2915	0.2333	0.0366	0.0298	0.0582	0.1768	0.0224	0.0601	0.0395	0	0	0	0	0	0	0	0	0
A9	0	0.1968	0.0259	0.1843	0.0504	0.2915	0.2333	0.0366	0.0264	0.0582	0.1768	0.0224	0.0601	0.0395	0	0	0	0	0	0	0	0	0

Site	a	b	c	d	e	f	g	h	i	j	k	l	m
Rural	0.4567	0.3753	0.1160	0.0520	0.0840	0.6412	0.2748	1	1	0.0665	0.3411	0.1424	0.4500
Off-shore	0.4192	0.3496	0.1589	0.0723	0.0774	0.5696	0.3530	1	1	0.1300	0.0864	0.4708	0.3128

Figure A.1: Unweighted supermatrix for the FANP method, for both rural and off-shore exploration sites.

A.3 Normalized Weighted Supermatrix

Next, the resulting normalized weighted supermatrix, subdivided per clusters, for both on-shore rural (figure A.2) and off-shore (figure A.3) exploration sites, is presented.

	Goal	AP	MA	DU	SU	CPP	CTR	TLF	M	L	VI	NI	EI	SF	A1	A2	A3	A4	A5	A6	A7	A8	A9
Goal	0	0	0	0.5026	0.0777	0	0	0	0	0.0985	0.3651	0.4313	0.3651	0.3409	0	0	0	0	0	0	0	0	0
AP	0.2103	0	0.8848	0	0	0.6985	0.6636	0.3492	0.3707	0	0	0	0	0	0.2329	0.2342	0.1810	0.0648	0.0614	0.0530	0.1463	0.2433	0.2460
MA	0.1728	0.5336	0	0	0.5906	0	0.2212	0.3492	0.3793	0.1248	0.1536	0	0.1280	0.1434	0.0434	0.0347	0.1212	0.2670	0.2668	0.2840	0.1668	0.0286	0.0273
DU	0.0534	0.1067	0	0	0	0	0	0	0.0833	0	0	0	0	0	0.1005	0.1084	0.0846	0.0302	0.0351	0.0316	0.0651	0.0977	0.0962
SU	0.0239	0	0	0	0	0	0	0	0	0	0	0	0.0256	0	0.0303	0.0299	0.0204	0.0452	0.0439	0.0386	0.0290	0.0376	0.0376
CPP	0.0209	0	0	0	0	0	0	0	0	0	0	0	0	0	0.0275	0.0252	0.0338	0.0188	0.0201	0.0338	0.0303	0.1644	0.1644
CTR	0.1598	0.2764	0	0	0.2549	0.2106	0	0.2106	0	0	0	0	0	0.0661	0.1548	0.1139	0.1877	0.1212	0.1126	0.1877	0.1638	0.1170	0.1170
TLF	0.0685	0	0	0	0	0	0	0	0	0.2317	0	0	0	0	0.1173	0.1606	0.0781	0.1596	0.1670	0.0781	0.1055	0.0183	0.0183
M	0.0931	0	0	0	0	0	0	0	0	0	0	0	0	0	0.1649	0.1649	0.1649	0.1649	0.1649	0.1649	0.1649	0.1649	0.1649
L	0.0603	0	0	0	0	0	0	0	0	0	0	0	0	0	0.0471	0.0471	0.0471	0.0471	0.0471	0.0471	0.0471	0.0471	0.0471
VI	0.0091	0	0	0	0	0	0	0	0	0	0	0	0	0	0.0467	0.0467	0.0318	0.0048	0.0044	0.0048	0.0050	0.0512	0.0512
NI	0.0467	0	0	0	0	0	0	0	0	0	0	0	0	0	0.0087	0.0087	0.0357	0.0368	0.0332	0.0368	0.0379	0.0057	0.0057
EI	0.0195	0	0	0	0	0	0	0	0	0	0	0	0	0	0.0128	0.0128	0.0075	0.0238	0.0248	0.0238	0.0270	0.0126	0.0126
SF	0.0617	0	0	0	0	0	0	0	0	0	0	0	0	0	0.0128	0.0128	0.0062	0.0158	0.0188	0.0158	0.0113	0.0117	0.0117
A1	0	0.0166	0.0062	0.0770	0.0050	0.0084	0.0209	0.0244	0.0132	0.1194	0.0693	0.0555	0.0198	0.0262	0	0	0	0	0	0	0	0	0
A2	0	0.0156	0.0045	0.0719	0.0050	0.0084	0.0209	0.0279	0.0120	0.1372	0.0693	0.0555	0.0198	0.0262	0	0	0	0	0	0	0	0	0
A3	0	0.0076	0.0092	0.0810	0.0024	0.0075	0.0030	0.0032	0.0214	0.0189	0.1009	0.0705	0.0180	0.0205	0	0	0	0	0	0	0	0	0
A4	0	0.0025	0.0239	0.0131	0.0181	0.0029	0.0048	0.0090	0.0359	0.0608	0.0179	0.0973	0.1045	0.0957	0	0	0	0	0	0	0	0	0
A5	0	0.0024	0.0239	0.0169	0.0196	0.0029	0.0033	0.0090	0.0359	0.0608	0.0179	0.0973	0.0942	0.1173	0	0	0	0	0	0	0	0	0
A6	0	0.0021	0.0257	0.0104	0.0163	0.0030	0.0048	0.0054	0.0305	0.0238	0.0179	0.0698	0.1045	0.0940	0	0	0	0	0	0	0	0	0
A7	0	0.0046	0.0158	0.0438	0.0028	0.0048	0.0038	0.0056	0.0083	0.0608	0.0179	0.0973	0.0627	0.0342	0	0	0	0	0	0	0	0	0
A8	0	0.0155	0.0030	0.0917	0.0039	0.0265	0.0269	0.0033	0.0050	0.0317	0.0851	0.0127	0.0289	0.0177	0	0	0	0	0	0	0	0	0
A9	0	0.0164	0.0030	0.0917	0.0039	0.0265	0.0269	0.0033	0.0044	0.0317	0.0851	0.0127	0.0289	0.0178	0	0	0	0	0	0	0	0	0

Figure A.2: Normalized weighted supermatrix for the FANP method, for a rural exploration site.

	Goal	AP	MA	DU	SU	CPP	CTR	TLF	M	L	VI	NI	EI	SF	A1	A2	A3	A4	A5	A6	A7	A8	A9
Goal	0	0	0	0.7149	0.1857	0	0	0	0	0.3397	0.1065	0.1365	0.1065	0.0970	0	0	0	0	0	0	0	0	0
AP	0.1794	0	0.8869	0	0	0.6985	0.6636	0.3492	0.3707	0	0	0	0	0	0.2273	0.2285	0.1766	0.0632	0.0599	0.0517	0.1427	0.2374	0.2401
MA	0.1496	0.5939	0	0	0.5803	0	0.2212	0.3492	0.3793	0.0736	0.2196	0	0.1830	0.2000	0.0423	0.0338	0.1183	0.2605	0.2604	0.2772	0.1628	0.0279	0.0267
DU	0.0680	0.1188	0	0	0	0	0	0	0.0833	0	0	0	0	0	0.0981	0.1058	0.0825	0.0294	0.0343	0.0308	0.0635	0.0954	0.0939
SU	0.0309	0	0	0	0	0	0	0	0	0	0	0	0.0366	0	0.0296	0.0292	0.0199	0.0441	0.0428	0.0376	0.0283	0.0366	0.0367
CPP	0.0200	0	0	0	0	0	0	0	0	0	0	0	0	0	0.0280	0.0257	0.0345	0.0192	0.0205	0.0345	0.0309	0.1677	0.1677
CTR	0.1473	0.1964	0	0	0.1600	0.2106	0	0.2106	0	0	0	0	0	0.0890	0.1580	0.1162	0.1915	0.1236	0.1148	0.1915	0.1671	0.1193	0.1193
TLF	0.0913	0	0	0	0	0	0	0	0	0.2447	0	0	0	0	0.1197	0.1638	0.0797	0.1629	0.1704	0.0797	0.1076	0.0186	0.0186
M	0.1809	0	0	0	0	0	0	0	0	0	0	0	0	0	0.1857	0.1857	0.1857	0.1857	0.1857	0.1857	0.1857	0.1857	0.1857
L	0.0765	0	0	0	0	0	0	0	0	0	0	0	0	0	0.0665	0.0665	0.0665	0.0665	0.0665	0.0665	0.0665	0.0665	0.0665
VI	0.0073	0	0	0	0	0	0	0	0	0	0	0	0	0	0.0258	0.0258	0.0176	0.0027	0.0024	0.0027	0.0027	0.0283	0.0283
NI	0.0048	0	0	0	0	0	0	0	0	0	0	0	0	0	0.0048	0.0048	0.0197	0.0203	0.0183	0.0203	0.0209	0.0031	0.0031
EI	0.0264	0	0	0	0	0	0	0	0	0	0	0	0	0	0.0071	0.0071	0.0042	0.0131	0.0137	0.0131	0.0149	0.0069	0.0069
SF	0.0175	0	0	0	0	0	0	0	0	0	0	0	0	0	0.0071	0.0071	0.0034	0.0087	0.0104	0.0087	0.0062	0.0065	0.0065
A1	0	0.0181	0.0061	0.0441	0.0048	0.0084	0.0209	0.0244	0.0132	0.0749	0.0971	0.0843	0.0277	0.0357	0	0	0	0	0	0	0	0	0
A2	0	0.0170	0.0044	0.0412	0.0048	0.0084	0.0209	0.0279	0.0120	0.0861	0.0971	0.0843	0.0277	0.0357	0	0	0	0	0	0	0	0	0
A3	0	0.0083	0.0091	0.0464	0.0023	0.0075	0.0030	0.0032	0.0214	0.0119	0.1412	0.1070	0.0252	0.0280	0	0	0	0	0	0	0	0	0
A4	0	0.0027	0.0234	0.0075	0.0174	0.0029	0.0048	0.0090	0.0359	0.0381	0.0251	0.1477	0.1463	0.1307	0	0	0	0	0	0	0	0	0
A5	0	0.0026	0.0234	0.0097	0.0189	0.0029	0.0033	0.0090	0.0359	0.0381	0.0251	0.1477	0.1319	0.1602	0	0	0	0	0	0	0	0	0
A6	0	0.0023	0.0253	0.0059	0.0157	0.0030	0.0048	0.0054	0.0305	0.0149	0.0251	0.1060	0.1463	0.1283	0	0	0	0	0	0	0	0	0
A7	0	0.0050	0.0155	0.0251	0.0027	0.0048	0.0038	0.0056	0.0083	0.0381	0.0251	0.1477	0.0878	0.0467	0	0	0	0	0	0	0	0	0
A8	0	0.0169	0.0029	0.0525	0.0037	0.0265	0.0269	0.0033	0.0050	0.0199	0.1191	0.0193	0.0405	0.0242	0	0	0	0	0	0	0	0	0
A9	0	0.0179	0.0029	0.0525	0.0037	0.0265	0.0269	0.0033	0.0044	0.0199	0.1191	0.0193	0.0405	0.0242	0	0	0	0	0	0	0	0	0

Figure A.3: Normalized Weighted Supermatrix for the FANP method, for an off-shore exploration site.

Appendix B: $\mathrm{V_w}$ and $\mathrm{P_{w,\Delta h}}$ maps for different atmospheric stability conditions

One presents the maps of wind speed and power per width unit for three atmospheric stability conditions at $h = \{150, 350, 450\}\,\mathrm{m}$. As justified in chapter 5, the results for stable atmospheric conditions for the two last altitudes must be interpreted with caution.

At a height of $h = 150\,\mathrm{m}$, the wind speed maps show maximum wind speeds ranging from $9.5\,\mathrm{m/s}$, in unstable atmospheric conditions, to $16\,\mathrm{m/s}$. The corresponding $P_{w,\Delta h}$ are $12\,\mathrm{kW/m}$ and $36\,\mathrm{kW/m}$.

At the heights of $h = 350\,\mathrm{m}$ and $h = 450\,\mathrm{m}$, one must disregard the results for stable atmospheric conditions and assume, as the most optimistic projections, the values for neutral atmospheric stratification. Hence, one obtains a maximum wind speed, at $h = 350\,\mathrm{m}$, of $13\,\mathrm{m/s}$, matching a power passing through a strip of unit width of $26\,\mathrm{kW/m}$. At a height of $h = 450\,\mathrm{m}$ the maximum wind speeds are, in neutral stratification, about $h = 13.5\,\mathrm{m/s}$, matching a power of $30\,\mathrm{kW/m}$.

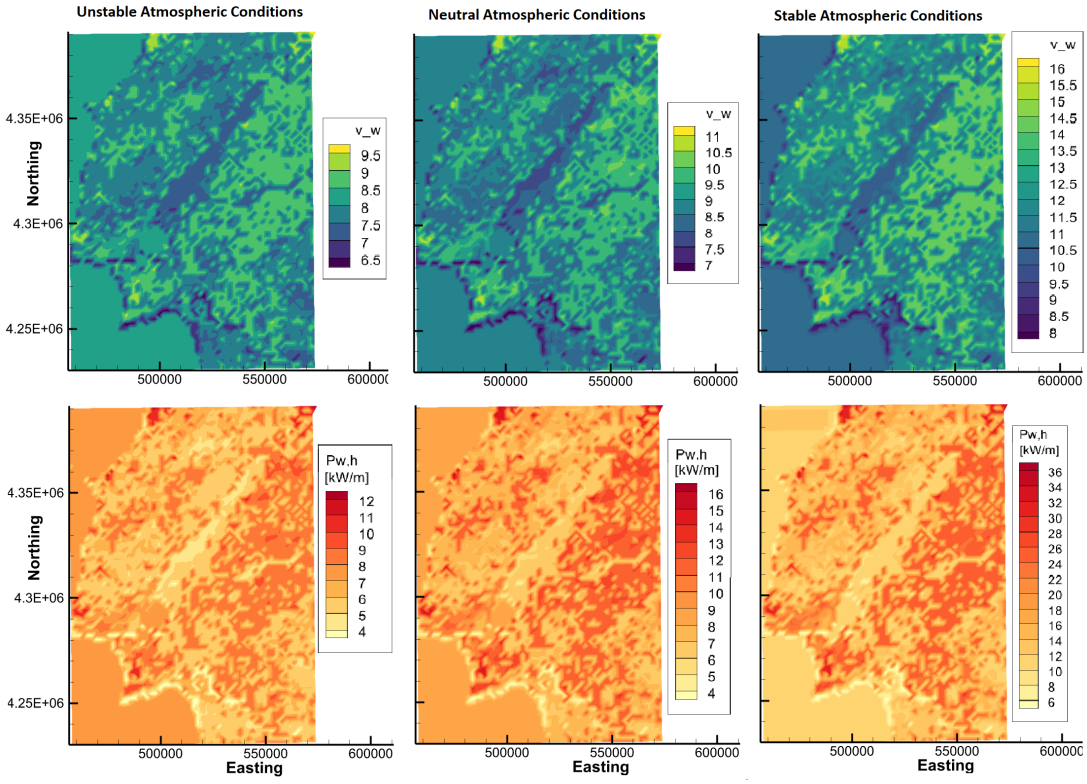

Figure B.1: Maps of v^* at $h = 150\,\mathrm{m}$ (top) and $P_{w,\Delta h}|_{h_0=140\,\mathrm{m}}^{h_1=160\,\mathrm{m}}$ (bottom) for unstable, neutral, and stable atmospheric conditions. The maps' axes are given in UTM coordinates.

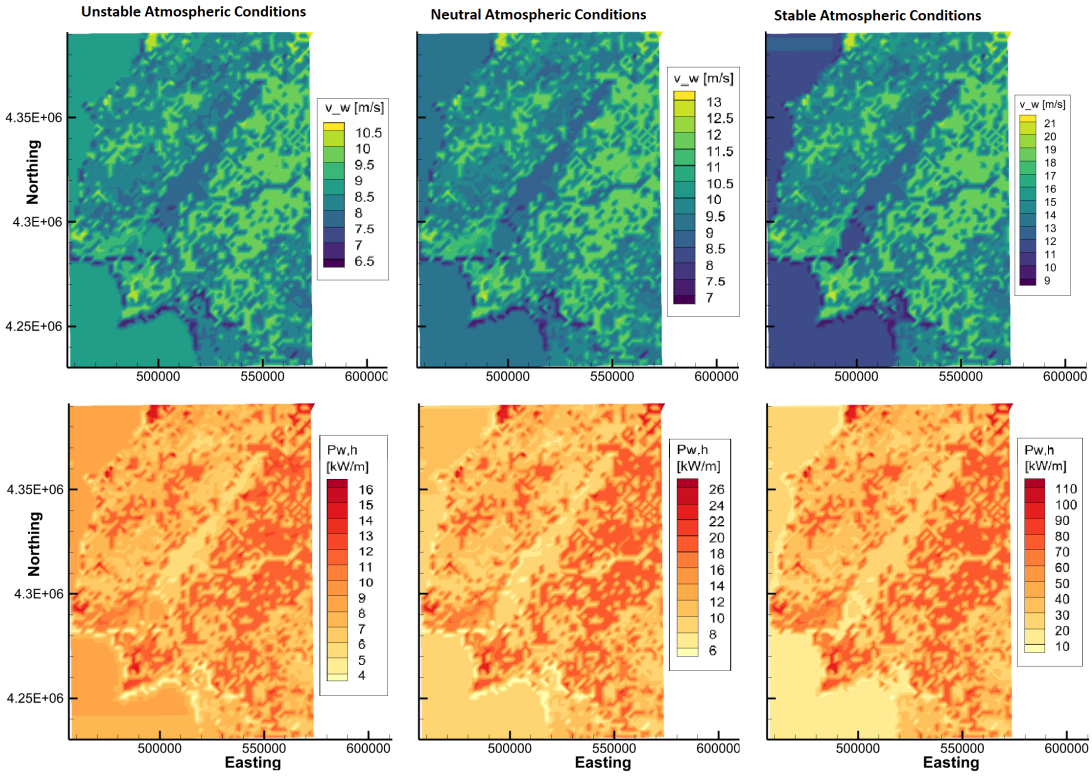

Figure B.2: Maps of v^* at $h = 350\,\mathrm{m}$ (top) and $P_{w,\Delta h}|_{h_0=340\,\mathrm{m}}^{h_1=360\,\mathrm{m}}$ (bottom) for unstable, neutral, and stable atmospheric conditions. The maps' axes are given in UTM coordinates.

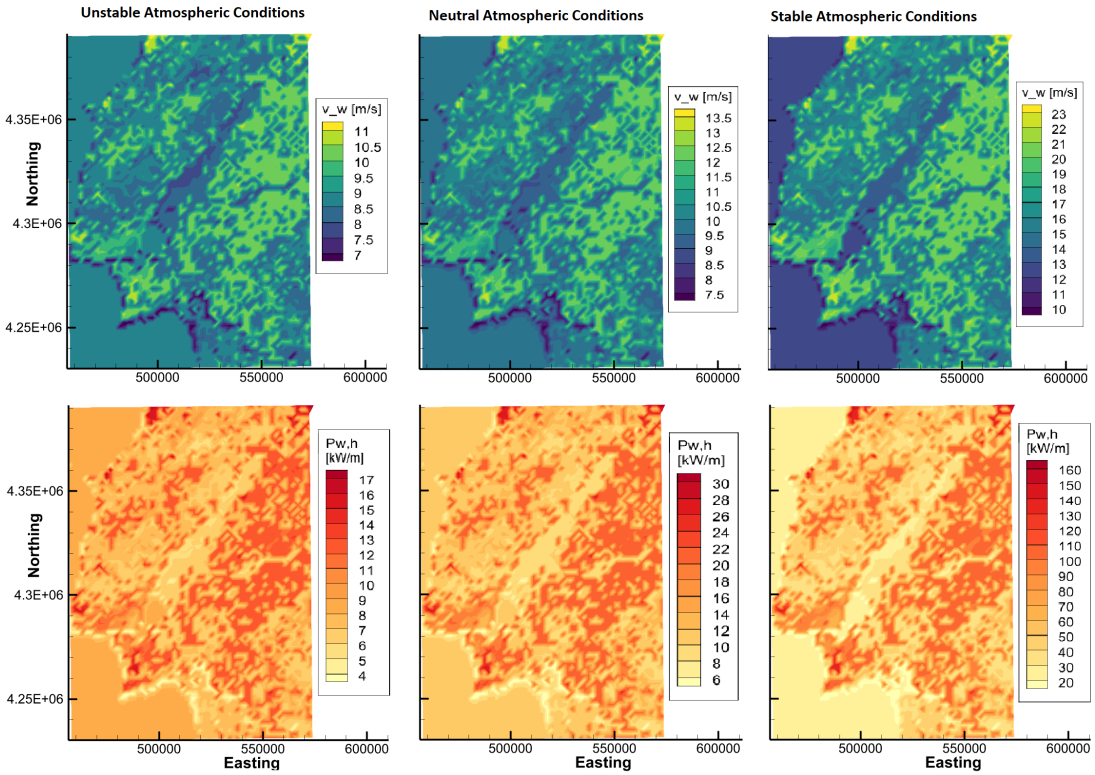

Figure B.3: Maps of v^* at $h = 450\,\mathrm{m}$ (top) and $P_{w,\Delta h}|_{h_0=440\,\mathrm{m}}^{h_1=460\,\mathrm{m}}$ (bottom) for unstable, neutral, and stable atmospheric conditions. The maps' axes are given in UTM coordinates.

Appendix C: Flight Test Measurements

Next, one presents video frames from the film recorded by the on-board camera during the flight test, which showcase the measurements presented in subsection 6.4.4 for the different flight conditions.

Figure C.1: Measured output voltage and current in an upwind climb flight condition (FC1).

Figure C.2: Measured output voltage and current in an downwind climb flight condition (FC2).

Figure C.3: Measured output voltage and current in a turning flight condition (FC3).

Figure C.4: Measured output voltage and current in a upwind horizontal leveled, with great turbulence, flight condition (FC4).

Figure C.5: Measured output voltage and current in a upwind horizontal leveled ”quasi-steady” flight condition (FC5).

Figure C.6: Measured output voltage and current in a downwind horizontal leveled ”quasi-steady” flight condition (FC6).

Figure C.7: Measured output voltage and current in an aerodynamic stall flight condition (FC7).

Figure C.8: Measured output voltage and current in a steep pitching flight condition (FC8).

Figure C.9: Measured output voltage and current in a gliding flight condition (FC9).